Sterile Neutrino Search with MINOS

Alena V. Devan

Kiev, Ukraine

Master of Science, College of William and Mary, 2010
Bachelor of Science, George Mason University, 2008

A Dissertation presented to the Graduate Faculty
of the College of William and Mary in Candidacy for the Degree of
Doctor of Philosophy

Department of Physics

The College of William and Mary
August 2015

APPROVAL PAGE

This Dissertation is submitted in partial fulfillment of
the requirements for the degree of

Doctor of Philosophy

Alena V. Devan

Approved by the Committee, July 2015

Committee Chair
Associate Professor Patricia Vahle, Physics
The College of William and Mary

Chancellor Professor David Armstrong, Physics
The College of William and Mary

Associate Professor Jeffrey Nelson, Physics
The College of William and Mary

Assistant Professor Andre Walker-Loud, Physics
The College of William and Mary

Assistant Professor Alexandre Sousa, Physics
University of Cincinatti

ABSTRACT

MINOS, Main Injector Neutrino Oscillation Search, is a long-baseline neutrino oscillation experiment in the NuMI muon neutrino beam at the Fermi National Accelerator Laboratory in Batavia, IL. It consists of two detectors, a near detector positioned 1 km from the source of the beam and a far detector 734 km away in Minnesota. MINOS is primarily designed to observe muon neutrino disappearance resulting from three flavor oscillations.

The Standard Model of Particle Physics predicts that neutrinos oscillate between three active flavors as they propagate through space. This means that a muon type neutrino has a certain probability to later interact as a different type of neutrino. In the standard picture, the neutrino oscillation probabilities depend only on three neutrino flavors and two mass splittings, Δm^2. An anomaly was observed by the LSND and MiniBooNE experiments that suggests the existence of a fourth, sterile neutrino flavor that does not interact through any of the known Standard Model interactions. Oscillations into a theoretical sterile flavor may be observed by a deficit in neutral current interactions in the MINOS detectors. A distortion in the charged current energy spectrum might also be visible if oscillations into the sterile flavor are driven by a large mass-squared difference, $\Delta m^2_s \sim 1\,\mathrm{eV}^2$. The results of the 2013 sterile neutrino search are presented here.

TABLE OF CONTENTS

Acknowledgments iv

Dedication v

List of Tables vi

List of Figures vii

CHAPTER

1 Neutrinos 2

1.1 Historical Perspective 2

1.2 Experimental Detection 4

1.3 Modern Evidence 8

1.4 Neutrinos in the Standard Model 10

1.5 Neutrino Oscillations 11

1.6 LSND Anomaly and Sterile Neutrinos 13

1.6.1 Four-flavor oscillations 15

2 The MINOS Experiment 19

2.1 NuMI beamline 20

2.2 The MINOS Detectors 23

2.2.1 Near Detector 24

2.2.2 Far Detector 27

2.3 Data Acquisition System 29

3 Calibration and Reconstruction . . . 33
3.1 Calibration . . . 33
3.2 Event Reconstruction . . . 39
3.3 Monte Carlo Event Simulation . . . 41
4 Event Identification . . . 44
4.1 Types of Events in MINOS . . . 44
4.1.1 ν_μ CC events . . . 45
4.1.2 ν_e CC events . . . 46
4.1.3 NC events . . . 47
4.2 NC Event Classification . . . 47
4.2.1 Near detector specific preselection . . . 48
4.2.2 Far detector specific preselection . . . 50
4.2.3 Neutral-current Event Selection . . . 51
4.3 Charged current Event Classification . . . 52
4.3.1 Near detector specific cuts . . . 54
4.3.2 Far detector specific cuts . . . 54
4.3.3 k-Nearest-Neighbor method of charged current identification . . . 55
5 Analysis . . . 59
5.1 MINOS 2011 Sterile Neutrino Search . . . 60
5.2 Far-over-Near Ratio . . . 60
5.2.1 Oscillation Probability . . . 62
5.2.2 Oscillated Monte Carlo . . . 63
5.2.3 Sterile Neutrino Oscillations at the Near Detector . . . 66
5.2.4 Varying Baseline . . . 67
5.3 χ^2 Minimization . . . 70

5.3.1 Fitting . . . 73
5.4 Surface Contours . . . 76
6 Systematic Uncertainties . . . 78
6.1 Uncertainties on NC selected events . . . 78
6.1.1 NC Normalization . . . 78
6.1.2 CC Background . . . 79
6.1.3 Relative Hadronic Energy . . . 81
6.1.4 Absolute Hadronic Energy . . . 81
6.1.5 Near Detector Cleaning . . . 82
6.1.6 Far Detector Cleaning . . . 83
6.2 Uncertainties on CC selected events . . . 84
6.2.1 CC Normalization . . . 84
6.2.2 NC Background . . . 85
6.2.3 Absolute Hadronic Energy . . . 85
6.2.4 Absolute Track Energy . . . 86
7 Results . . . 87
7.1 Three flavor comparison . . . 88
7.2 Four flavor comparison . . . 92
8 Conclusion . . . 97
8.1 Extending to a full range of Δm^2_{34} . . . 98
Bibliography . . . 101
Vita . . . 110

ACKNOWLEDGMENTS

I would like to thank my advisor, Patricia Vahle, for her guidance, knowledge and encouragement. A huge thanks to all the MINOS collaborators, this thesis would not be possible without their support and dedication to high energy physics. In particular, I would like to thank Alex Sousa, Justin Evans, Mark Mathis, Joao Coelho, Joe O'Connor and Adam Aurisano for all their hard work that went into this analysis. Thank you to the William & Mary physics professors, Jeff Nelson, Mike Kordosky and David Armstrong, for their countless advice and direction in bringing this thesis to completion. To my fellow William & Mary graduate students, especially Travis, Zak, and Katja, you have made the past few years that much more enjoyable. I am forever grateful for the friendships we have formed. To my parents, for giving me the opportunity to get to this point and to my brother and sister for always being there. And finally, to my husband, Joshua, for his confidence in me and limitless technical support. And finally to our daughter, Adelyn, you have brightened my life.

To my loving husband, Joshua, and our beautiful Adelyn.

LIST OF TABLES

1.1 Experimentally measured values of the neutrino oscillation parameters . . . 10

5.1 Oscillation paramters which are fixed in the fit for the χ^2 minimization. . . 74

5.2 $\Delta\chi^2$ values for confidence levels 1-α with m parameters 76

7.1 The number of expected neutral current events in the far detector. 88

7.2 The number of expected charged current events in the far detector. 88

7.3 R statistic with $\theta_{23} < 45°$. 89

7.4 R statistic with $\theta_{23} > 45°$. 92

7.5 Global best fit values for all free parameters. Δm^2_{34} fixed at $0.5\,\mathrm{eV}^2$. The degrees of freedom (d.o.f) correspond to the number of energy bins used in the χ^2 and is equal to 233. 93

LIST OF FIGURES

1.1 The four ν_τ CC interactions discovered by the DONUT collaboration. . . . 7

1.2 The combined result from the experiments ALEPH, DELPHI, L3, and OPAL at LEP 8

1.3 The effect of different values of Δm^2_{34} on $\mathrm{P}(\nu_\mu \to \nu_s)$ 18

2.1 A schematic of the components of the NuMI beamline. 20

2.2 For normal low energy running, the horns are separated by 10 m with a current of 185 kA. 21

2.3 The target and target vacuum canister 22

2.4 A cartoon of the MINOS planes, scintillator, and electronic readout. 24

2.5 The scintillator strips used in both MINOS detectors 25

2.6 Showing the orientation of the scintillator (white) and steel (grey) planes for both detectors. 26

2.7 The MINOS near detector at Fermilab. 31

2.8 The near detector planes. 31

2.9 The MINOS far detector. 32

3.1 he raw response (top) and the calibrated response (bottom) in ADCs for the far detector. 39

3.2 The raw response (top) and the calibrated response (bottom) in ADCs for the near detector. 40

4.1 Feynman diagram for a neutrino charged-current interaction. 45

4.2 Feynman diagram for a neutrino neutral-current interaction. 45

4.3 Energy loss of muons in copper as a function of $\beta\gamma$ over several orders of magnitude. 46

4.4 Monte Carlo simulations of the different event topologies. 47

4.5 Monte Carlo and data distribution of the number of consecutive planes. . . 49

4.6 Monte Carlo and data distribution of the fraction of the slice pulse height contained in the event. 49

4.7 Monte Carlo and data comparison of the event lengths in the far detector for neutral current events. 53

4.8 Monte Carlo and data comparison of the event lengths in the near detector for neutral current events. 53

4.9 Monte Carlo and data comparison of the track extension in the far detector for neutral current events. 53

4.10 Monte Carlo and data comparison of the track extension in the near detector for neutral current events. 53

4.11 Monte Carlo and data comparison of the number of tracks in an event in the far detector for neutral current events. 53

4.12 Monte Carlo and data comparison of the number of tracks in an event in the near detector for neutral current events. 53

4.13 All event vertices observed in the far detector for neutral-current selected events. 54

4.14 The efficienty and purity of the neutral current event selection. 55

4.15 All event vertices observed in the far detector for charged-current selected events. 56

4.16 The roID distribution in the near detector. 57

4.17 he efficiency and purity of the charged current event selection. 58

5.1 MINOS complete data set between 2005 and 2012. 61

5.2 Far detector neutral current spectrum from the MINOS 2011 sterile neutrino search. 62

5.3 Far detector charged current spectrum from the MINOS 2011 sterile neutrino search. 62

5.4 Reconstructed energy vs. L(km)/E_{true}(GeV) 2D histogram. 64

5.5 A ratio of the fake far detector data spectrum and the far detector prediction. 66

5.6 A ratio of the fake far detector data spectrum and the far detector prediction. 67

5.7 The black line is showing the probability curve when when each of the 100 iterations over each energy bin is used. 68

5.8 The black line is showing the probability curve when each of the 100 iterations over each energy bin is used. 69

5.9 A ratio of the fake far detector data spectrum and the far detector prediction. 70

5.10 The ND NC monte carlo spectra before and after the inclusion of ND oscillations. 71

5.11 The ND CC monte carlo spectra before and after the inclusion of ND oscillations. 71

5.12 The FD NC prediction before and after the inclusion of ND oscillations. . . 72

5.13 The FD CC prediction before and after the inclusion of ND oscillations. . . 72

5.14 A χ^2 surface for the Δm^2_{34} vs. θ_{24} parameter space. 73

5.15 The black curve represents the four flavor probability for $\nu_\mu \rightarrow \nu_s$ at $\Delta m^2_{34} = 40.99\text{eV}^2$ at the far detector baseline. 74

5.16 An example of averaging a $\sin^2(x)$ probability over an energy bin of width W (arbitrarily scaled to π). 75

5.17 An example of averaging a $\sin^2(x)$ probability over an energy bin of width W (arbitrarily scaled to π). 75

5.18 A χ^2 surface for the θ_{24} vs. θ_{34} phase space is shown for data. 76

5.19 1D χ^2 distribution for θ_{23} when different parameters are varied. 77

7.1 Neutral current energy spectum in the far detector for 10.56×10^{20} POTs. 90

7.2 Charged current energy spectum in the far detector for 10.56×10^{20} POTs. 90

7.3 Neutral current energy spectum in the far detector for 10.56×10^{20} POTs. 91

7.4 Charged current spectum in the far detector for 10.56×10^{20} POTs. 91

7.5 Contours representing the 90% C.L. for these pair of parameters with a four flavor oscillation fit. 94

7.6 Projections of $\Delta\chi^2$ as a function of the different oscillation parameters. The values of $\Delta\chi^2$ at the 68% and 90% C.L. are also shown. 95

7.7 LSND, MiniBooNE appearance signal compared to Karmen and Bugey. . . 96

8.1 The χ^2 surface of Δm^2_{34} vs. θ_{24}. The best fit point is found at $\Delta m^2_{34} = 56\,\mathrm{eV}^2$. 98

8.2 Near detector $\nu_\mu \to \nu_s$ oscillation probability curve. 100

8.3 Far detector $\nu_\mu \to \nu_s$ oscillation probability curve. 100

STERILE NEUTRINO SEARCH WITH MINOS

CHAPTER 1

Neutrinos

Neutrinos [1] were first proposed as a 'desperate remedy' to save the conservation of energy. This chapter explores the early beginnings of neutrinos and the key experiments that determined their existence and properties.

1.1 Historical Perspective

At the end of the 19^{th} century, it was observed that β-decay was an emission of an electron from a radioactive nucleus. As such, the emergent electron was expected to be monoenergetic with its kinetic energy approximately equal to the released energy. However, in 1914 James Chadwick showed that the energy spectrum of the emitted electron was instead continuous [2]. Several solutions to this problem were proposed. One possible explanation was that the electron was losing energy into the medium containing the radioactive nuclei. However, this was proven false by Ellis and Wooster in 1927 [3]. Ellis and Wooster performed a calorimetric β-decay experiment and found that the energy detected in β-decay was smaller than the total released energy. To explain this phenomenon, Neils Bohr suggested that energy was not conserved for individual decays.

On December 4, 1930, Wolfgang Pauli wrote a letter to a conference on radioactivity in Tübingen as "a desperate remedy to save the exchange theorem of statistics and the law of conservation of energy [4]." Pauli proposed that, in fact, there was another particle emitted alongside the electron in β-decay that was electrically neutral, had spin $\frac{1}{2}$, and had mass no larger than 1% of the proton mass. He called this particle the neutron [4]. In 1932, Chadwick discovered the modern neutron through experiments involving α radiation. However, it was clear that this neutral particle was too heavy to be Pauli's neutron [5].

In 1934, Enrico Fermi proposed a theory of β-decay as a process of a quantum transition of a neutron into a proton with the creation of an electron-neutrino pair:

$$n \to p + e^- + \nu. \tag{1.1}$$

His theory incorporated Pauli's particle, but he renamed it the neutrino to avoid confusion [6]. Shortly afterwards, Bethe and Peierls obtained the first estimation of the cross section of neutrino reactions. They found that $\sigma < 10^{-44}\,\mathrm{cm}^2$, which corresponds to a neutrino absorption length in solid matter larger than $10^{14}\,\mathrm{km}$. In their paper, they concluded that "there is no practically possible way of observing the neutrino" [7]. The neutrino would be considered undetectable until 1946, when Pontecorvo proposed a radiochemical method based on the reaction [8]

$$\bar{\nu} + {}^{37}\mathrm{Cl} \to e^- + {}^{37}\mathrm{Ar}. \tag{1.2}$$

The Cl-Ar method would later be used by Davis to observe solar neutrinos.

1.2 Experimental Detection

Neutrinos were discovered by Reines and Cowan in 1956 [9]. They used antineutrinos from the Savannah River nuclear reactor to detect neutrinos through the inverse β-decay:

$$\bar{\nu} + p \rightarrow e^{+} + n. \tag{1.3}$$

Their detector was a liquid scintillator loaded with cadmium chloride as a neutron absorber. About 10^{20} antineutrinos were emitted per second from the nuclear reactor. This gave a huge flux of about $10^{13}\,\mathrm{cm^{-2}s^{-1}}$ antineutrinos [9]. The positron created in the process described in Equation 1.3 quickly finds an electron and pair-annihilates producing two photons with energies of approximately 0.51 MeV and opposite momenta. This was a distinct signature of the reaction, however, it was not enough proof of a neutrino interaction. Reines and Cowan, therefore, arranged to detect the neutron in Equation 1.3 as well. The neutron would slow down in the target and then get captured by the cadmium nucleus within 5μs through the following process

$$n + {}^{108}\mathrm{Cd} \rightarrow {}^{109}\mathrm{Cd} + \gamma. \tag{1.4}$$

The neutrino events now had a distinct signature of two photons of opposite momenta from the e^{+}-e^{-} annihilation along with a delayed photon from the neutron capture by the cadmium in the scintillator [9]. In 1995, Reines received the Nobel Prize for the detection of the neutrino.

Shortly thereafter, Davis performed an experiment that tested Pontecorvo's radiochemical method according to

$$\bar{\nu} + {}^{37}\mathrm{Cl} \rightarrow e^{-} + {}^{37}\mathrm{Ar}. \tag{1.5}$$

However, no ^{37}Ar atoms were found [10], showing that although antineutrinos could produce a positron through inverse β-decay as per the Reines-Cowan experiment, they could not produce electrons. This demonstrated that neutrinos and antineutrinos were distinct and that lepton number was conserved [10].

Proof that a second type of neutrino existed came from an experiment at Brookhaven in 1962 performed by Lederman, Schwartz, and Steinberger [11]. It was the first experiment to use accelerator neutrinos. A beam of π^+'s was obtained by colliding protons of 15 GeV with a Be target. The π^+'s were allowed to decay in a 21m long channel, producing neutrinos according to

$$\pi^+ \rightarrow \mu^+ + \nu. \tag{1.6}$$

At the end of the decay channel, 13.5 m of iron was used as shielding material to absorb the charged particles while the neutrinos passed through. A 10 ton aluminum spark chamber was used as the neutrino detector to detect the production of the charged leptons as the neutrinos interacted. If there was only one type of neutrino, the interactions in the detector would produce electrons approximately half of the time and muons the other half. However, 29 muon events were detected and the observed 6 electron events could be explained by the background suggesting that ν_μ and ν_e neutrinos were distinct. For a beam of ν_μ neutrinos, only muons would be produced according to

$$\nu_\mu + N \rightarrow \mu^- + X \tag{1.7}$$

and

$$\nu_\mu + N \rightarrow \mathrm{e}^- + X \tag{1.8}$$

was not allowed. In 1988, Lederman, Schwartz, and Steinberger received the Nobel Prize for their discovery of the muon neutrino.

In the meantime, Davis continued using the radiochemical method of neutrino detection in an attempt to detect solar neutrinos according to the reaction

$$\nu_e + {}^{37}\mathrm{Cl} \rightarrow \mathrm{e}^- + {}^{37}\mathrm{Ar}. \tag{1.9}$$

Davis succeeded at detecting solar neutrinos, however, his result in the late 1960's showed that the observed flux of solar neutrinos was two to three times smaller than the predicted flux, thus creating the solar neutrino problem [12]. The predicted flux was calculated based on the nuclear fusion proton-proton reaction in the Sun. The experiment ran continuously between 1970 and 1994 with a consistently low measurement of the rate of solar neutrinos. Years later, the solar problem would be understood by the discovery of neutrino mass and oscillations.

In experiments performed at the e^+ - e^- collider Stanford in 1975-77 by M. Perl et. al [13], the third lepton $\tau^{\pm}$ was discovered. This led to the belief that a third neutrino, ν_τ, must also exist. In 2000, the DONUT collaboration [14] at Fermilab observed the tau neutrino through the production of τ in the process

$$\nu_\tau + N \rightarrow \tau + X. \tag{1.10}$$

A high intensity beam of neutrinos produced at Fermilab was fired at a target with alternating iron plates and layers of emulsion. When a charged particle passes through the emulsion, a permanent record of its path is recorded, allowing measurements of decays of short lived particles, such as the τ. The signature event in the emulsion was a track with a kink since the tau would decay and could produce a single charged particle at an average distance of 2 mm from the production point [14]. Four such events were discovered, shown in Figure 1.1.

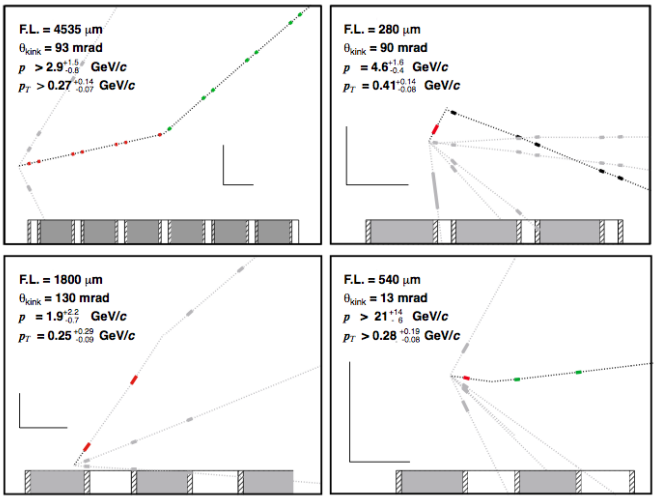

FIG. 1.1: The four ν_τ CC interactions discovered by the DONUT collaboration. The bar at the bottom represents the target, steel (shaded), emulsion (cross-hatched), and plastic (no shading) [14].

The number of light, active neutrinos is constrained by measurements of the width of the Z^0 resonance. In the 1990s, four LEP (Large Electron-Positron) collider experiments at CERN (ALEPH, DELPHI, L3, OPAL) observed the reaction:

$$e^+e^- \rightarrow Z^0 \rightarrow q\bar{q}, l^+l^-, \nu\bar{\nu}. \tag{1.11}$$

Here, the electron and positron annihilate to form a Z^0, which decays into a quark-antiquark pair ($q\bar{q}$), a charged lepton pair (l^+l^-) or a neutrino-antineutrino pair (e^+e^-). The width of the Z^0 resonance is the sum of the partial widths of these channels and thus will increase if there are more available channels, such as if there was a fourth light, active neutrino. A fit to the width of the Z^0 resonance finds the number of light, active neutrinos to be [15]:

$$N_\nu = 2.984 \pm 0.008. \tag{1.12}$$

The result is depicted in Figure 1.2.

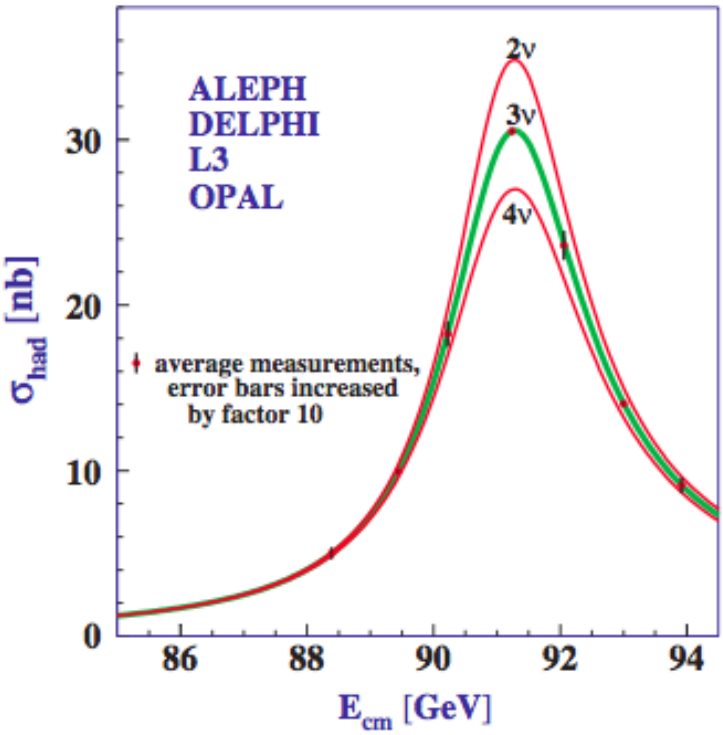

FIG. 1.2: The combined result from the experiments ALEPH, DELPHI, L3, and OPAL at LEP showing the measurement of the hadron production cross section around the Z^0 mass resonance. The different curves show the prediction for the cross section with either 2, 3, or 4 active neutrinos. The result constrained the number of light neutrinos to $N_\nu = 2.984 \pm 0.008$ [15].

1.3 Modern Evidence

The first incontrovertible evidence of neutrino oscillations came in 1998 from the Super-Kamiokande collaboration [16]. Super-Kamiokande measured the number of neutrinos that were produced in the earth's atmosphere. Neutrinos that were detected coming from above would travel distances of 20 - 500 km while neutrinos detected from below would pass through the earth and travel distances of 500 - 12,000 km. Atmospheric neutrinos have energies on the order of 1 GeV. It was measured that the number of muon neutrinos coming from below the detector was about two times smaller than the muon neutrinos coming from above. It was therefore proven that the number of muon neutrinos depended on the distance through which they traveled from their production point in the

earth's atmosphere. These results were confirmed by both K2K [17] and MINOS [18], two long-baseline accelerator experiments.

In 2002, the SNO [19] solar neutrino experiment proved that solar ν_e's would oscillate into ν_μ and ν_τ while traveling to earth. SNO detected high energy solar neutrinos greater than 10 MeV from ^{8}B-decay through charged-current and neutral-current interactions. Charged-current interactions determined the flux of solar ν_e's on earth while neutral-current interactions determined the flux of all flavor neutrinos. The experiment showed that the flux of solar ν_e's was approximately three times smaller than the total flux of ν_e, ν_μ, and ν_τ. Only electron neutrinos are produced in the Sun, according to

$$p + p \rightarrow d + e^+ + \nu_e. \tag{1.13}$$

Therefore, the other flavors are the result of neutrino oscillations.

In 2002-2004, KamLAND [20] obtained evidence for neutrino oscillations of reactor $\bar{\nu_e}$. Fifty five reactors at an average distance of about 170km from the KamLAND detector were used to detect $\bar{\nu_e}$'s. It was found that the total number of $\bar{\nu_e}$ events was about 60% of the total number predicted.

Most recently, in 2012, the Daya Bay [21] experiment confirmed three flavor neutrino oscillation effects by measuring the final unknown active neutrino mixing angle, θ_{13}. Daya Bay observed $\bar{\nu_e}$ disappearance using six Gd-doped liquid scintillator detectors. The $\bar{\nu_e}$'s were generated by six reactors. The following inverse beta decay was searched for and observed in Daya Bay:

$$\bar{\nu_e} + p \rightarrow n + e^+. \tag{1.14}$$

Their event selection aimed to identify events which included the detection of a prompt positron and a delayed neutron. The positron carries most of the neutrino energy and

Parameter	Measured Value
Δm^2_{12}	$7.59 \times 10^{-5}\,\mathrm{eV}^2$
Δm^2_{23}	$2.40 \times 10^{-3}\,\mathrm{eV}^2$
θ_{13}	8.6°
θ_{12}	34.38°
$\sin^2(\theta_{23})$	0.43

TABLE 1.1: Experimentally measured values of the neutrino oscillation parameters [22].

annihilates quickly while the average capture time of a neutron in Gd-doped liquid scintillator is $28\,\mu$s. Table 1.1 depicts the experimentally measured values of the mass splittings and mixing angles.

1.4 Neutrinos in the Standard Model

The Standard Model of particle physics was completed in the mid-1970s. It is very successful in describing electromagnetic and weak interactions between fundamental particles of matter and is often referred to as the theory of almost everything [22]. However, it falls short in predicting properties of neutrinos, mainly because it predicts that neutrinos are massless. The following properties are predicted by the Standard Model:

1. Neutrinos have a mass of exactly zero.
2. There are exactly three neutrino flavors, corresponding to each of the three charged leptons.
3. Neutrinos and antineutrinos are distinct particles.
4. Neutrinos have left-handed helicity while antineutrinos have right-handed helicity.

However, experimental data now suggest that neutrinos oscillate between the three active flavors, a phenomenon that cannot be explained by massless neutrinos. In fact, the idea of neutrino oscillations was first proposed in 1958 by Pontecorvo who suggested that neutrinos

had mass and could oscillate from neutrinos to anti-neutrinos [23]. This idea was later extended to allow oscillations between the different neutrino flavors [24]. The neutrino oscillations phenomenon will be further explored in the following section.

1.5 Neutrino Oscillations

Neutrinos can come in three different flavors, ν_e, ν_μ, ν_τ, based on their charged lepton partners, e, μ, τ. The three flavors are eigenstates of the weak force, the only interaction in which neutrinos participate. Although they are produced and detected in their flavor eigenstates, neutrinos propagate through space as a superposition of their mass eigenstates, ν_1, ν_2, ν_3. Combinations of mass eigenstates propagate with slightly different frequencies brought on by the mass differences, hence they develop different phases with distance travelled. Interference between the mass eigenstates results in an oscillation between the flavors.

For simplicity, considering only the two flavor case, it is possible to represent the flavor eigenstates as linear combinations of the two mass eigenstates,

$$\begin{pmatrix} \nu_\mu \\ \nu_e \end{pmatrix} = \begin{pmatrix} \cos\theta & \sin\theta \\ -\sin\theta & \cos\theta \end{pmatrix} \begin{pmatrix} \nu_1 \\ \nu_2 \end{pmatrix} \tag{1.15}$$

where θ is the mixing angle. Assuming that a neutrino is ultrarelativistic and propagates as a plane-wave, the time evolution of the ν_μ state can be expressed as [25],

$$\mid \nu(L)\rangle = \cos\theta e^{-im_1^2 L/2E} \mid \nu_1\rangle + \sin\theta e^{-im_2^2 L/2E} \mid \nu_2\rangle \tag{1.16}$$

where t is the time and L is the distance travelled. It is easy to show that the survival

probability for one flavor of neutrino is

$$P(\nu_\alpha \to \nu_\alpha) = |\ \langle \nu_\alpha \mid \nu(L) \rangle\ |^2 \tag{1.17}$$

$$= 1 - \sin^2(2\theta) \sin^2\left(\tfrac{\Delta m^2 L}{4E}\right) \tag{1.18}$$

where $\Delta m^2 \equiv m_2^2 - m_1^2$. Appearance experiments look for a greater than expected number of neutrinos of a specific flavor relative to what was produced at the neutrino source. The appearance probability for one flavor oscillating to another can be shown to be

$$P(\nu_\alpha \to \nu_\beta) = \sin^2(2\theta) \sin^2\left(\tfrac{\Delta m^2 L}{4E}\right) \tag{1.19}$$

Many experimental measurements can be interpreted in the two flavor approximation. Neutrinos, however, exist in three flavors not just two. The mass and flavor eigenstates can be related by a 3x3 PMNS unitary mixing matrix, $U_{\alpha i}$,

$$\mid \nu_\alpha \rangle = \sum_i U^*_{\alpha i} \mid \nu_i \rangle \tag{1.20}$$

where $\nu_\alpha = (\nu_e, \nu_\mu, \nu_\tau)$, $\nu_i = (\nu_1, \nu_2, \nu_3)$ and the mixing matrix for three flavors is given by,

$$U = \begin{pmatrix} 1 & & \\ & c_{23} & s_{23} \\ & -s_{23} & c_{23} \end{pmatrix} \begin{pmatrix} c_{13} & & s_{13}e^{-i\delta} \\ & 1 & \\ -s_{13}e^{+i\delta} & & c_{13} \end{pmatrix} \begin{pmatrix} c_{12} & s_{12} & \\ -s_{12} & c_{12} & \\ & & 1 \end{pmatrix} \begin{pmatrix} 1 & & \\ & e^{i\alpha} & \\ & & e^{i\beta} \end{pmatrix} \tag{1.21}$$

where $c_{ij} \equiv \cos\theta_{ij}$, $s_{ij} \equiv \sin\theta_{ij}$, δ is the CP (charge-parity) symmetry violating phase, and α and β are the Majorana phases. The Majorana phases are not observable in oscillation experiments and are therefore dropped from the oscillation probability calculations.

Experiments measure the probability that a neutrino created with flavor ν_α will be detected some distance away with flavor ν_β. The neutrino oscillation probability is given

by

$$P(\nu_\alpha \to \nu_\beta) = \mid \sum_j U^*_{\alpha j} \mathrm{e}^{-im_j^2 L/2E} U_{\alpha j} \mid^2 \tag{1.22}$$

Expanding and simplifying, the three flavor neutrino oscillation probability can be written as [26],

$$\begin{aligned} P(\nu_\alpha \to \nu_\beta) = \delta_{\alpha\beta} - 4 \sum_{i>j} \Re(U_{\beta i} U^*_{\beta j} U^*_{\alpha i} U_{\alpha j}) \sin^2 \left(\frac{\Delta m^2_{ij} L}{4E} \right) \\ + 2 \sum_{i>j} \Im(U_{\beta i} U^*_{\beta j} U^*_{\alpha i} U_{\alpha j}) \sin \left(\frac{\Delta m^2_{ij} L}{2E} \right) \end{aligned} \tag{1.23}$$

1.6 LSND Anomaly and Sterile Neutrinos

Most experimental data is in agreement that there are three neutrino flavors and two neutrino mass splittings. However, in 1996, the Liquid Scintillator Neutrino Detector (LSND) at the Los Alamos Meson Physics Facility (LAMPF), published a result that could not be explained with only two mass splittings [27]. Instead, this result was interpreted as the existence of a third mass splitting and fourth neutrino flavor. Because LEP experiments which measured the width around Z^0 indicated that there were only three active neutrinos that coupled to the Standard Model weak interaction, this fourth hypothetical neutrino could not couple to the Standard Model weak interaction, and is therefore termed *sterile*.

The primary goal of LSND was to search for $\bar{\nu}_\mu$'s oscillating into $\bar{\nu}_e$'s. LSND was a 167 ton tank filled with mineral oil doped with scintillator. The mixture allowed for detection of both Cherenkov light and isotropic scintillator light. About 25% of the surface inside the tank walls was covered by 1220 8" PMTs [28]. The detector was located 30m from the neutrino source. The neutrinos were produced by the LAMPF by accelerating protons to 800MeV and aiming them at a series of targets [28]. The main neutrino flux comes from

π^+'s which came to rest inside the target and decayed through the sequence

$$\begin{aligned} \pi^+ &\rightarrow \mu^+ + \nu_\mu \\ \mu^+ &\rightarrow e^+ + \nu_e + \bar{\nu}_\mu. \end{aligned} \tag{1.24}$$

The energies of the $\bar{\nu}_\mu$'s ranged up to 52.8 MeV. The signal $\bar{\nu}_e$ events are searched for through the reaction $\bar{\nu}_e + p \rightarrow e^+ + n$. The $\bar{\nu}_e$ component in the beam was LSNDs biggest background occurring from the symmetrical decay chain starting with a π^-. This background was suppressed by three factors,

- π^+'s were produced eight times more than π^-'s,
- 95% of the π^-'s produced would come to rest in the beam stop and shielding and be absorbed before they decayed,
- 88% of μ^- from π^- decay in flight were captured by atomic orbit.

LSND published a result in 1996 [27]. They found a significant excess of $\bar{\nu}_e$ events above the background. The excess was interpreted as a signal for $\bar{\nu}_\mu \rightarrow \bar{\nu}_e$ oscillations. Due to the energy and baseline of the LSND experiment, such an oscillation would require a mass splitting on the order of 1eV^2, significantly larger than the mass splittings found for solar and atmospheric neutrinos. In order to be compatible with other neutrino experiments and the LEP Z width results, the size of the splitting was explained with the presence of a fourth, sterile neutrino.

A large portion of the allowed LSND parameter space was ruled out by other experiments sensitive to $\bar{\nu}_\mu \rightarrow \bar{\nu}_e$ oscillations. Because the LSND result was not entirely ruled out, it prompted the construction of the MiniBooNE experiment at Fermilab [29]. MiniBooNE is a 800 ton spherical tank filled with mineral oil in the Fermilab Booster neutrino beam. The beam is produced from 8 GeV protons incident on a beryllium target. Particles

passing through the MiniBooNE detector can emit both Cherenkov and scintillator light. The ν_μ energy spectrum peaks at 700 MeV, while the detector is 541m from the source of the beam, giving a similar L/E to the LSND experiment. In MiniBooNE's first published results in 2007 [30] which ran in neutrino mode, no significant excess of events was found for the energy region of 475-1250 MeV, ruling out the LSND 90% C.L. allowed region at 90% C.L. The MiniBooNE and LSND results are compatible in the more complex two sterile neutrino plus three active neutrino model. The experiment was rerun in antineutrino mode, however, the results were inconclusive at ruling out oscillations at the LSND mass scale.

Other anomalies resulting from reactor and radioactive source neutrino experiments have arisen since LSND. A detailed calculation of the reactor $\bar{\nu_e}$ fluxes [31], resulted in a reactor neutrino anomaly from the re-analysis of the short baseline reactor neutrino oscillation data using the new fluxes [32]. The new fluxes are found to be larger which leads to a possible disappearance of reactor $\bar{\nu_e}$. Radioactive source neutrino experiments also showed a deficit in the measured fluxes. The Gallium Anomaly arises from the GALLEX [33, 34] and SAGE [35, 36] experiments showing hints of ν_e disappearance at short baselines.

1.6.1 Four-flavor oscillations

In order to incorporate the LSND anomaly into neutrino oscillations, a 3+1 model in which the sterile neutrino mass is much larger than the active neutrino mass can be used. An extension to the neutrino oscillation probability to include a fourth neutrino flavor can be made in the following manner,

$$P(\nu_\alpha \rightarrow \nu_\beta) = \mid \sum_{j=0}^{4} U^*_{\alpha j} U_{\beta j} e^{-i m_j^2 L/2E} \mid^2 \tag{1.25}$$

Expanding the expression gives,

$$P(\nu_\alpha \to \nu_\beta) = \mid U^*_{\alpha 1}U_{\beta 1} + U^*_{\alpha 2}U_{\beta 2}e^{-i(m^2_2-m^2_1)L/2E} + U^*_{\alpha 3}U_{\beta 3}e^{-i(m^2_3-m^2_1)L/2E} + U^*_{\alpha 4}U_{\beta 4}e^{-i(m^2_4-m^2_1)L/2E} \mid^2 . \tag{1.26}$$

To simplify, define $\Delta_{jk} = \frac{(m^2_j-m^2_k)L}{4E}$ and eliminate $U^*_{\alpha 1}U_{\beta 1}$ through the unitarity of the mixing matrix:

$$\sum_j U^*_{\alpha j}U_{\beta j} = \delta_{\alpha\beta} \tag{1.27}$$

$$U^*_{\alpha 1}U_{\beta 1} = \delta_{\alpha\beta} - U^*_{\alpha 2}U_{\beta 2} - U^*_{\alpha 3}U_{\beta 3} - U^*_{\alpha 4}U_{\beta 4} \tag{1.28}$$

to give

$$P(\nu_\alpha \to \nu_\beta) = \mid \delta_{\alpha\beta} + U^*_{\alpha 2}U_{\beta 2}(e^{-i2\Delta_{21}} - 1) + U^*_{\alpha 3}U_{\beta 3}(e^{-i2\Delta_{31}} - 1) + U^*_{\alpha 4}U_{\beta 4}(e^{-i2\Delta_{41}} - 1) \mid^2 \tag{1.29}$$

and finally, using $\sin(\theta) = \frac{e^{i\theta}-e^{-i\theta}}{2i}$, the four flavor neutrino oscillation probability can be written as

$$P(\nu_\alpha \to \nu_\beta) = \mid \delta_{\alpha\beta} - 2iU^*_{\alpha 2}U_{\beta 2}\sin(\Delta_{21})e^{-i\Delta_{21}} - 2iU^*_{\alpha 3}U_{\beta 3}\sin(\Delta_{31})e^{-i\Delta_{31}} - 2iU^*_{\alpha 4}U_{\beta 4}\sin(\Delta_{41})e^{-i\Delta_{41}} \mid^2 \tag{1.30}$$

The 4x4 mixing matrix now contains six mixing angles, three mass-squared differences and three CP-violating phases.

For MINOS, in this model, oscillations can occur at the far detector, at the near detector, or in between the two detectors, depending on the value of the sterile mass splitting. Figure 1.3 shows examples of the predicted four flavor oscillation probability

as a function of E for different values of Δm^2_{34}. The sterile mixing angles were set to the limits of the previous MINOS sterile neutrino analysis and the standard three flavor parameters were fixed at the best fit values known at the time this thesis was written.

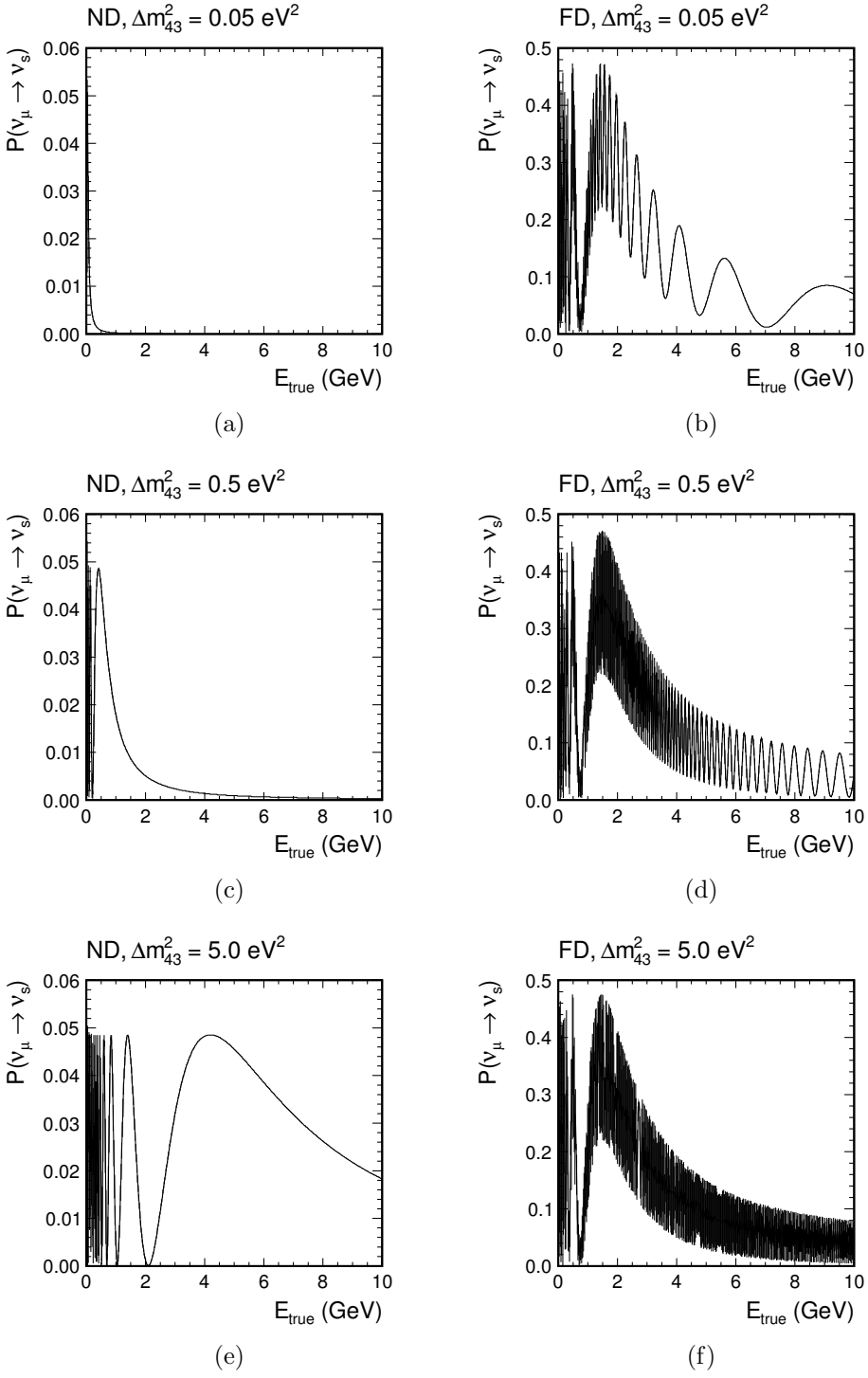

FIG. 1.3: The effect of different values of Δm^2_{34} on $P(\nu_\mu \rightarrow \nu_s)$ at both the near (a, c, e) and far (b, d, f) detectors.

CHAPTER 2

The MINOS Experiment

MINOS, the Main Injector Neutrino Oscillation Search, is a long-baseline neutrino oscillation experiment in the NuMI muon neutrino beam at the Fermi National Accelerator Laboratory in Batavia, IL. It consists of two detectors, a near detector positioned 1 km from the source of the beam and a far detector 735 km away. The neutrino beam is produced by 120GeV protons extracted from the Main Injector at Fermilab and aimed at the Soudan Underground Laboratory mine in northern Minnesota the site of the far detector. The neutrino energy spectrum is measured at the near detector then extrapolated to the far detector. The use of two detectors allows for the cancellation of certain systematic uncertainties such as the neutrino interaction cross section and the beam flux. An observation of an energy dependent deficit of the rate of muon neutrinos at the far detector is indicative of neutrino oscillations. MINOS is primarily designed to observe muon neutrino disappearance and to make precision measurements of the mixing parameters Δm^2_{23} $(m^2_3 - m^2_2)$ and $\sin^2(2\theta_{23})$. Both detectors are magnetized and consist of alternating planes of steel and scintillator strips with optical fibers in the center. They are nearly functionally identical.

2.1 NuMI beamline

The NuMI [37], Neutrinos at the Main Injector, beamline at Fermilab, was designed to meet the physics goals of long-baseline neutrino oscillation experiments. Figure 2.1 shows a schematic of the components of the NuMI beamline. To produce a beam of muon neutrinos, 120 GeV protons are extracted from the Main Injector and directed onto a long, thin graphite target, Figure 2.3, in 10μs spills. The intensity of the proton beam is

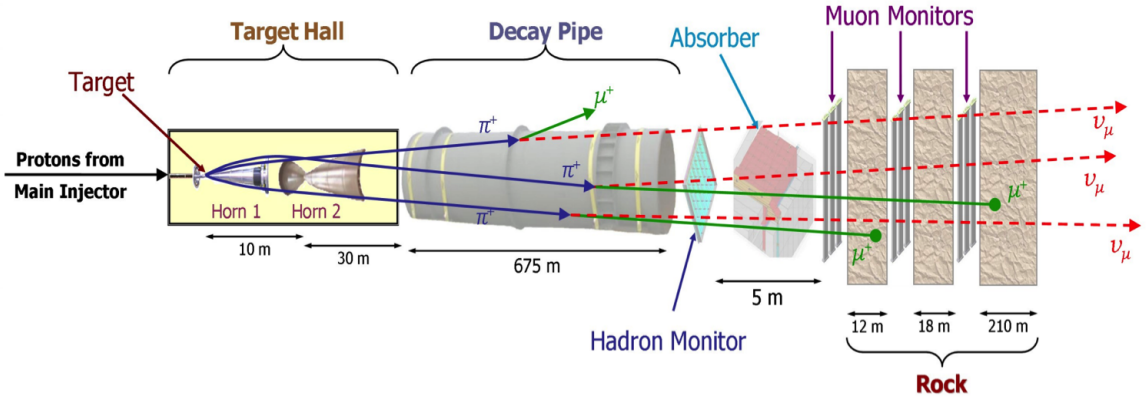

FIG. 2.1: A schematic of the components of the NuMI beamline. Protons at 120 GeV from the Main Injector hit a graphite target. Secondary pions and kaons are focused by the horns and allowed to decay to produce neutrinos in the decay pipe. Any remaining mesons are stopped by the beam stop and rock in front of the near detector.

2.1-3.0$\times 10^{13}$ [39] protons on target per spill with a cycle time of about 2.2s. The beam is bent downward by 3° to point at the far detector.

Protons interact with the nuclei in the target to produce a high flux of pions and kaons. The graphite target has dimensions of $6.4\times15\times940\,\mathrm{mm}^3$ that is segmented longitudinally into 47 fins which are water cooled at the top and bottom. The beam spot size at the target is approximately 1.2-1.5 mm [38].

Two magnetic focusing horns with parabolic shaped inner conductors are downstream of the target and act as lenses, with the focal length proportional to the pion momentum. A 185 kA pulsed current in the horns produces a maximum 30 kG toroidal field which focuses the secondary particles produced at the target by charge sign and momentum

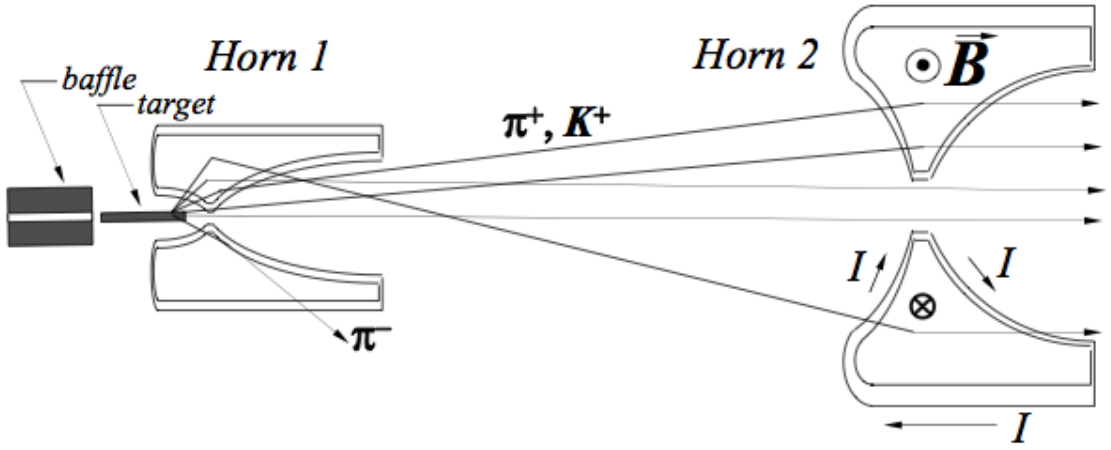

FIG. 2.2: For normal low energy running, the horns are separated by 10 m with a current of 185 kA. A collimating baffle, a 1.5 m long graphite rod with an 11 mm inner bore, upstream of the target protects the horns from direct exposure to misdirected proton beam pulses [38].

[38]. These horns focus the either positive or negative pions and kaons along the neutrino beam direction, as shown in Figure 2.2. By changing the current in the horns and the relative position of the target with respect to the first horn, it is possible to change the sign and range of momentum of the focused mesons. This allows for different neutrino and antineutrino energy configurations. The inner walls of the horns are designed as thin as possible to reduce pion absorption. The inner aluminum conductor is cooled with a water spray. In the ν_μ-beam mode, the horns are configured to focus positive mesons, and produces a beam of 91.1% ν_μ, 7.1% $\bar{\nu}_\mu$, and 1.8% ν_e and $\bar{\nu}_e$. In the $\bar{\nu}_\mu$-beam mode, the horns are configured to focus negative mesons, and produces a beam of 46.8% $\bar{\nu}_\mu$, 51.3% ν_μ, and 1.9% ν_e and $\bar{\nu}_e$ [37].

The focused pions and kaons decay while traveling through a 675 m decay pipe, the average distance a 10 GeV pion will travel before decaying. Combined with the 50 m distance from target hall to decay pipe, the pions and kaons have a total distance of 725 m to decay. The original design called for the decay pipe to be evacuated, but due to worries of implosion the decay pipe is now filled with helium. The decay pipe has a

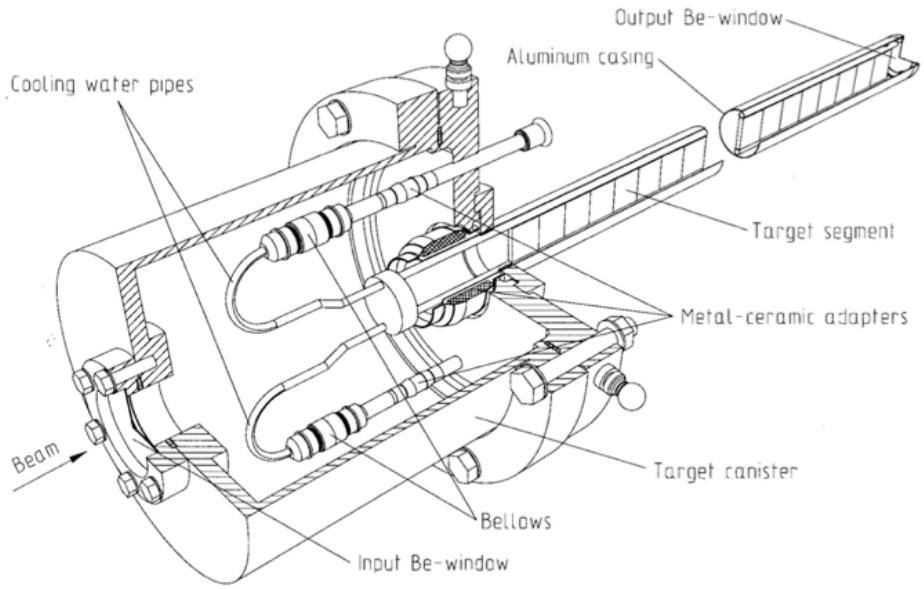

FIG. 2.3: The target and target vacuum canister [37].

radius of 1m to balance loss of particles that interact in the walls of the pipe against the cost of construction. The entrance of the decay pipe is sealed with a two piece aluminum-steel window. Concrete shielding of 2.5-3.5 m thickness surrounds the decay volume. Any remaining hadrons that did not decay and protons that did not interact in the target are stopped by a hadron absorber consisting of a water cooled aluminum core surrounded by steel and concrete followed by 240 m of dolomite rock [37].

The proton beam is monitored along its path by 24 capacitive beam position monitors. Two toroidal beam current transformers and 44 loss monitors measure the beam intensity and the beam position. Beam spot size is monitored by ten retractable segmented foil secondary emission monitors. Produced particles are monitored using ionization chambers [37]. A hadron monitor is located at the end of the decay pipe to measure the flux and spatial profile of the hadrons before they hit the hadron absorber. There are also three muon monitors, one immediately following the hadron absorber, another one after 12 m of rock, and the third after another 18 m of rock, which are used to monitor the rates and

spatial profiles of any remaining muons in the beam [37] that are produced in the same decays as their associated neutrinos [40].

2.2 The MINOS Detectors

MINOS [41] consists of two functionally identical steel-scintillator sampling calorimeters. The near detector, at Fermilab, is 1.04 km from the target and is used to characterize the neutrino beam and its interactions. The far detector, is 735 km downstream in the Soudan Mine in northern Minnesota and is used to measure the energy spectrum at a distance away from the source of the beam. Both detectors consist of alternating planes of plastic scintillator strips and 2.54 cm thick steel plates. Figure 2.4 depicts the components of the MINOS planes. The scintillator strips in alternating planes are oriented 90° to one another to allow for three-dimensional event reconstruction, as shown in Figure 2.6. The steel planes are separated by a 5.94 cm air gap. The scintillator strips, shown in Figure 2.5, are 4.1 cm wide and 1.0 cm thick and consist of extruded polystyrene, doped with PPO and POPOP [41]. Each scintillator strip is coated with a layer of reflective titanium-dioxide (TiO_2), that retains the light within the strip until it is captured by the wavelength-shifting fiber (WLS). The WLS carries the signal to the end of the strip where it is transported to the multi-anode photomultiplier tube (PMT) by a clear fiber. Both the PMTs in the near and far detector are manufactured by Hamamatsu and have multiple pixels sharing a common photocathode. The PMTs [42] are operated at an average of 800 V and have a typical gain on the order of 10^6. Both detectors have a current-carrying coil passing through each plane which produces a toroidal magnetic field with a mean strength of 1.3 T. This allows for charge separation of μ^+ and μ^- tracks produced by charge current muon neutrino or antineutrino interactions, on an event by event basis. The coil hole is centered in the far

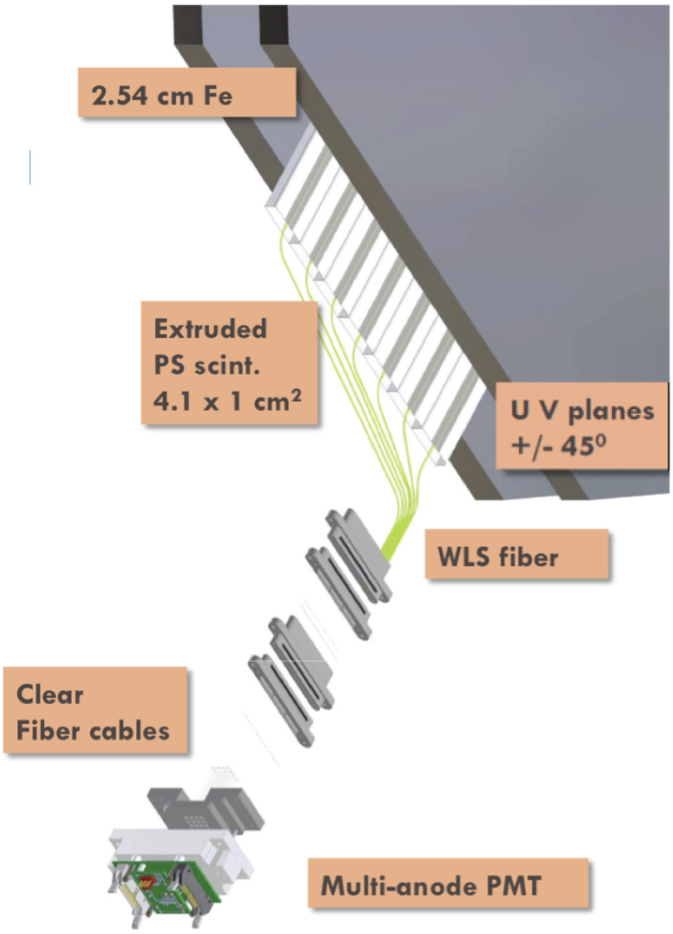

FIG. 2.4: A cartoon of the MINOS planes, scintillator, and electronic readout.

detector but is off center in the near detector. This keeps the uninstrumented section off of the beam axis which is centered on the detector.

2.2.1 Near Detector

The near detector is 1.04km from the NuMI target and 110 m underground at Fermilab. It has a total mass of 980 tons and consists of 282 steel+scintillator planes. The smaller size of the near detector is justified by the high neutrino flux at this location and cost considerations. The near detector planes are shaped as a "squashed" octagon

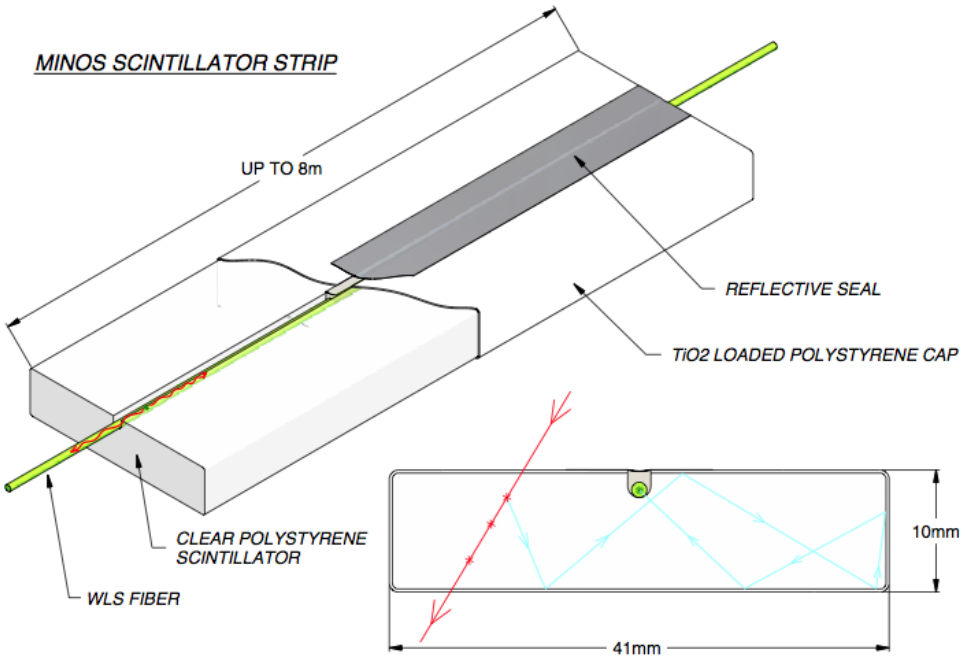

FIG. 2.5: The scintillator strips used in both MINOS detectors [41].

which is 6.2 m wide and 3.8 m high, shown in Figure 2.7. The magnet coil runs through a $30\times30\,\mathrm{cm}^2$ hole which is offset by 56 cm from the horizontal center. To induce a 1.3 T field at the neutrino-beam center, located 1.49 m to the left of the coil, the coil carries a 40 kA current [41].

The target fiducial volume is contained in the upstream 120 planes which make up the calorimeter section. This detector section is intended to measure the energy of a hadronic shower, defining the interaction vertex, and finding the upstream portion of the muon tracks. Each steel plane in the calorimeter section is instrumented with scintillator, maximizing the energy resolution. Four out of five of the scintillator planes are partially instrumented with only 64 scintillator strips per plane covering a $6.0\mathrm{m}^2$ area. The fifth plane is fully instrumented, having 96 scintillator strips covering the full $13.2\mathrm{m}^2$ area of the steel plane. The planes are readout on one side by 64 anode photomultiplier tubes

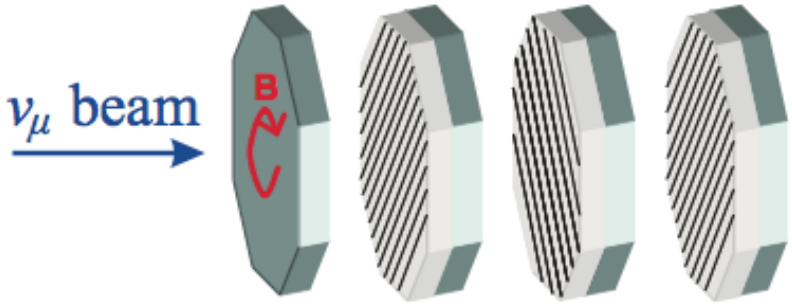

FIG. 2.6: Showing the orientation of the scintillator (white) and steel (grey) planes for both detectors. Not to scale.

(PMTs), with each pixel reading out one fiber [42]. To maximize light output, the other end of the strip is mirrored. Each strip is read out independently in the calorimeter section.

The downstream part of the detector, consisting of 160 planes, makes up the spectrometer section intended for measuring the momentum of long muon tracks. As a cost-saving measure, only every fifth plane is fully instrumented with scintillator. There are no partially instrumented planes in the spectrometer section. For additional cost savings, the signals from four adjacent strips are summed onto one electronics channel. This is resolved during event reconstruction by extrapolating the muon track found in the calorimeter section. Figure 2.8 shows the geometry of the near detector and the partially and fully instrumented planes. An average of 16 events per trigger are collected at the near detector for every 10μs spill in the normal intensity, approximately 10^{13} POT/spill, low-energy beam. Events that originate in the calorimeter section can be fully reconstructed.

Near Detector Electronics

Due to the much higher flux of neutrinos at the near detector, the electronics have to be much faster than at the far detector. In order to distinguish all neutrino events in a spill, the near detector electronics must be capable of digitizing continuously at a frequency of 53MHz to match the rate of the Fermilab Main Injector, and have zero deadtime during

the entire spill. Current from an anode of the photomultiplier tubes (PMTs) is received and integrated by the Fermilab designed Charge-to-Current Encoder (QIE) [43]. The QIE splits the current into binary weighted ranges $\frac{1}{2}$, $\frac{1}{4}$, $\frac{1}{8}$, etc. down to $\frac{1}{128}$. Splitting the current is achieved by pulling the current through 128 identical bipolar transistors over 8 capacitors and then grouping the collectors together in a binary fashion. There is a bias current present when there is no input current from the PMT. The capacitors are reset for one clock cycle then the charge is integrated during the integration cycle. During the comparison cycle, the integrated current is split into ranges as described above and the capacitor voltages are buffered and driven to a set of comparators where they are compared with preset threshold voltages. Due to the configuration of the bias current and the split ratios, only one capacitor is selected to be within the predetermined range. The selected capacitor voltage is digitized by an analog to digital converted (ADC) on the output cycle. The process then repeats itself. In order for the system to have no deadtime, the QIE has four sets of capacitors at each range. Charge is integrated and processed every 18.8ns.

The QIE, ADC, and a FIFO (First In First Out) buffer large enough to hold the output data from the whole spill are all mounted on a MENU board. There are 16 MENUs on a MINDER, a motherboard with the functions of analog input signal routing, power distribution, calibration, clocking, control, and data readout. Up to eight MINDERs are mounted on a MASTER. The MASTER linearizes the signal using a lookup table and sends the results to a VME computer and ultimately to the data acquisition system (DAQ) [43], as described in Section 2.3.

2.2.2 Far Detector

The far detector is 735 km from the NuMI target and 705 m underground in Soudan, MN, Figure 2.9. It has a total mass of 5400 ktons and consists of 486 steel planes which

are 8 m wide and in the shape of a regular octagon. The planes are divided into two supermodules which are separated by 1.1 m. Each supermodule has an independently controlled magnet coil which carries a 15.2 kA current to induce an average field of 1.27 T. Every plane is fully instrumented [41]. In the far detector, due to the larger attenuation along the longer strip, the signal from the WLS is readout at both ends by 16-anode PMTs.

Far Detector Electronics

The neutrino event rate at the far detector is much lower than at the near detector. Light collected by the WLS fibers is readout from both ends of the plane by 16-anode PMTs [44]. Eight fibers are connected to each pixel. This ambiguity is resolved at reconstruction time using the fact that the optical summing pattern is different at each end of each strip. The multiplexing pattern is different at each end which allows the determination of the correct track location. The far detector electronics [44] are optimized for low neutrino rates and a signal dominated by noise. Each PMT is readout by a VA chip mounted on a VA front-end boards (VFB). There are 3 VA chips on each VFB. The VFB also includes an ASDLite chip which is used to compare dynode signals from the PMTs to a programmable threshold and is used for time-stamping and triggering readout. In order to have good efficiency of accepting single photoelectrons (pe), the threshold is set at one third of the mean amplitude of a single pe. Two VFBs are connected to a VA Mezzanine Module (VMM) which includes an ADC which digitizes the multiplexed signal from the VA chip. Six VMMs are mounted onto a VA readout controller (VARC) which controls the signal digitalization, triggering, time-stamping and bias of the VA chip. The VARC receives and timestamps the discriminated dynode signal of each PMT. The delay time is around 500ns after the trigger signal is received. To reduce dead time due to dark noise in the PMTs and fiber noise from the scintillator, a 2-out-of-36 trigger is used. Digitization of events only occurs if at least 2 dynodes from 2 different PMTs in the same VARC receive

a signal within a 400ns window. Three VARCs are mounted in a VME crate. There are 16 VME crates to readout the 22,000 electronics channels and send the signal to the Data Acquisition System (DAQ).

2.3 Data Acquisition System

The data acquisition systems (DAQ) for the near and far detectors are functionally identical. They differ in their front-end software to accommodate the different front-end electronics. The DAQ reads out data continuously without triggering and with no dead-time. The data is then consolidated and transferred to an array of trigger processors that time sort the data and select physics events. Up to four Read Out Processors (ROPs) are responsible for acquiring data from the front-end electronics. There are sixteen ROPs at the far detector which support a mean data rate of 2.5MB/s from the front-end electronics [45]. The near detector has eight ROPs which transfer data at a rate of 5MB/s. Data is read from alternating buffers in the front-end electronics, which allows digitization to continue during readout and thus incurring no dead-time. The readout is synchronized across all front-end crates via the Timing System Central Unit (TCU). The ROPs are connected to a PCI Vertical InterConnect (PVIC) system responsible for transferring the data via a multi-node, high-speed PCI-to-PCI interconnect. The data is transferred to PCs called Branch Readout Processors (BRP). Four BRPs consolidate data from each of the four PVIC branches and transfer the data to an array of PCs called Trigger Processors (TPs), where data of interest are selected for storage. One of the four BRPs acts as master and instructs the other BRPs to request a given time frame from the ROPs. The data is then transferred from the ROPs in parallel into the memory of the BRP. Once complete, the master BRP instructs the other three BRPs to transfer the time frame to a TP. The master BRP also keeps track of the number of time frames being queued and processed

in each TP and controls the operations of the TPs. The TPs time sort the hits from a received time frame and identify events of interest. An alert is sent to the far detector each time a spill occurs and all data is recorded during the spill and outside of the spill window. A trigger test is done on candidate events defined as time clusters of hits within a 200 ns window. The trigger requires that 4 out of 5 contiguous planes contain one or more hits. For the near detector, all data flagged to have occurred within a beam spill are recorded [45].

FIG. 2.7: The MINOS near detector at Fermilab, approximately 1km from the source of the neutrino beam.

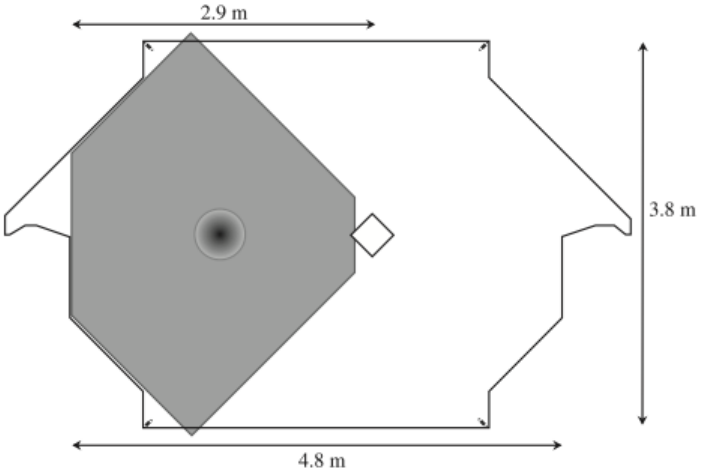

FIG. 2.8: The near detector planes. The coil hole is represented by the diamond shape in the middle. The circle represents the beam center. Partially instrumented planes cover the shaded region only.

FIG. 2.9: The MINOS far detector at the Soudan mine in Minnesota, approximately 735 km from the source of the neutrino beam.

CHAPTER 3

Calibration and Reconstruction

3.1 Calibration

The MINOS detectors are sampling calorimeters, meaning their light output is proportional to the energy deposition. Energy calibration is critical because the experiment relies on the comparisons of energy spectra and event characteristics in the near and far detector. Therefore, the calorimetric energy scale must be well known and ideally the same for both detectors. The calibration chain [41] is a multi-stage process that converts the raw pulse height $Q_{raw}(s, x, t, d)$ in strip s, longitudinal position along the strip x, time t, and detector d into a fully corrected signal Q_{corr} by applying several multiplicative calibration constants:

$$Q_{corr} = Q_{raw} \times D(d,t) \times L(d,s,Q_{raw}) \times S(d,s,t) \times A(d,s,x) \times M(d) \qquad (3.1)$$

where *D(d,t)* is a drift correction, *L(d,s,Q_{raw})* is a linearity correction, *S(d,s,t)* is a strip-to-strip correction, *A(d,s,x)* is an attenuation correction, and *M(d)* is an overall scale factor. Each is described below. Both an optical light injection (LI) system and cosmic ray muons

are used in the calibration. The LI system is used to measure the response of the readout electronics, including the PMTs, while cosmic ray muons are used to measure the response of the entire read out chain.

Gains and PMT Drift

A LI system periodically injects pulses of light from purple LEDs into the detector to be used for calibration [46]. Each pulse has a time reference associated with it when the LI system sends a signal to the front-end electronics. The TP designates all hits around this time reference within a well defined time window as a flasher event. Using spatial and temporal clustering of hits, the TP identifies events of physics interest. Periodically, the LI system pulses the fibers at each strip end to monitor the stability and gain of every channel. At the far detector, each strip end is pulsed 300 times per hour while at the near detector each strip end is pulsed 1000 times per hour. Each PMT pixel receives approximately 50 photoelectrons per pulse. Good environmental control eliminates most short-term variations in the electronics. However, in the long-term, variations of approximately less than 4% per year are seen, due to seasonal environmental changes and aging effects. Each month the data is collated and used to compute the average response per photoelectron per channel. The number of ADC counts per photoelectron for each channel is found by comparing the RMS width of many pulses to the mean. These gains are used offline for reconstruction tasks such as Monte Carlo simulations, crosstalk simulation, and strip efficiency evaluation [46].

Linearity calibration

At light levels of about 100 photoelectrons, the PMTs become $5-10\%$ nonlinear [42]. During calibration, the LI system is used to map this nonlinearity of the PMT response and to correct it. Once a month, each scintillator strip-end is pulsed 1000 times at many dif-

ferent light levels with the pulse height for each LED tuned so that the average response of the strips covers the full dynamic range of interest. This data is used to parametrize PMT response as a function of true illumination. Offline, the linearity correction is determined by interpolating PMT response [42].

Drift calibration

Temperature variations and aging cause light output changes in the scintillator and WLS fibers. In MINOS, a minimally ionizing particle is expected to deposit 2-10 photoelectrons at each end of a scintillator strip [41]. The drift calibration uses a sample of stopping muons at each detector to monitor the amount of energy deposited, which is expected to stay constant over time. Daily, the average pulse height per plane is computed and the relative change in this quantity is used to compute the drift according to:

$$D(d,t) = \frac{\text{Median response (d,}t_0\text{)}}{\text{Median response (d,t)}}. \tag{3.2}$$

Attenuation correction

Depending on where the particle hits along the fiber, light will be attenuated as it travels to the readout electronics. Hits that occur closer to the readout will have higher pulse heights than those occurring farther away along the strip. Instead of using cosmic ray muons to correct for the attenuation, it is more accurate to fit the data obtained from the module mapper measurements, which were conducted during detector assembly, to a double exponential according to Equation (3.3). In these measurements, a well-defined γ beam from a 5m Ci^{137}Cs source was used to illuminate the strip every 8cm. They provide a detailed map of the response of each scintillator module to ionizing radiation. The data are parameterized using:

$$A(x) = A_1 e^{-x/L_1} + A_2 e^{-x/L_2} \tag{3.3}$$

where x is the position along the strips, L_1 and L_2 are the two attenuation lengths, and A_1 and A_2 are the attenuation constants. A fit is performed for each strip and used to correct the data. Cosmic ray muons were used to double check this method. The pulse height from a hit by a track is plotted as a function of longitudinal track position and compared with the double exponential fit from the module mapper data. The difference is found to agree to approximately $\pm 4\%$. The cosmic ray muon method for obtaining attenuation constants is used in the near detector due to high cosmic ray statistics while the fits to the module mapper measurements are used in the far detector.

Strip-to-Strip non-uniformity calibration

The strip-to-strip calibration is used to remove variations in the individual strip response within the detector. The calibration, *S(s,d,t)*, is measured by using through-going cosmic ray muons. The data is linearized and known spatial and angular dependences are removed by applying attenuation and path-length corrections such that *S(s,d,t)* is calculated using the mean response of a muon of normal incidence traveling through the center of the strip. *S(s,d,t)* relates the mean response of each strip to the average detector response:

$$S(s,d,t) = \frac{\text{Mean response of detector (d,t)}}{\text{Mean response of the strip end (s,d,t)}} \tag{3.4}$$

This single correction incorporates several detector effects such as scintillator light yield, WLS collection efficiency, readout fiber attenuation, PMT quantum efficiency, and PMT gain.

Inter-detector calibration

A relative calibration is needed to normalize the energy scales at the near, far, and calibration detectors. Because of their abundance at all detectors and because their energy

depositions in each plane can be accurately determined from range measurements, stopping muons are used for this calibration. A so-called track window technique [47] is used. The *dE/dx* of a 1.5GeV/c muon increases by approximately 100% in the last 10% of its range. However, the *dE/dx* only changes by about 8% in the other 90% of the muon's range. The track window technique measures the response of muons when their momenta are between 0.5GeV and 1.1GeV. By only using muons from a region where the *dE/dx* varies slowly, a 2% error on knowing where the muon stopped corresponds to an error of approximately 0.2% in the energy deposition. This calorimetric response, *1/M(d)*, of the three detectors is calculated using this track window technique and used to normalize the detectors' energy scales to within 2%.

Absolute energy calibration

In order to achieve an accuracy of better than 10% on measurements of Δm^2_{23} and $\sin^2(2\theta_{23})$, MINOS has to have a less than 5% uncertainty in the absolute energy scale and less than 2% uncertainty in the relative calibration between the near and far detectors. A third MINOS calibration detector (CalDet) [48] was built to establish an energy scale for the two larger detectors and to develop the calibration technique. CalDet consists of five identical sub-sections, each with 12 steel, unmagnetized 1m $\times$ 1m planes. The front-end electronics and readout system used was identical to the MINOS far and near detectors and the DAQ was scaled down but otherwise identical to the MINOS DAQ system. CalDet's primary goal was to determine the calorimetric response to electrons, hadrons, and muons as a function of particle energy and to compare near and far detector response. To identify muons or pions, electrons, and protons, time-of-flight and Cherenkov detectors were used. Starting at 200 MeV/c and continuing in 200 MeV/c increments up to 3.6 GeV/c and then 1 GeV/C steps between 4 GeV/c and 10 GeV/c, CalDet was exposed to test beams of dual polarity at CERN to establish a response to hadrons, muons, and electrons. These

measurements were used to normalize Monte Carlo simulations and to get an uncertainty on the hadronic and electromagnetic energy scales. Data were compared to Monte Carlo simulations generated with GEANT3 [49]. Stopping muons were modeled to better than 3% while the simulated detector response to electrons agreed with data to 2% [50] .

Showers induced by pions and protons were compared with simulations using GHEISHA, GEANT-FLUKA, and GCALOR. The best agreement came from using GCALOR [51] simulations which was therefore adopted as the default shower code. The response to pion and proton induced showers agreed with data to better than 6% for all momentum settings [52]. The energy resolution may be parametrized at $56\%/\sqrt{E} \oplus 2\%$ for hadron showers and $21.4\%/\sqrt{E} \oplus 4\%$/E for electrons [41], where the energy E is in GeV.

Timing calibration

Timing information is used to determine the propagation direction of physics events. Up-going and down-going events must be clearly separated to maximize the sensitivity of the atmospheric neutrino analysis. An up-going event must originate from a neutrino interaction. However, there is a very high background of down-going cosmic muon events. In order to select up-going neutrino events from the high background of cosmic muons, the event direction must be reconstructed very precisely from timing information. Therefore, at the far detector, a timing calibration is performed. Due to different cable lengths and channel-to-channel variations in the electronics, the detector readout is synchronized only to within 30ns. A time offset is calculated between the actual times and positions of the reconstructed hits on each track and a linear timing fit. To obtain the final calibration constants, the offsets are tuned using an iterative procedure. Shifts in the timing system caused by changes in the readout components must be incorporated into the measured times. The size of these shifts can be calculated from the corresponding shifts in the relative times of muon hits recorded at opposite strip ends in the far detector. This calibration

is performed for each side at the far detector. A Gaussian fit to the distribution gives an RMS of 0.40 ns and the mean timing calibration error for a single strip is estimated to be $\sigma = 0.40\text{ns}/\sqrt{2} = 0.28$ ns [41].

Figure 3.1 shows the performance of the calibration chain on the far detector. Figure 3.2 shows an example of the calibration chain on the near detector.

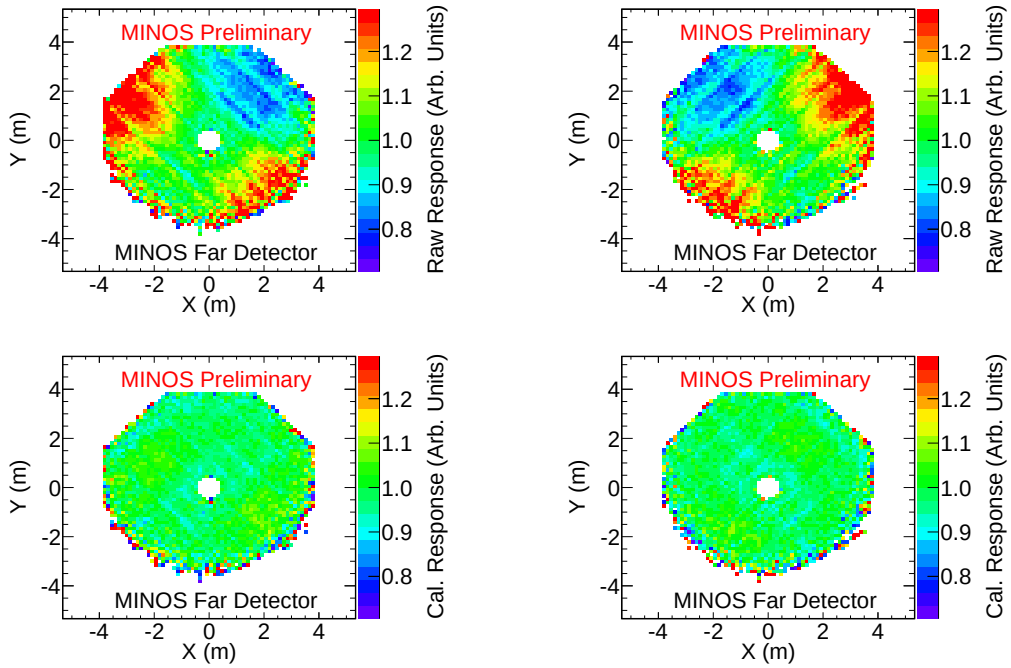

FIG. 3.1: The raw response (top) and the calibrated response (bottom) in ADCs for the far detector as a function of the detector position for the U strips (left) and the V strips (right) [53].

3.2 Event Reconstruction

Through an offline process called reconstruction, the raw data from the detectors is interpreted as neutrino interactions. During reconstruction, topology and timing of hits are used to identify neutrino interactions inside the detector as well as through-going muon tracks from cosmic rays or neutrino interactions in the surrounding rock. The

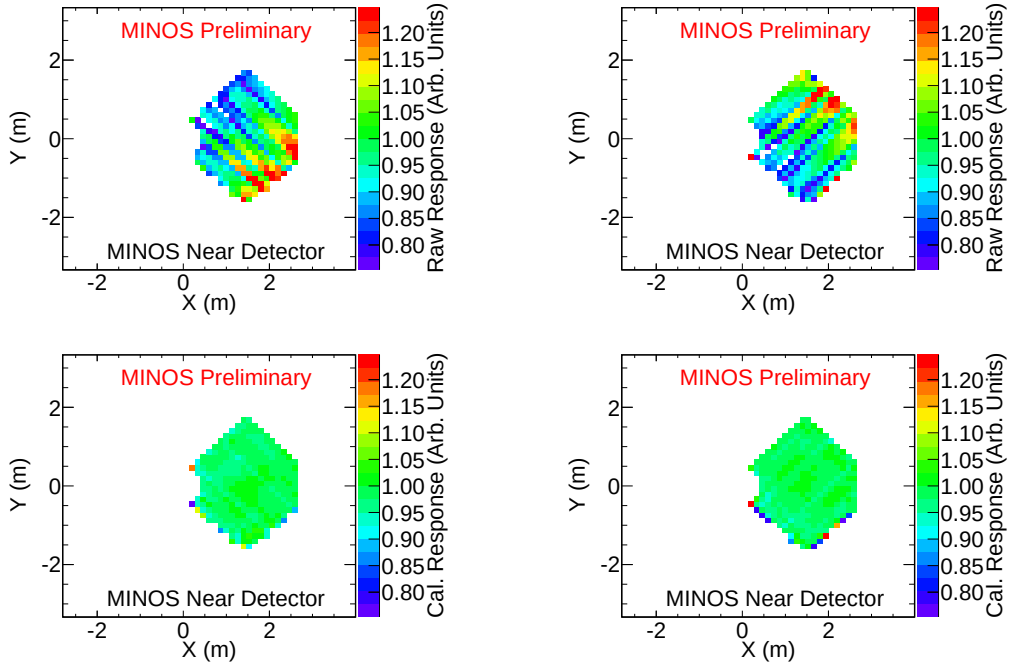

FIG. 3.2: The raw response (top) and the calibrated response (bottom) in ADCs for the near detector as a function of the detector position for the U strips (left) and the V strips (right) [53].

primary goal of reconstruction is to first provide characteristic quantities that can be used to identify what type of neutrino interaction occurred, then to estimate the visible energy of ν_μ charged-current, ν_e charged-current, and neutral current interactions. A long track, penetrating several detector planes is the strongest evidence for a ν_μ charged-current interaction. Neutral-current interactions can be characterized by the hadronic showers created by the recoil system while ν_e charged-current events are identified through the presence of an electron. Event topologies are further described in Section 4.1.

In the near detector, one or more neutrino interactions can occur in each beam spill. The data from one spill is called a snarl. The first step in the reconstruction procedure is to divide each snarl into one or more slices which contain hits that are localized in space and time. In the far detector, the rate is much lower and there is rarely more than one event per beam spill, in fact the vast majority of spills contain no neutrino interactions.

Next, the reconstruction algorithm uses a Hough Transform [54] to find track segments. These are then chained together into longer tracks, taking into account timing and spatial correlations. The momentum of the track is estimated in one of two ways. If the track stops within the detector, its momentum is calculated from its range using the range tables [55]. If the track exits the detector, its momentum is calculated from its curvature in the toroidal magnetic field. To calculate the momentum from curvature, the trajectory of the track is fitted using a Kalman Filter [56] technique. The Kalman Filter technique takes into account the bending of the track from both multiple Coulomb scattering and the magnetic field and the energy loss along the track. For a muon track produced by a ν_μ charged-current interaction, the momentum resolution is approximately 5% if determined by the range, and 10% if determined by curvature for the momentum calculation.

Showers are reconstructed from clusters of strips that are localized in space and time. The energy of the shower is computed by summing up the pulse height of all the individual hits. If a shower and a reconstructed track share the same hit, the tracks estimated pulse height is subtracted from the shower energy. For a neutrino induced hadronic shower, Monte Carlo simulations indicate that the energy resolution is 59% at 1 GeV.

3.3 Monte Carlo Event Simulation

Because MINOS is a two-detector experiment, it reduces the reliance on Monte Carlo simulations. However, it does not eliminate the need entirely and a reasonably accurate simulation is still necessary to perform parts of analysis, such as to estimate the background, correct for acceptance, estimate efficiency corrections, unfold detector resolution, fit oscillation hypotheses to data and to evaluate the effect of systematics. The simulation is performed in three stages: the beam simulation, the neutrino interaction simulation, and the detector simulation.

Beam Simulation

The NuMI beam is simulated using the FLUGG [57, 58] Monte Carlo generator to incorporate a GEANT4 [59] geometry into a FLUKA [60] simulation of the hadronic production, decay and transport process. Primarily, it is a simulation of the secondary meson beam and its decay to produce neutrinos. The simulation begins with the 120 GeV Main Injector protons incident on a graphite target. It then follows any secondary mesons that are produced as they travel through the focusing horns and into the decay pipe. The properties of the parent particle are recorded once it decays to produce a neutrino. Using the position and momentum of the parent particle, the probability of that neutrino reaching one of the detectors and its energy is then calculated. Every pion decay to neutrino is recorded along with a weight that accounts for the probability of the neutrino actually getting to the detectors. The weighted neutrino flux is the input to the MINOS detector simulation.

Neutrino Interaction Simulation

NEUGEN [61] is used to generate neutrino interactions. The program simulates both quasi-elastic and inelastic neutrino scattering in a range of 100MeV to 100GeV. The hadronization process is simulated using the AGKY [62] model. At high hadronic invariant mass PYTHIA/JETSET [63] is used while at low invariant mass the KNO [64] phenomenological model is used with a smooth transition between the two models. The INTRANUKE [65] model of intranuclear rescattering is also included in NEUGEN to account for the interactions of the hadronic particles as they leave the nucleus. The model incorporates pion elastic and inelastic scattering, single charge exchange, and absorption.

Detector Simulation

The MINOS detector simulation, GMINOS, is based on GEANT3 [49]. It is used to generate raw energy depositions that are used as input to the detector response model. Randomly selected neutrino events from the flux predicted by the beam simulation are traced through to the near and far detector and the strip-by-strip energy depositions as the particles lose energy in the steel and scintillator are recorded. GMINOS includes a model for the magnetic fields derived from a finite-element analysis incorporating bench measurements of the steel B-H curve.

Based on the GMINOS energy depositions, a C++ based PhotonTransport program, generates photons in the scintillator, transports those photons into the WLS fiber and onto the PMT cathode where they are converted into photoelectrons using a Poisson number generator. PhotonTransport includes detailed behavior of the PMTs and electronics, including non-linearity, noise, cross-talk, and triggering. The simulation is decalibrated by applying the measured calibration constants in reverse in order to model the real-world detector as accurately as possible. This way the simulation includes the best knowledge available on the light levels, attenuation, non-linearity, and gains. A fictitious date from actual data taking is given to each simulated run and the calibration constants from that time are used on the Monte Carlo. Later, each Monte Carlo run is re-calibrated by reapplying the calibration constants from the same date that were used to produce it. At this point, the Monte Carlo is as similar to real data as possible and both are handled in the same manner during reconstruction.

CHAPTER 4

Event Identification

4.1 Types of Events in MINOS

Neutrinos interact with matter through only the weak interaction. There are two types of weak interactions. A charged current (CC) interaction results through the exchange of a charged $W^{\pm}$ boson, as shown in Figure 4.1. The incoming neutrino interacts with a nucleus resulting in a lepton corresponding to the initial neutrino flavor. Charged current interactions have an energy threshold due to the lepton being produced in the final stage. Therefore, ν_τ charged current events are rare given MINOS's energy range. A neutral current (NC) interaction occurs from the exchange of a neutral Z boson, as shown in Figure 4.2. The neutrino exits the interaction leaving no information about the original neutrino flavor and taking away some of the initial energy of the neutrino. The cross sections are the same for all three active flavors and therefore a deficit in the NC spectrum at the far detector would indicate the existence of a sterile neutrino. This chapter explains the different types of events observed in the MINOS detectors and explains the criteria for selecting CC and NC events.

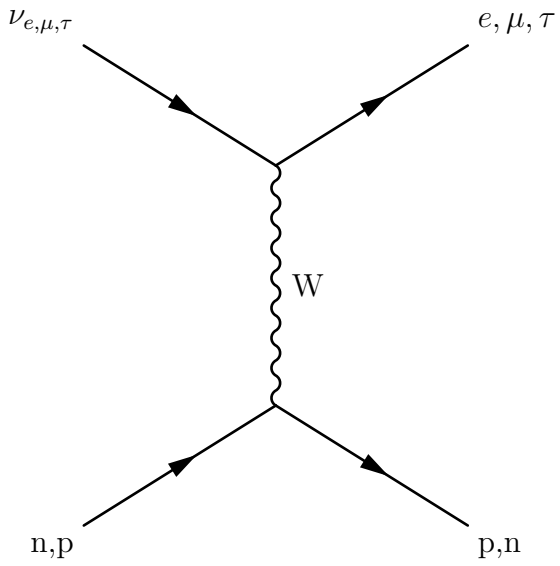

FIG. 4.1: Feynman diagram for a neutrino charged-current interaction. Where time goes from left to right.

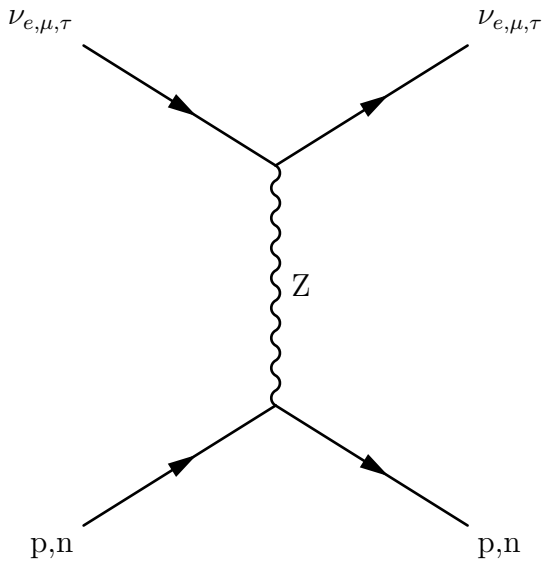

FIG. 4.2: Feynman diagram for a neutrino neutral-current interaction. Where time goes from left to right.

4.1.1 ν_μ CC events

An incoming muon neutrino will interact with the detector through the exchange of a $W^\pm$ boson resulting in a muon track and a hadronic shower. Figure 4.4 shows a ν_μ CC event from the Monte Carlo simulation. Due to the magnetized coil, the muon will produce a long track that will curve toward or away from the coil in the magnetic field allowing for charge identification and momentum estimation. As muons traverse the detectors, they lose energy primarily due to ionization when they interact with the scintillator and steel. For energies between 10MeV and 10GeV, the mean energy loss is well described by the Bethe-Bloch equation (4.1) [66].

$$\left\langle -\frac{dE}{dx} \right\rangle = Kz^2 \frac{Z}{A} \frac{1}{\beta^2} \left[\tfrac{1}{2} \ln \tfrac{2m_e c^2 \beta^2 \gamma^2 W_{max}}{I^2} - \beta^2 - \tfrac{\delta(\beta\gamma)}{2} \right] \tag{4.1}$$

where $K = 4\pi N_A r_e^2 m_e c^2 = 0.307$ MeVg^{-1}cm^2, A is the atomic mass of absorber, Z is the atomic number of the absorber, W is the maximum energy transfer to an electron in a

single collision, I is the mean excitation energy, $\delta(\beta\gamma)$ is the density effect correction to the ionization energy loss, z is the charge number of the incident particle, and m_e is the mass of the electron. According to the Bethe-Bloch equation, a muon with momentum

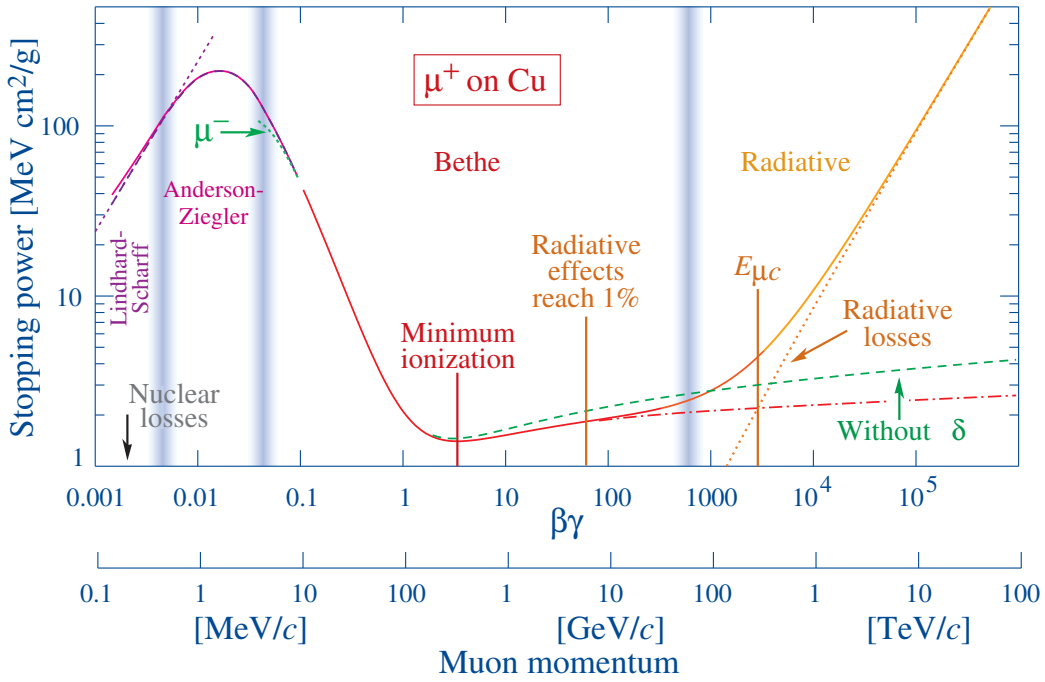

FIG. 4.3: Energy loss of muons in copper as a function of $\beta\gamma$ over several orders of magnitude. Vertical bands separate boundaries for different approximations [66].

within a certain range based on the material will lose a minimum of about 1.5 - 2.0 MeV cm^2/g while traveling through matter. The energy is computed for a stopped muon track by going backwards along the track and adding the energy that would have been lost in each steel and scintillator plane.

4.1.2 ν_e CC events

The incoming electron neutrino will interact with the detector through the exchange of a $W^{\pm}$ boson resulting in an electron and a hadronic shower. Through bremsstrahlung, the electron will create an electromagnetic shower. Figure 4.4 shows a ν_e CC event in Monte

Carlo. These types of events are produced in the far detector from ν_e contamination in the NuMI beam and from $\nu_\mu \rightarrow \nu_e$ oscillations.

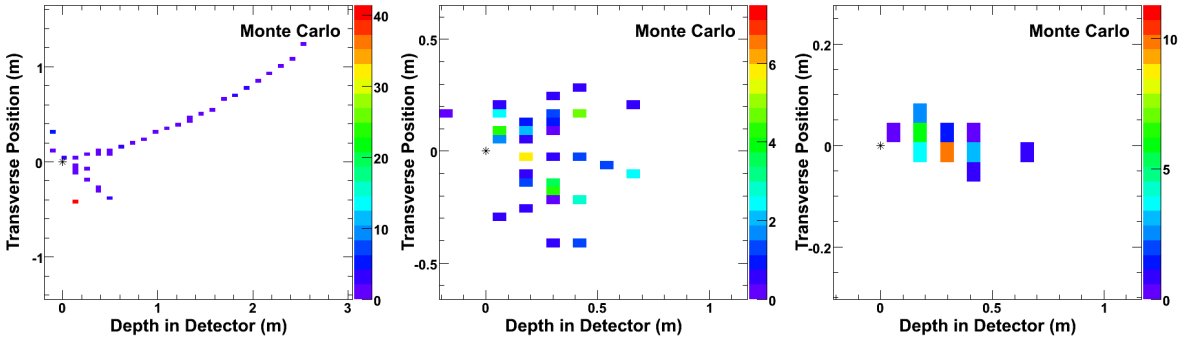

FIG. 4.4: Monte Carlo simulations of the different event topologies, ν_μ CC (left), NC (center), and ν_e CC (right), visible in the MINOS detectors [67].

4.1.3 NC events

An incoming neutrino may also interact with the detector through the exchange of a neutral Z boson resulting in a hadronic shower and a neutrino in the final state. Because the neutrino is in the final state, it carries away a fraction of the energy of the interaction which cannot be reconstructed and the flavor of the incoming neutrino remains unknown. Figure 4.4 shows a NC event as seen in Monte Carlo simulations.

4.2 NC Event Classification

In order to reject non-neutrino events, such as cosmic ray muons, all events must have their reconstructed vertex safely within a fiducial volume inside the detector and their timing has to be within a beam spill window. The fiducial volume requirement also removes events near the edges of the detector that will have an unknown fraction of their energy deposited outside of the detector. Such events will have poor energy reconstruction and are thus removed with the fiducial volume requirement. In the NC analysis, the event

vertex is used unless a track extends farther than the shower. In such cases, the event vertex is defined to be the track vertex. For the near detector, the vertex of the event must be 0.5m or more from the edge of the outline defined by the scintillator in the partially instrumented plane. Also, the longitudinal position of the vertex, z, must be 1.7 m $< z <$ 4.737m. The lower limit of the cut rejects muon events from neutrino interactions in the rock in front of the detector and the upper limit is about 2.4m from the back of the calorimeter. This ensures good containment of hadronic showers. For the far detector, events must be 0.4m or more from the outer edge of the detector and 0.6m or more from the center of the coil hole. The longitudinal position of the vertex must be within one of the super-modules of the far detector and not in the gap between them, 0.21m $\leq z \leq$ 13.72m or 16.12m $\leq z \leq$ 28.96m [68].

The quality of data is tested by counting the number of crates that were enabled when the event was recorded. Events in both detectors must pass a beam type cut to ensure that data is from the low energy beam and that the horn is on. The status of the coil is recorded with each event and a quality cut is enforced.

4.2.1 Near detector specific preselection

The ND neutral current spectrum is contaminated with poorly reconstructed events that are reconstructed as low energy showers. Because of the higher neutrino flux at the near detector, the badly reconstructed events are unique to the near detector due to events overlapping in space and time and cause Far-Near differences between the detectors. Large data and Monte Carlo discrepancies, due to the presence of these badly reconstructed events, are reduced by the implementation of two pre-selection cuts. Poorly reconstructed events are expected to often have few consecutive planes with deposited energy above a given threshold (2 photoelectrons for this analysis). Therefore, events are cut if the

maximum number of consecutive planes is < 3. Figure 4.5 shows the data and Monte Carlo comparison of the distribution of the number of consecutive planes in an event.

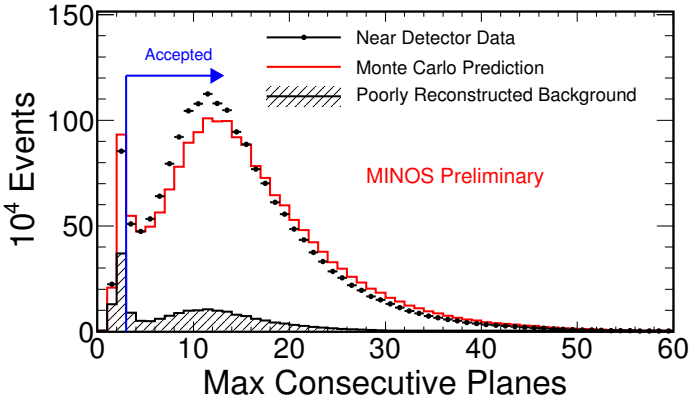

FIG. 4.5: Monte Carlo and data distribution of the number of consecutive planes with signal in an event in the near-detector. Distrubution is for all events in the near detector. Events with fewer than 3 consecutive planes are removed from the sample.

The second preselection cut is defined to be the event pulse height divided by the total pulse height deposited in the slice. Events are cut if the ratio is ≤ 0.5 [69]. Figure 4.6 shows the data and Monte Carlo comparison of the slice pulse height fraction

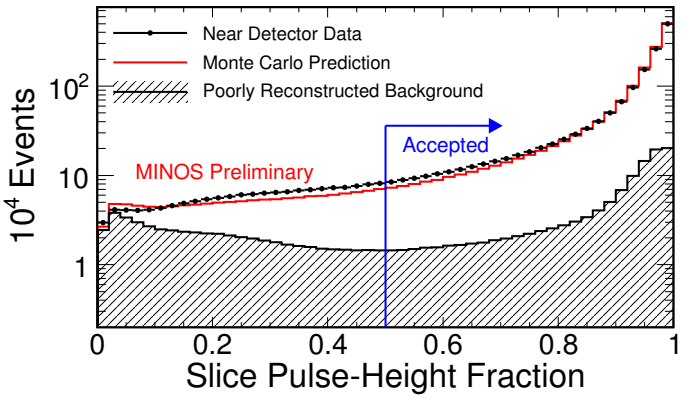

FIG. 4.6: Monte Carlo and data distribution of the fraction of the slice pulse height contained in the event. Distrubution is for all events in the near detector. Events with a slice pulse height of less than 0.5 are removed from the sample.

4.2.2 Far detector specific preselection

Background events are different in the far detector and therefore a separate set of pre-selection cuts is applied. These pre-selection cuts remove events due to detector noise, cosmic ray induced events, and stray light injection (LI) pulses.

The LI system pulses the ends of the wavelength shifting fibers continuously monitor the PMT gain and optical path integrity. A trigger PMT (tPMT) is attached to the LI system to provide a signal when the LI is flashing. This allows the spills to be rejected in later processing. However, if the tPMT does not trigger, the neutrino sample will get contaminated with these LI events. A series of cuts allows these events to be rejected from the final sample. A signal event will often occur in the center of the detector leading to a balanced east-west energy deposition. However, the light injection is on one side of the strip which leads to an east-west energy deposition asymmetry. Also, the energy deposition of a LI event is often much larger than the average minimum ionizing particle. An event will be classified as LI and removed from the analysis if both of the following conditions are met,

1. The sum of the pulse height in the east and west portions of the detector is greater than 1.7×10^6 ADC or the east-west asymmetry exceeds 0.55.

2. The pulser box which contains the greatest number of strips hit has $> 2\%$ of the strip hits and the ratio of the strip hit fraction in the second pulser box to that of the first pulser box is $< 0.6\%$.

Another potential background signal in the far detector is fiber noise events. Fiber noise may occur from the electronics or PMTs or from spontaneous light emission from the scintillator and wavelength-shifting fiber [41]. Typically, the ADCs from a noise event are much smaller than the typical minimal ionizing particle (MIP) energy deposition of a

signal event. An event is classified as fiber noise and removed from the sample if either of the following two conditions are met:

1. Number of hit strips ≤ 8 and the pulse height < 3750 sigcor
2. Number of hit strips > 8 and the pulse height < 2000 sigcor

Contamination from cosmic ray muons is a sub-dominant background source. Cosmic ray muons may be very steep and therefore reconstructed as a shower, or else a track may be reconstructed. An event is classified as a cosmic ray muon and removed from the sample if,

1. The longitudinal direction cosine, $\frac{|p_z|}{E}$, is < 0.4.
2. If a shower is reconstructed in the event, the RMS value of the shower strip positions is > 0.5.
3. The event steepness, defined as $\left(\frac{strips}{plane}\right)/$ (event planes), is ≥ 1.

Spill times are also checked at the far detector. Events are required to be between -2 μs and 12 μs of the beginning of a beam spill. An in depth description of the far detector preselection cuts can be found in [70] and [71].

4.2.3 Neutral-current Event Selection

After the preselection cuts are applied, a selection criteria is applied to distinguish neutral current events from charged current events. The same selection variables are applied to both the near detector and the far detector. Because neutral current events are usually shorter than charged current events, a constraint is placed on the length of the event. If the event has no reconstructed track and passes fewer than 47 planes in the detector, it is classified as a neutral current event. If there is a reconstructed track present

in the event, the track must extend no more than 5 planes beyond the shower and the event must cross fewer than 47 planes. Events that fail the neutral current selection are classified as charged current events if they pass the charged current selection described in the next section [72].

Figure 4.13 shows the distribution of the event vertices for neutral-current selected events within the far-detector fiducial volume. The efficiency and purity of the neutral current selection based on Monte Carlo simulations for both the near and far detectors is shown in Figure 4.14.

4.3 Charged current Event Classification

Previous sterile analyses have used the same preselection cuts as the NC events with an additional PID cut applied and only selected negatively charged tracks. For this analysis, the charged current selection criteria from the 2012 ν_μ disappearance analysis [73], as described in Section 4.3.3 was adopted and both positive and negative tracks are included in the analysis. The charged current selection is only applied to events that have failed the neutral current selection. Events that fail both selectors are discarded from the analysis.

There are several cleaning cuts that are applied to both the near detector and the far detector. We make sure that the beam hit the target well and that the configuration of the beam is consistent with the particular run. The coil is tested to make sure it is operational and the coil current is in the proper direction, i.e. that the magnetic field focuses negative muons for FHC running and positive muons for RHC running. LI events are rejected. Events where the error on the muon tracks reconstructed charge over the momentum ratio, $\sigma(\frac{q}{p})$, equals 1 $\times 10^{-4}$ are removed from the sample. This is an error which indicated a failure in the Kalman filter during track reconstruction.

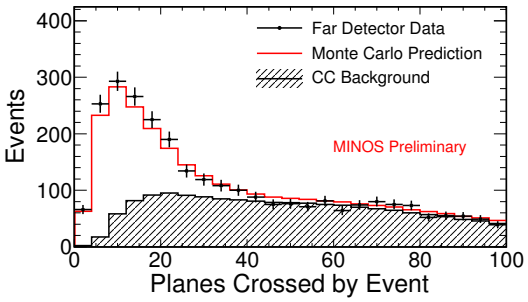

FIG. 4.7: Monte Carlo and data comparison of the event lengths in the far detector for neutral current events.

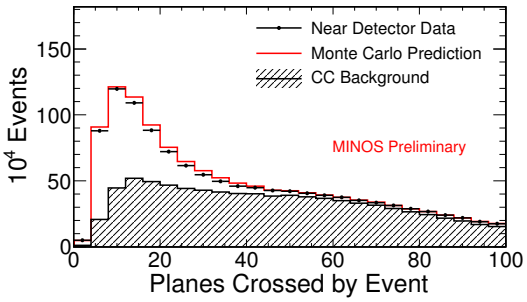

FIG. 4.8: Monte Carlo and data comparison of the event lengths in the near detector for neutral current events.

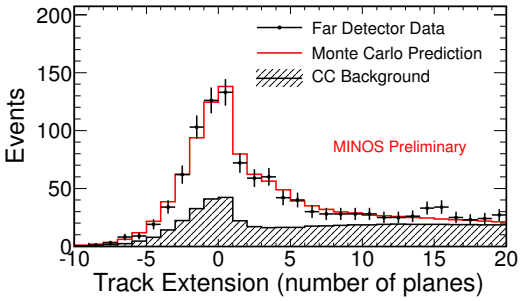

FIG. 4.9: Monte Carlo and data comparison of the track extension in the far detector for neutral current events.

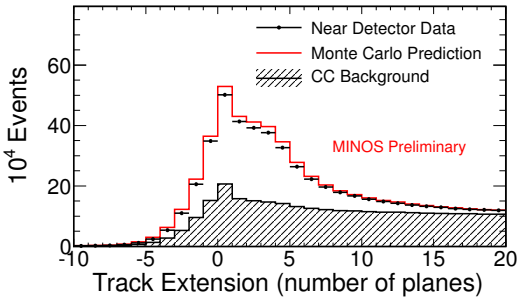

FIG. 4.10: Monte Carlo and data comparison of the track extension in the near detector for neutral current events.

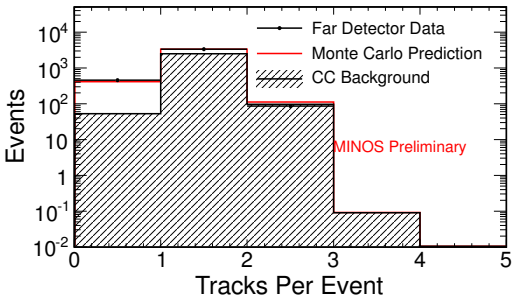

FIG. 4.11: Monte Carlo and data comparison of the number of tracks in an event in the far detector for neutral current events.

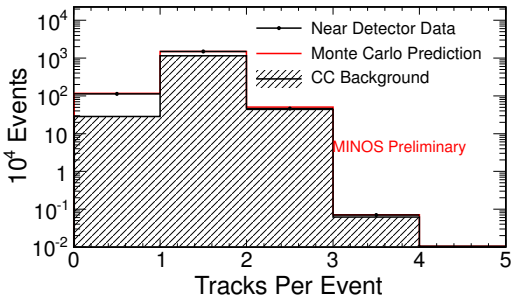

FIG. 4.12: Monte Carlo and data comparison of the number of tracks in an event in the near detector for neutral current events.

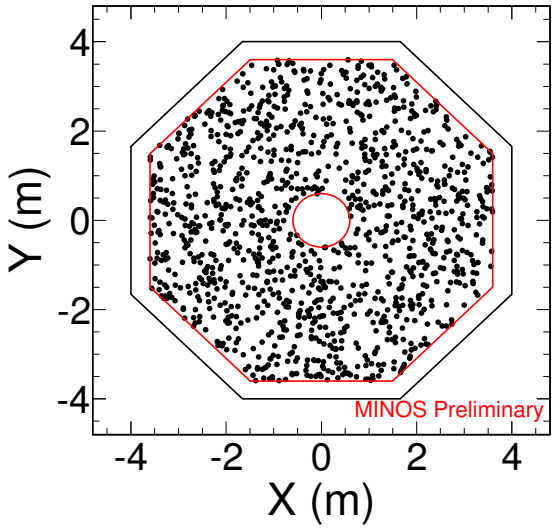

FIG. 4.13: All event vertices observed in the far detector for neutral-current selected events. The red lines indicates the fiducial volume cut.

4.3.1 Near detector specific cuts

Events are removed which are too close to the coil hole. These events are typically poorly reconstructed due to the large curvature in the muon tracks and the large amount of uninstrumented material near the coil. The selection removes events whose track ends at the far side of the coil (x $<$ 0), where x is the horizontally oriented direction and 0 is the center of the coil hole, or the track ends within 60cm of the center of the coil hole. Because the Kalman fitter often fails on events that it cannot reconstruct, prior to this selection criteria, the track fitter pass rate was 95%. With the addition of this cut the pass rate is 99%.

4.3.2 Far detector specific cuts

A timing cut is applied at the far detector to remove non-NuMI beam events. Events must be within a -2 to 12μs spill window to be kept. To further reduce cosmic and atmospheric background, a cut on the track direction is applied. It is required that cos(θ) $>$

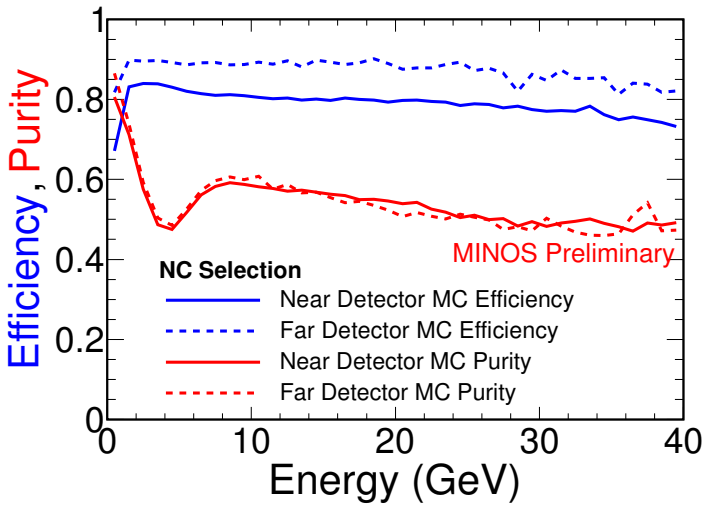

FIG. 4.14: The efficienty and purity of the neutral current event selection is shown for both the far and near detectors. The dip in the prurity at 2-3 GeV can be explained by the charged current background peaking in this region.

0.6, where θ is the angle between the muon track and the beamline. If there are more than two events overlapping in a spill window, that entire event is removed from the sample. If there are two overlapping events then only the largest event, defined as having more than 75% of the total pulse height, is used. Figure 4.15 shows the distribution of the event vertices for charged-current selected events within the far-detector fiducial volume.

4.3.3 k-Nearest-Neighbor method of charged current identification

Neutral current and charged current events are separated using the k-nearest-neighbor (kNN) method. There are a number of variables associated with a true charged current event. The kNN method uses these variables to distinguish actual charged current events by comparing data events to a Monte Carlo training sample which is divided into two sets of events, one set which includes a muon track and another that does not [74]. A Euclidean

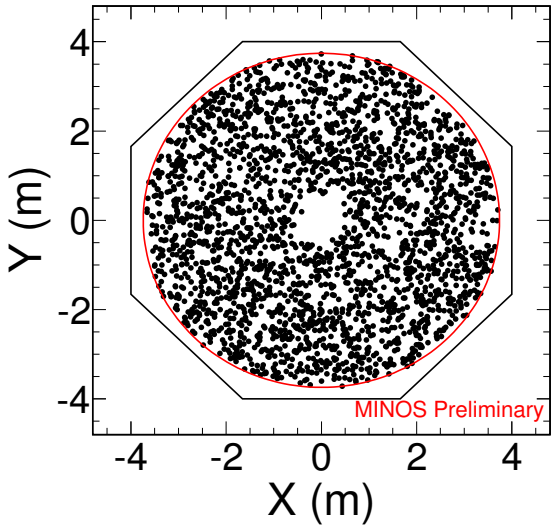

FIG. 4.15: All event vertices observed in the far detector for charged-current selected events. The red lines indicates the fiducial volume cut.

space is defined by

$$\mathrm{D}^2 = \sum_{i}^{d} (\mathrm{X}_i^T \mathrm{X}_i^Q) \tag{4.2}$$

where D is the distance, d is the number of variables, X_i^T is an event from the Monte Carlo training set, and X_i^Q is a data event. The k-nearest-neighbours, where k is defined to be 80, are then selected and a probability that the event is a charge-current event is calculated according to

$$\mu_{\mathrm{ID}} = \frac{\mathrm{k}_\mu}{\mathrm{k}} \tag{4.3}$$

where k_μ is the number of selected neighbouring events which contain a muon track and k is the number of events selected. MINOS utilizes two methods for calculation of μ_{ID}. These are roID which is applied at all energies and the jmID which is instead applied between 0-5 GeV to data from a forward horn current (FHC) run.

The roID [74] calculation uses the following four discriminating variables:

1. The number of active planes in the track, since muons tend to travel much further than NC events.

2. The transverse profile, since muon tracks tend to deposit only a single hit on a given scintillator plane and are therefore cleaner events than a shower.

3. The average pulse height per plane in the track, since muon tracks are minimally ionizing while hadronic showers tend to deposit more energy.

4. The ratio of mean low pulse height to mean high pulse height, because muon tracks tend to deposit energy in a consistent manner relative to a hadronic shower.

The distribution of the roID variable, μ_{ID}, in the near detector is shown in Figure 4.16. A charge current event is selected if $\mu_{\mathrm{ID}} > 0.25$.

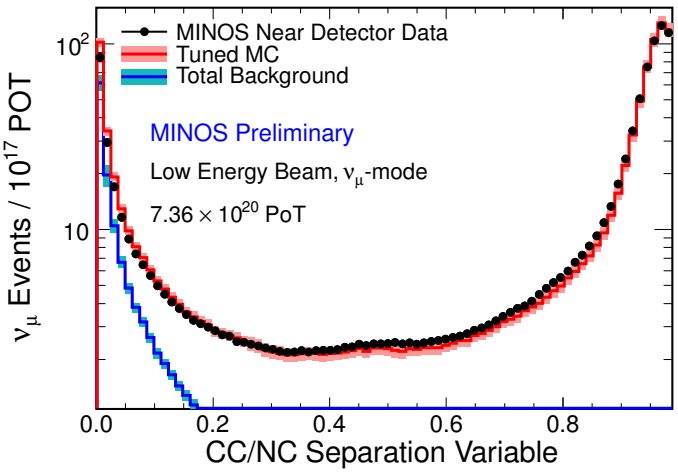

FIG. 4.16: The roID distribution in the near detector. Events that fail the neutral current selection and have $\mu_{\mathrm{ID}} > 0.25$ are classified as charged current events [74].

The jmID [75] calculation is used for events with energies of 0-3GeV obtained in the FHC runs. At lower energies it is harder to distinguish short tracks and neutral current showers, due to the detector's resolution. The jmID attempts to keep the efficiency of the

sample as high as possible. It used the following three discriminating variables which are meant to identify shorter tracks better:

1. As with the roID, the number of active planes in the track is considered.

2. The pulse height in the last five planes of the track will be lower than in a hadronic shower because hadronic particles tend to end with a large energy deposit due to nuclear interaction.

3. The degree of scattering will be smaller in a muon track because they tend to have gently curving paths, whereas hadronic tracks will have more hadronic scattering and plane-to-plane variations.

A charged current event is selected if $\mu_{\mathrm{ID}} > 0.5$.

The efficiency and purity of the charged current selection for both the near and far detectors is shown in Figure 4.17.

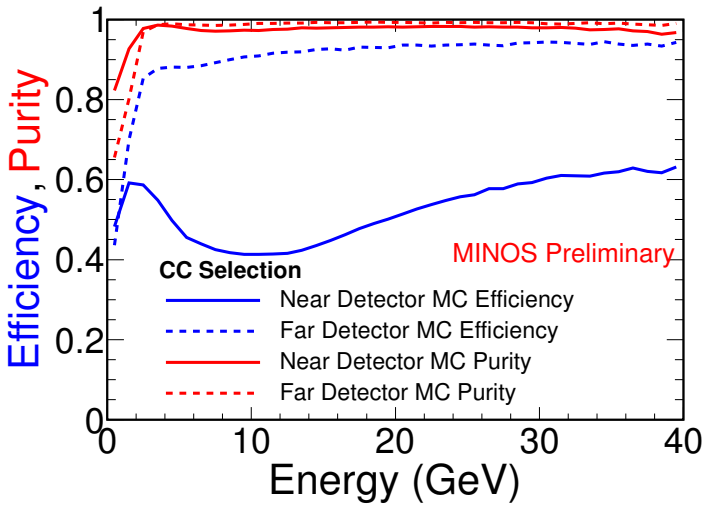

FIG. 4.17: The efficiency and purity of the charged current event selection is shown for both the far and near detectors as determined through Monte Carlo simulations. The large change of the efficiency in the near detector is due to the removal of events which include tracks ending near the coil.

CHAPTER 5

Analysis

If a fourth, sterile, neutrino should exist, as suggested by the LSND experiment [28], a deficit in the neutral current spectrum would be observed in the far detector because the sterile neutrino would not interact in the detector volume. A method for searching for such a deficit in the far detector neutral current spectrum is presented here. If the sterile neutrino should have a large mass-squared difference, $\Delta m^2_{34} \sim 1\ \mathrm{eV}^2$ (where $\Delta m^2_{34} = m^2_4 - m^2_3$), the charged current energy spectrum would also be distorted at higher energies. The charged current spectrum is also used to constrain Δm^2_{23}. This analysis, therefore, uses both the neutral current and the charged current spectra to probe for sterile neutrino mixing. A far-over-near ratio from Monte Carlo is used to generate a far detector energy spectrum prediction based on near detector data for both neutral current and charged current events. The far detector prediction is then compared with far detector data by fitting for the oscillation parameters that will minimize the χ^2 between data and Monte Carlo. At large values of Δm^2_{41} ($1\,\mathrm{eV}^2$), oscillations into sterile neutrinos will occur before reaching the near detector. This thesis aims to build upon the MINOS 2011 sterile neutrino

publication [1] with the addition of new data and the inclusion of possible near detector oscillations into the far detector prediction.

5.1 MINOS 2011 Sterile Neutrino Search

In 2011, the MINOS collaboration reported a result which was consistent with the standard three flavor neutrino oscillations model [1]. The far detector energy spectrum is predicted by calculating the ratio of events in the far and near detectors as a function of reconstructed energy using Monte Carlo and multiplying that ratio by the near detector data spectrum. This method is discussed in further detail in subsequent sections. The far-over-near ratio predicted that 754 $\pm$ 28(stat) $\pm$ 37(syst) NCevents would be observed in the far detector based on three flavor oscillations. A total number of 802 neutral current candidates were observed, which is consistent with the three flavor neutrino oscillation model. Figures 5.2 and 5.3 show the observed neutral current and charged current energy spectra, respectively. For the $m_4 \gg m_3$ model, the analysis also obtained 90% C.L. limits of $\theta_{24} < 7°(8°)$ and $\theta_{34} < 26°(37°)$, for $\theta_{13} = 0°(11.5°)$.

This thesis furthers that analysis with the addition of data from Runs V, VI, and X, for a total of 10.56×10^{20} POT and takes into account the possibility that oscillations into sterile neutrinos could occur prior to reaching the near detector. Figure 5.1 depicts the total accumulated data for MINOS between 2005 and 2012.

5.2 Far-over-Near Ratio

A far detector prediction is obtained for both neutral current and charged current selected energy spectra through the extrapolation of near detector data. The near detector data provides a high statistics neutrino interaction sample that reduces the dependance

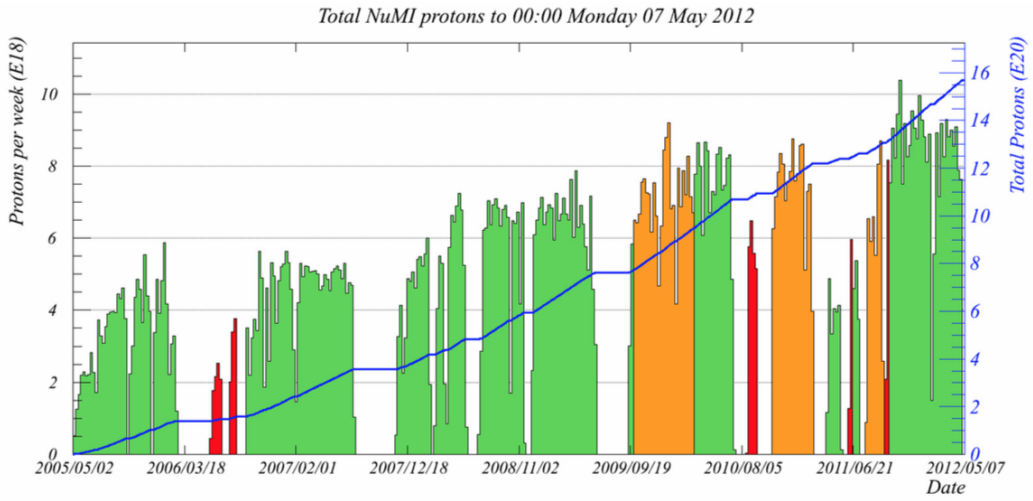

FIG. 5.1: MINOS complete data set between 2005 and 2012. A total of 15.6 $\times 10^{20}$ POTs were accumulated. The low energy forward horn current (FHC) neutrino mode is shown in green. The anti-neutrino mode using reversed horn current (RHC) is shown in orange. The red depicts some higher energy modes with different target positions [76].

on Monte Carlo simulations in the far detector prediction. A far-over-near ratio will be used in the extrapolation which applies a correction to each reconstructed energy bin in the far detector Monte Carlo using the near detector data and Monte Carlo differences as a scale factor according to

$$FD^{\text{prediction}} = ND^{\text{data}}\left(\frac{FD^{\text{oscillated MC}}}{ND^{\text{oscillated MC}}}\right), \tag{5.1}$$

where ND^{data} is the number of selected events in the near detector data, $ND^{\text{oscillated MC}}$ is the number of events expected from near detector Monte Carlo scaled by the neutrino oscillation probability as a function of the variable oscillation parameters, and $FD^{\text{oscillated MC}}$ is the number of events expected from the far detector Monte Carlo scaled by the neutrino oscillation probability.

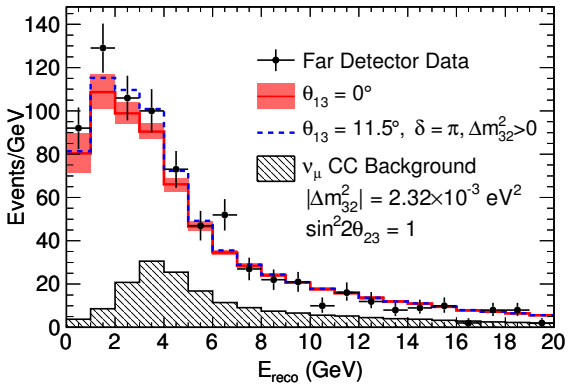

FIG. 5.2: Far detector neutral current spectrum from the MINOS 2011 sterile neutrino search result from an exposure of 7.07×10^{20} protons on target [1]. A total of 802 neutral current candidates were observed while $754 \pm 28(\text{stat}) \pm 37(\text{syst})$ events were expected for standard three flavor oscillations. The result was consistent with the standard three flavor neutrino oscillation model.

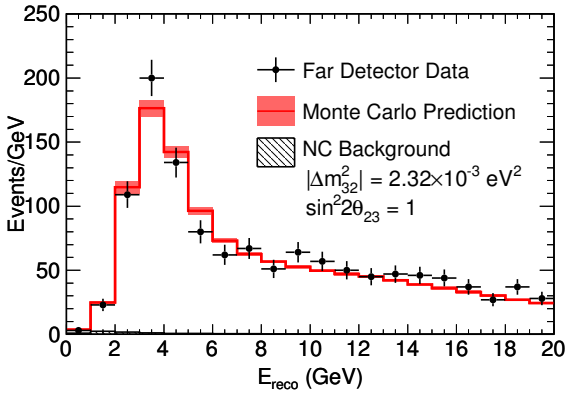

FIG. 5.3: Far detector charged current spectrum from the MINOS 2011 sterile neutrino search result from an exposure of 7.07×10^{20} protons on target [1].

5.2.1 Oscillation Probability

The oscillation probability implemented in this analysis is the exact 3+1 sterile neutrino mixing model which includes an additional sterile flavor eigenstate, ν_s, and one additional mass eigenstate, m_4, as explained in Chapter 1 and shown again:

$$P(\nu_\alpha \to \nu_\beta) = | \ \delta_{\alpha\beta} - 2iU^*_{\alpha 2}U_{\beta 2}\sin(\Delta_{21})e^{-i\Delta_{21}} - 2iU^*_{\alpha 3}U_{\beta 3}\sin(\Delta_{31})e^{-i\Delta_{31}} \\ - 2iU^*_{\alpha 4}U_{\beta 4}\sin(\Delta_{41})e^{-i\Delta_{41}} \ |^2 \tag{5.2}$$

Matter effects are not included in the 3+1 oscillation model used for this analysis. The exact 3+1 model correctly incorporates oscillations at the near detector. The procedure to oscillate the far and near detector Monte Carlo is explained in the following section. Both a neutral current and charged current far detector prediction is extrapolated and compared to far detector data separately through χ^2 minimization.

5.2.2 Oscillated Monte Carlo

In order to oscillate the Monte Carlo properly, the Monte Carlo is divided into five types of true events for both the near and far detectors: neutral current events, charged current ν_μ events, charged current beam ν_e events, charged current $\nu_\mu \rightarrow \nu_e$ events, and charged current $\nu_\mu \rightarrow \nu_\tau$ events which are obtained from the following three samples of Monte Carlo:

1. A nominal Monte Carlo sample with no oscillations applied to the events. There are three types of events in this sample: neutral current events from both ν_μ and ν_e, charged current ν_μ, and charged current ν_e's from the intrinsic ν_e component of the beam. No ν_τ's are simulated in the beam.

2. A fully oscillated Monte Carlo sample where all ν_μ events are converted to ν_τ events.

3. A fully oscillated Monte Carlo sample where all ν_μ events are converted to ν_e events.

Applying an oscillation weight for each event in the Monte Carlo sample would be very CPU intensive when attempting a χ^2 fit for each unique combination of oscillation parameters. Instead, for each type of event, a 2D histogram is constructed for the reconstructed neutrino energy versus the ratio of the baseline over the unoscillated true neutrino energy (L/E), as in Figure 5.4. The baseline is defined here as the distance between the neutrino production

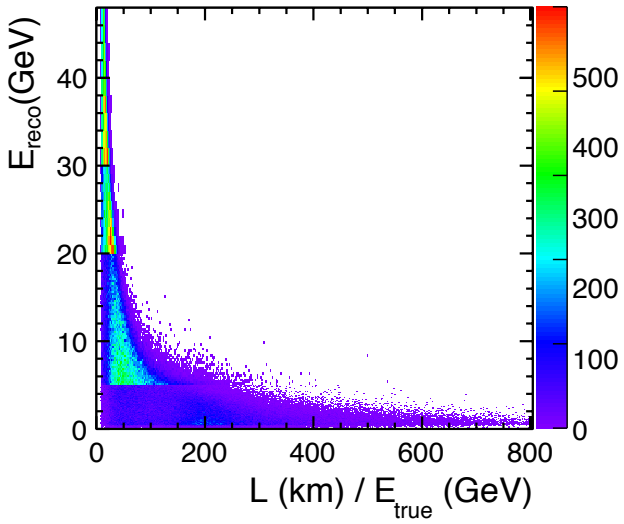

FIG. 5.4: Reconstructed energy vs. L(km)/E_{true}(GeV) 2D histogram for simulated true neutral current events selected in the far detector.

vertex and the far or near detector. For each bin of L/E, each reconstructed energy is scaled by the oscillation probability according to event type:

1. True neutral current events: 1 - P($\nu_\mu \rightarrow \nu_s$)

2. Charged current ν_μ events: P($\nu_\mu \rightarrow \nu_\mu$)

3. Charged current beam ν_e events: P($\nu_e \rightarrow \nu_e$)

4. Charged current $\nu_\mu \rightarrow \nu_e$ events: P($\nu_\mu \rightarrow \nu_e$)

5. Charged current $\nu_\mu \rightarrow \nu_\tau$ events: P($\nu_\mu \rightarrow \nu_\tau$)

where P($\nu_\alpha \rightarrow \nu_\beta$) is given by equation 5.2. Once the oscillation weight has been applied, the reconstructed energy is recorded for each type of event in a separate 1D histogram and all five are added for a final oscillated Monte Carlo reconstructed energy spectrum. The above procedure is repeated for both the near and far detectors and for the neutral current and charged current spectra separately.

Validation

As stated previously, the most accurate manner to apply oscillations would be on an event by event basis. However, the Monte Carlo sample will have many neutrinos with the same reconstructed energy and L/E combination. Hence, when performing the χ^2 fitting procedure, nearly the same probability would be calculated millions of times, making it very inefficient and time consuming. The binned method described above for oscillating the Monte Carlo is a reasonable approximation. To validate the method, a fake data set was generated for the far detector using Monte Carlo and applying selected oscillation parameters on an event by event basis. The oscillation parameters used to generate the fake data set were the best fit parameters for standard three flavor oscillations known at the time. This fake far detector data set was then compared to the far-over-near ratio method for generating a far detector prediction using the 2D-histogram oscillation approximation. When performing this validation method on the neutral current events, the fake data set and the far detector prediction lined up to within a few subpercent, as shown in Figure 5.5. However, initially when performing this validation on the charged current events, a large discrepancy was discovered between the fake data set and the far detector prediction, as shown in Figure 5.6. The problem was traced back to incorrectly approximating the rapid neutrino oscillations. To calculate the oscillations, each energy bin is iterated over 100 times, an oscillation weight is calculated at each iteration and the average over that bin is used as the oscillation weight. For the charged current spectrum, the dominant oscillation, $\nu_\mu \rightarrow \nu_\mu$, oscillates rapidly between the values of 0 and 1 below 1 GeV. The rapid oscillations were being accounted for when oscillations were applied on an event by event basis but were washed out when applying the oscillations bin by bin, as illustrated in Figure 5.7. To better approximate the oscillation probability, finer binning was utilized for the analysis, as shown in Figure 5.8. Figure 5.9 shows the significant improvement

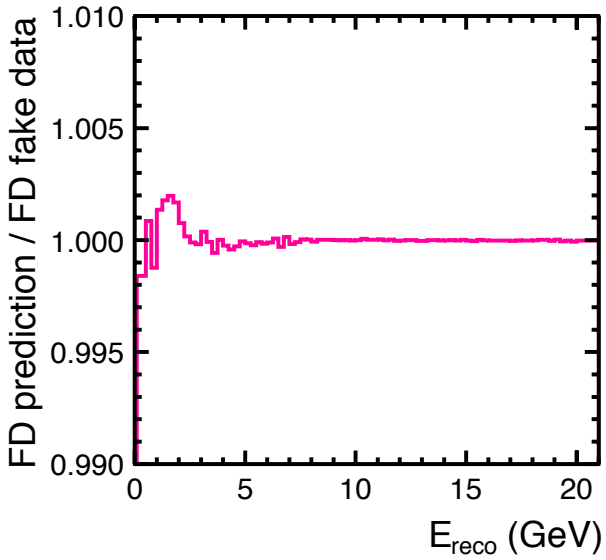

FIG. 5.5: A ratio of the fake far detector data spectrum and the far detector prediction. Four flavor oscillations were applied with $\theta_{13} = 0$.

from fine bins.

5.2.3 Sterile Neutrino Oscillations at the Near Detector

For $\Delta m^2_{34} \sim 1\,\mathrm{eV}^2$, $\nu_\mu \to \nu_s$ oscillations will occur at the near detector baseline of $\sim$ 1 km. Due to lack of prior knowledge of the NuMI neutrino flux, MINOS is incapable of identifying oscillations at the near detector, but because the far detector prediction is based on near detector data and Monte Carlo, neutrino oscillations into sterile neutrinos at the near detector have to be taken into account to properly predict the far detector spectrum. Figures 5.10 and 5.11 show how the neutral current and charged current spectra change with the inclusion of near detector oscillations. The change in the far detector prediction for the neutral current spectra is shown in Figure 5.12 and for the charged current spectra in Figure 5.13. At a value of $\Delta m^2_{34} = 4\,\mathrm{eV}^2$, a significant distortion in both the neutral current and charged current spectra for both detectors is visible, demonstrating the necessity of the inclusion of near detector oscillations.

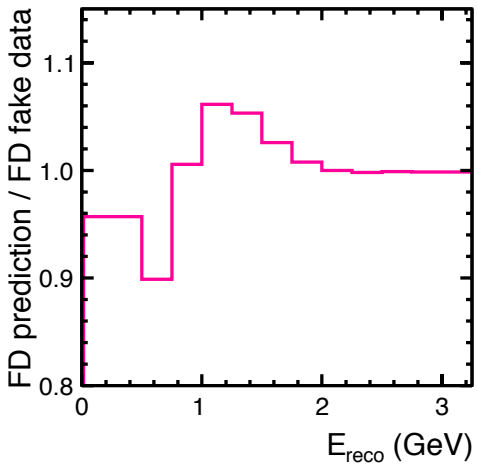

FIG. 5.6: A ratio of the fake far detector data spectrum and the far detector prediction. Four flavor oscillations were applied with $\theta_{13} = 0$. Significant discrepancies are seen below 2GeV.

5.2.4 Varying Baseline

For MINOS, neutrinos are created through pion decay as they travel through the decay pipe, a distance of 675m. As such, the baseline will actually have varying values since pions could decay anywhere throughout the decay pipe. Prior to the addition of near detector oscillations, the analysis was processed without accounting for the varying baseline due to the marginal change over the far detector baseline. With the addition of a near detector baseline of 1040 m into the oscillation probability, the effect of an exact baseline became relevant and therefore, a varying baseline was incorporated into the analysis. The first iteration of incorporating the varying baseline was to produce a 3D histogram of reconstructed energy vs. true neutrino energy vs. baseline, where L was defined as the near (far) baseline minus the neutrino production vertex. However, a 3D matrix took much longer to generate and because the oscillation probability depends directly on L/E and not just E, it was decided to generate 2D histograms of reconstructed energy vs. L/E.

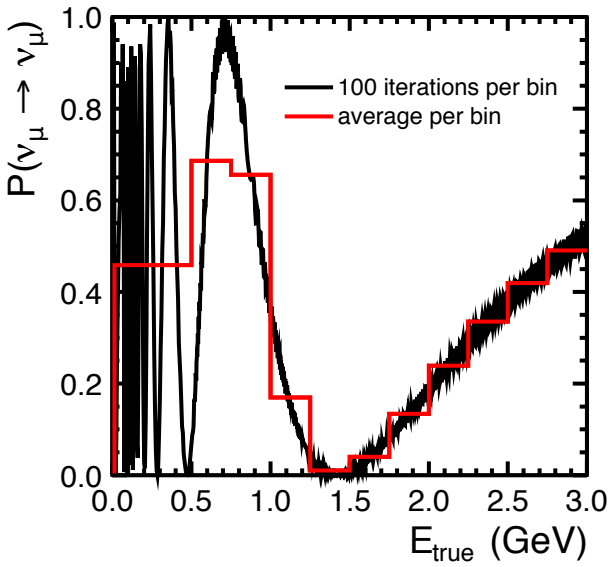

FIG. 5.7: The black line is showing the probability curve when when each of the 100 iterations over each energy bin is used. The red cureve is showing the averaged weight over each energy bin, which is the oscillation weight applied to the Monte Carlo.

Approximation

Incorporating a varying baseline resulted in discontinuities in the χ^2 surface around $\Delta m^2_{34} \geq 1\,\mathrm{eV}^2$, as shown in Figure 5.14. Given the exact four flavor oscillation probability, the oscillations are very rapid at high Δm^2_{34}. The implemented 2 km/GeV binning in the far detector spectrum is not sufficient to sample the oscillation curve using only the bin center, as shown in Figure 5.15. Finer binning is an option but results in the procedure taking too long when processing. However, taking the average would be a good enough approximation because MINOS is not sensitive to seeing every single wiggle in the oscillation probability. The four flavor oscillation depends on

$$\sin^2\left(\frac{1.27\Delta m^2_{34} L(km)}{E(GeV)}\right). \tag{5.3}$$

with a period in L/E of $\mathrm{T} \equiv \frac{\pi}{1.27\times\Delta m^2_{34}}$ and a width of $W \equiv$ bin width (km/GeV).

When $T \gg W$, sampling at the bin center is sufficient. But when $T \lesssim W$, the

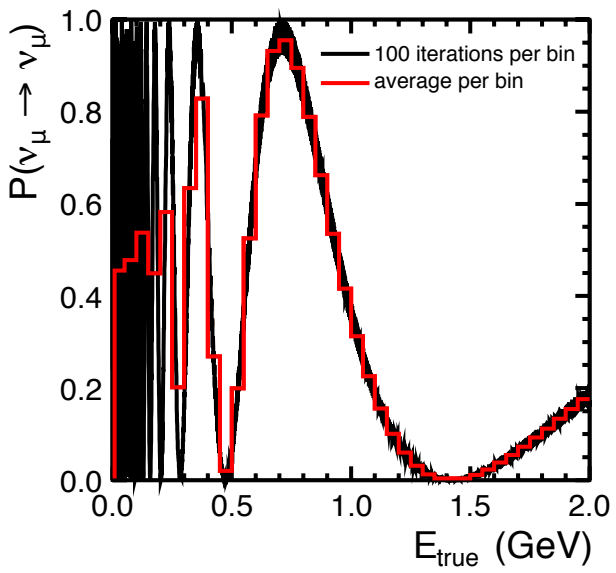

FIG. 5.8: The black line is showing the probability curve when each of the 100 iterations over each energy bin is used. The red curve shows the averaged weight over each energy bin, which is the oscillation weight applied to the Monte Carlo.

oscillations become very rapid and an average of the oscillation curve needs to be used. For the near detector, $T \lesssim W$ when $\Delta m^2_{34} = 989\text{eV}^2$. Because MINOS is not sensitive in that region, this approximation is not used on the near detector spectrum. At the far detector, however, depending on the binning, $T \lesssim W$ occurs at values as low as $\Delta m^2_{34} = 1.24\text{eV}^2$ and therefore an approximation is necessary. In order to perform the approximation, the period, T, will be calculated at a given Δm^2_{34}. The oscillation curve will then be sampled at the bin center $\pm$ T/4 and averaged. Figures 5.16 and 5.17 show two examples of this procedure.

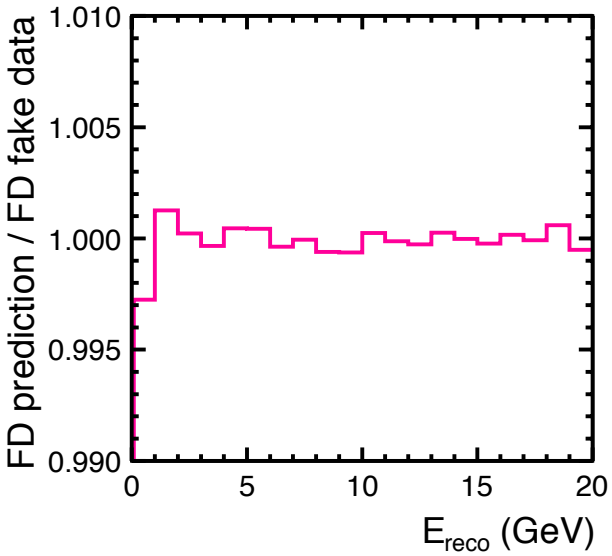

FIG. 5.9: A ratio of the fake far detector data spectrum and the far detector prediction.

5.3 χ^2 Minimization

The χ^2 method is used to calculate the agreement between the far detector prediction and the far detector data according to,

$$\chi^2 = 2\sum_{i=1}^{N}\left[e_i - o_i + o_i \ln\frac{o_i}{e_i}\right] + \sum_{j=1}^{N}\frac{\epsilon_j^2}{\sigma_j^2} \tag{5.4}$$

where, e_i is the expected number of events based on the far detector prediction for energy bin i and o_i is the observed number of events from the far detector data. The second sum includes systematic errors into the fit using nuisance parameters. In the second term of equation (5.4), ϵ_j corresponds to the shift from the nominal value due to the j^{th} systematic and σ_j is the uncertainty in the j^{th} systematic. Each ϵ_j is a separate fit parameter. The systematic uncertainties included in the fit are described in Chapter 6.

The expected number of events, e_i is a function of the oscillation parameters (mass splittings and angles), the far-over-near ratio, the near detector data, and the systematic nuisance parameters, ϵ_j. The systematic uncertainties are included in the χ^2 calculation as

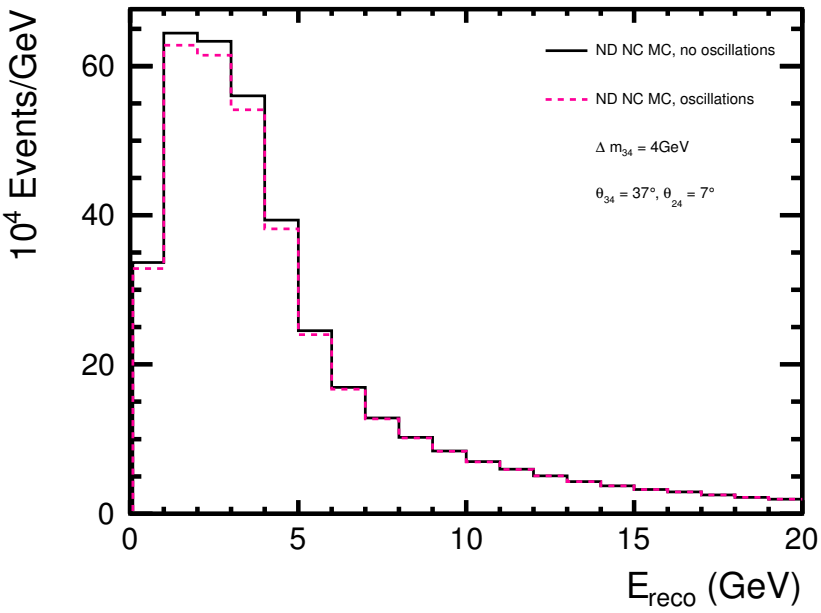

FIG. 5.10: The ND NC monte carlo spectra before and after the inclusion of ND oscillations. A significant distortion is visible at $\Delta m^2_{34} = 4\,\mathrm{eV}^2$.

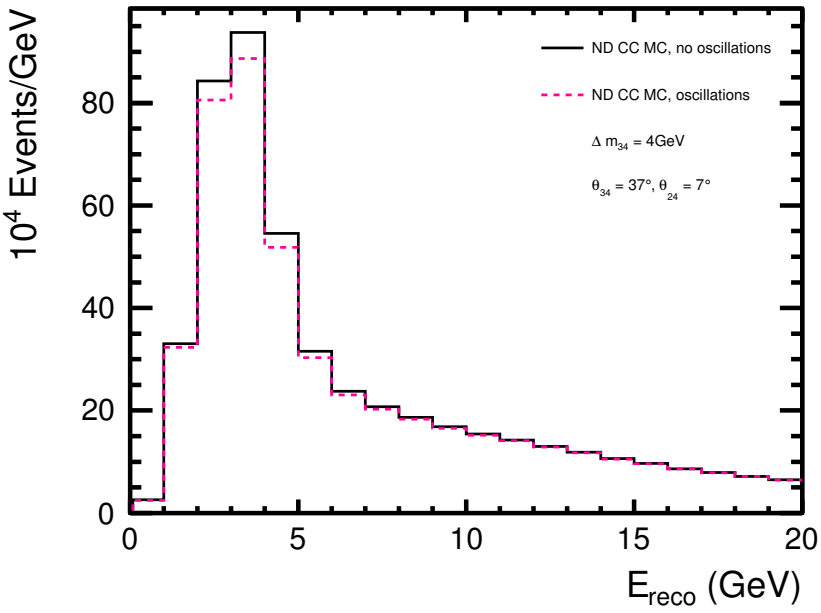

FIG. 5.11: The ND CC monte carlo spectra before and after the inclusion of ND oscillations. A significant distortion is visible at $\Delta m^2_{34} = 4\,\mathrm{eV}^2$.

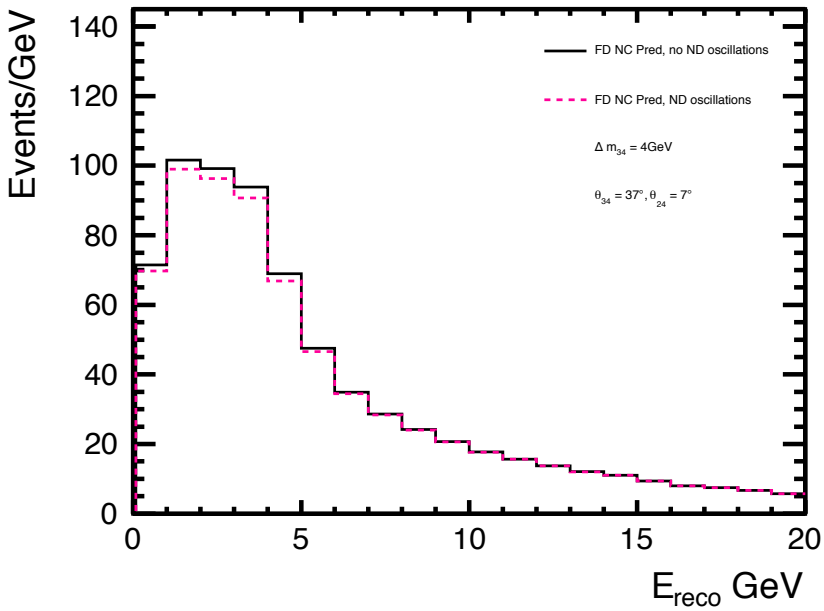

FIG. 5.12: The FD NC prediction before and after the inclusion of ND oscillations. A significant distortion is visible at $\Delta m^2_{34} = 4\,\mathrm{eV}^2$.

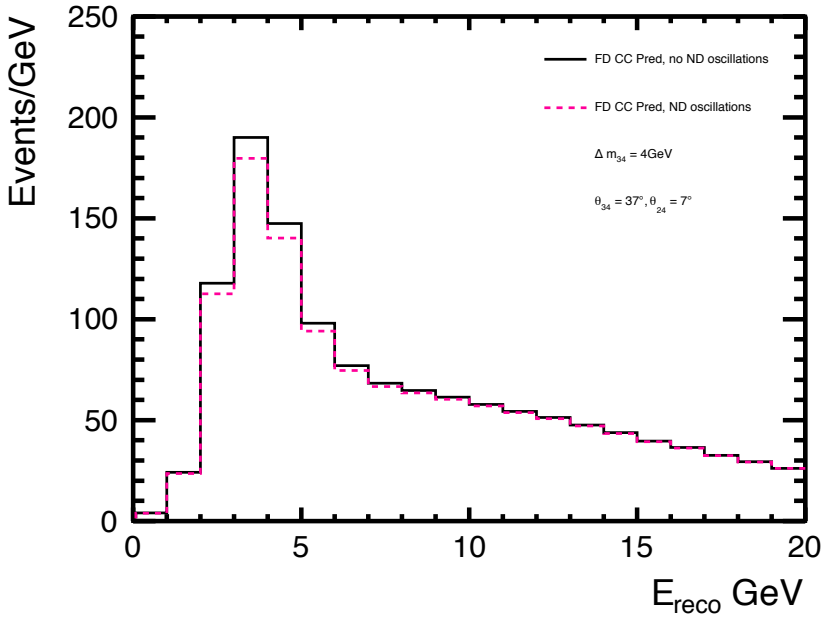

FIG. 5.13: The FD CC prediction before and after the inclusion of ND oscillations. A significant distortion is visible at $\Delta m^2_{34} = 4\,\mathrm{eV}^2$.

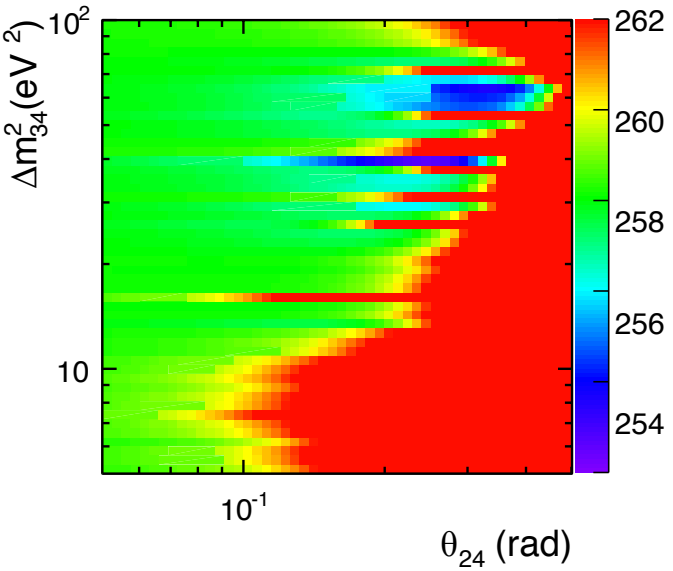

FIG. 5.14: A χ^2 surface for the Δm^2_{34} vs. θ_{24} parameter space. Discontinuities are visible around $\Delta m^2_{34} \geq 1$. The procedure for generating this χ^2 surface and its anomalies will be discussed in subsequent sections.

follows: for each systematic uncertainty, a $+1\sigma$ and a -1σ shifted, oscillated Monte Carlo sample is generated. The shifted reconstructed energy spectrum is divided by the nominal oscillated reconstructed energy spectrum. The far detector and near detector oscillated Monte Carlo spectrum is multiplied by the appropriate ratio ($+1\sigma$ or -1σ), scaled by the value $\frac{\epsilon_j}{\sigma_j}$. The far-over-near ratio is then the ratio of these systematic shifted, oscillated Monte Carlo spectra.

The χ^2 is calculated independently for both the neutral current and charged current spectra. The total χ^2 is the sum of the two:

$$\chi^2_{\text{TOTAL}} = \chi^2_{NC} + \chi^2_{CC}. \tag{5.5}$$

5.3.1 Fitting

The fit is performed over a χ^2 surface in the following parameter spaces: θ_{24} vs. θ_{34}, θ_{23} vs. θ_{34}, θ_{24} vs. θ_{23}, Δm^2_{34} vs. θ_{24}. At each point in the parameter space, which

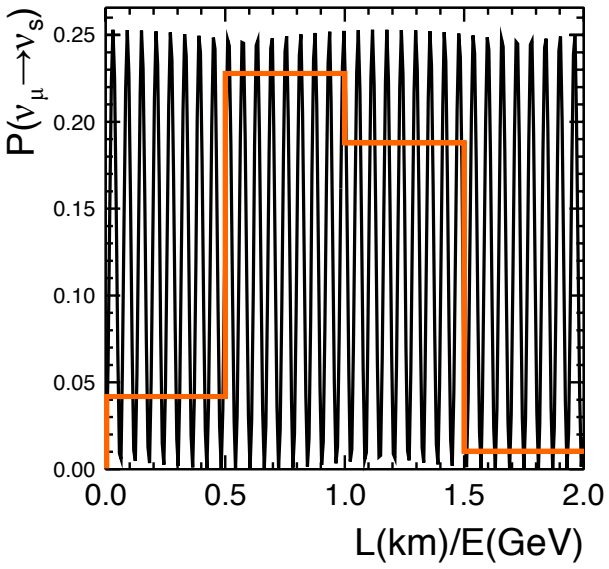

FIG. 5.15: The black curve represents the four flavor probability for $\nu_\mu \rightarrow \nu_s$ at $\Delta m^2_{34} = 40.99\text{eV}^2$ at the far detector baseline. The orange curve represents the calculated oscillation based on bin center.

Oscillation Parameter	Value
θ_{13}	$8.6°$
θ_{12}	$34.38°$
Δm^2_{12}	$0.0000759\ \text{eV}^2$
δ_1	0
δ_2	0

TABLE 5.1: Oscillation paramters which are fixed in the fit for the χ^2 minimization.

is 100 by 100 bins, the two axis variables are fixed to the bin centers. The other two physics parameters and the 11 nuisance systematics parameters are allowed to vary. With each iteration of the oscillation parameters, a new far detector prediction is produced and compared to the far detector data. MINUIT2 is used to find a set of oscillation parameters that minimize the χ^2 in Equation 5.4. The other parameters are always fixed to the specific values in Table 5.1. A global fit is also found by initially setting all free parameters to 0 and running MINUIT2.

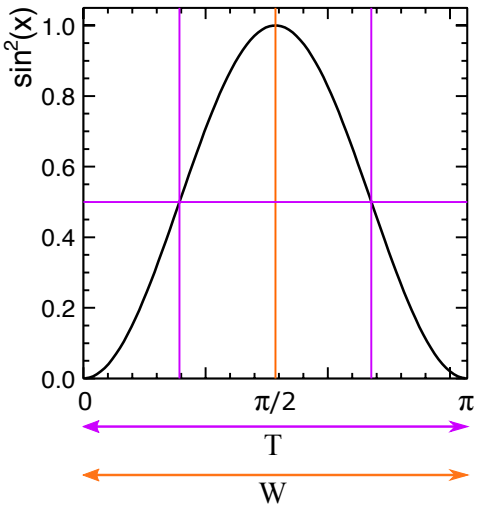

FIG. 5.16: An example of averaging a $\sin^2(x)$ probability over an energy bin of width W (arbitrarily scaled to π). The period of the oscillation, T, is identical to W in this case. The probability is sampled at the bin center (the vertical orange line) $\pm$ T/4 (the vertical purple lines). The averaged probability is the average of those two points (horizontal purple line).

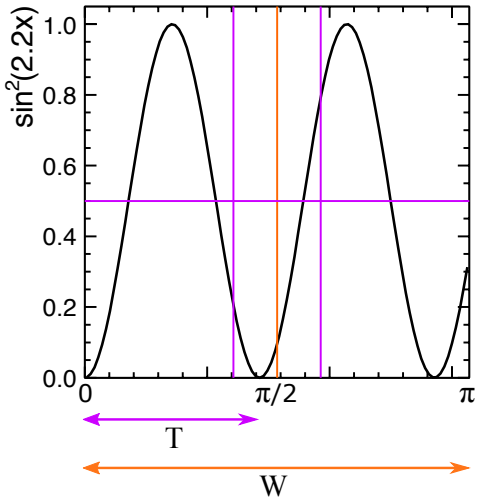

FIG. 5.17: An example of averaging a $\sin^2(x)$ probability over an energy bin of width W (arbitrarily scaled to π). The period of the oscillation, T, is smaller than W in this case. The probability is sampled at the bin center (the vertical orange line) $\pm$ T/4 (the vertical purple lines). The averaged probability is the average of those two points (horizontal purple line).

Discontinuities

A discontinuity was discovered when performing the χ^2 minimization over the phase spaces, Figure 5.18. A look at the 1D χ^2 distributions yielded the insight that θ_{23} had two minima. as shown in Figure 5.19 shows the octant symmetry of θ_{23}. The exact four flavor oscillation probability depends directly on θ_{23}, making it mildly sensitive to which octant θ_{23} is in. Depending on the value of Δm^2_{23}, θ_{34} and θ_{24}, the preferred octant for θ_{23} may vary, yielding a lower χ^2 in either one or the other octant, creating a discontinuity. Because of this mild sensitivity to θ_{23}, when θ_{23} was allowed to vary in the fit, the analysis was run with constraints on θ_{23} to each octant separately. The two χ^2 surfaces were compared and the lowest χ^2 was recorded as the global minimum. Confidence contours were based on the global χ^2 surfaces.

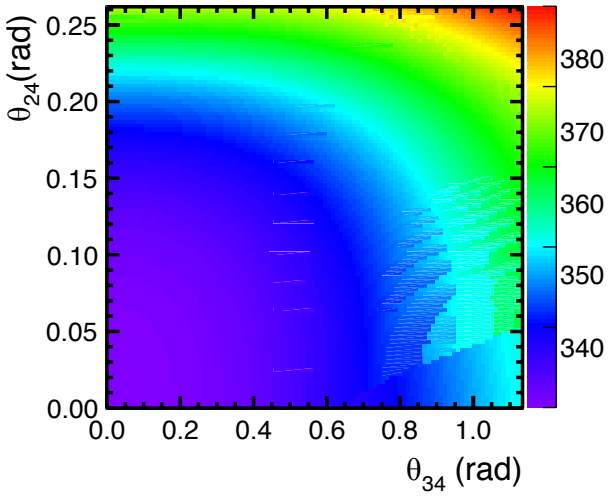

FIG. 5.18: A χ^2 surface for the θ_{24} vs. θ_{34} phase space is shown for data. A discontinuity is visible due to the mild sensitivity to θ_{23}.

5.4 Surface Contours

In order to generate a surface contour to set limits on possible values for oscillation parameters, the fit is implemented over a full parameter space for a set of physics parameters. Two of the physics parameters are fixed for a given point in the parameter space and the other 13 parameters are released. A minimization is performed and the minimum χ^2 is recorded at each point in the parameter space. The confidence level (C.L.) contours are generated using the χ^2 grid. Each χ^2 is subtracted from the best fit χ^2 and a contour is drawn at the corresponding confidence level according to Table 5.2.

(1-α) (%)	m = 1	m = 2
68	1.00	2.30
90	2.71	4.61

TABLE 5.2: $\Delta\chi^2$ values for confidence levels 1-α with m parameters, [66], where α is the sigma and m is the number of fixed parameters.

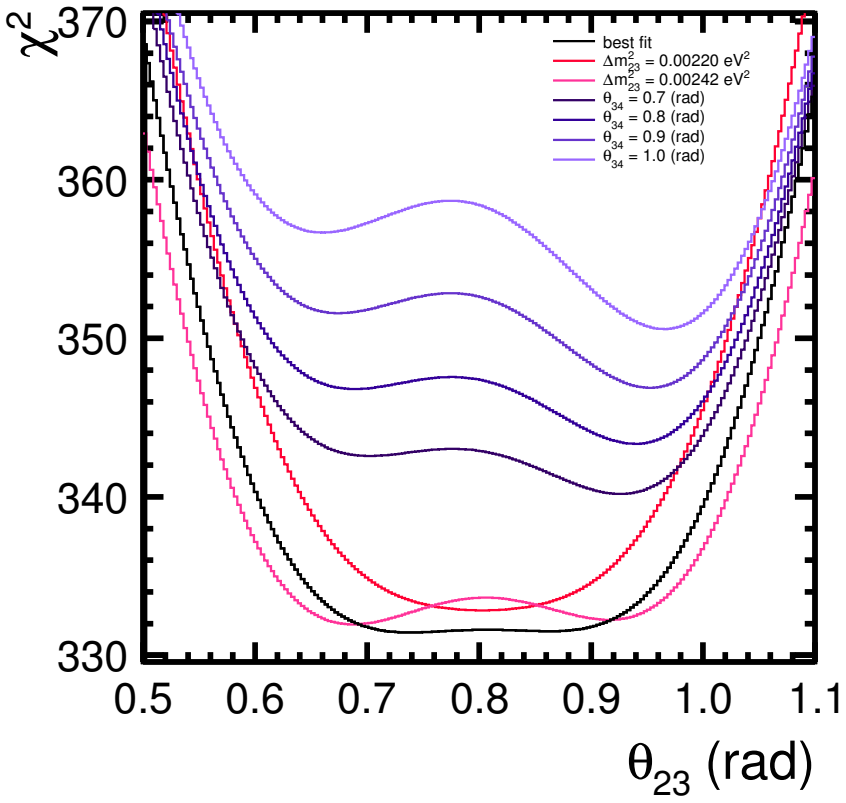

FIG. 5.19: 1D χ^2 distribution for θ_{23} when different parameters are varied. The χ^2 distribution is generated by fixings all parameters except θ_{23} and performing the χ^2 minimization. For different combinations of oscillation parameters, the best fit value of θ_{23} varies between the upper and lower octant. The different colors depict different versions of the fixed parameters. The purple lines show how the 1D χ^2 surfaces changes whtna θ_{34}. The change in whether the θ_{23} minimum is in found in either the upper or lower octant clearly shows why the analysis has to be run in both octants.

CHAPTER 6

Systematic Uncertainties

A number of systematic uncertainties have the potential to affect the best-fit oscillation parameters returned from the fitting procedure. The uncertainties could shift the energy of the events, the number of selected events, or the number of predicted background events. A description of the systematic uncertainties evaluated in this analysis is given below.

6.1 Uncertainties on NC selected events

6.1.1 NC Normalization

A dominant systematic for both the charged-current and neutral current analyses is the relative near/far normalization. The inter-detector normalization consists of several components. The largest contributor is the near/far selection bias which is any difference in reconstruction efficiency between the two detectors unaccounted for by Monte Carlo

simulation. If the double ratio of efficiencies,

$$\mathrm{R} = \frac{\epsilon^F_{data}/\epsilon^F_{MC}}{\epsilon^N_{data}/\epsilon^N_{MC}} \tag{6.1}$$

is equal to 1, there is no overall systematic effect. Therefore, in order to estimate an uncertainty, all four combinations of near/far and data/MC must be taken into account.

To obtain a value for the normalization systematic of NC selected events, a muon-removed charged current method was implemented. Here, hits associated with a muon from a CC sample are removed and the remaining hits are passed through the reconstruction again. The event may or may not be reconstructed in the second processing, therefore allowing a data-driven calculation of the reconstruction efficiency to be made. By running the procedure over all four combinations, the double ratio R is obtained. For NC-selected events this method yielded a 2% uncertainty on the near/far selection bias. Additionally, a near detector fiducial bias is calculated by dividing the near detector fiducial volume in half in x, y, z, and the data/MC ratio in each is calculated. The difference in the number of events in each half is calculated to be 0.53%, 0.14%, and 0.43% respectively. A third component comes from measuring how well the live time and the proton on target (POTs) counting of the detectors relative to each other is known. Comparing the POTs from files to the POTs from the database yields a contribution to the normalization uncertainty of 0.32%. Finally, the detector steel thickness and scintillator thickness are both known to 0.2%. Adding all the components in quadrature gives a value of 2.2% as the normalization uncertainty for NC-selected events [77].

6.1.2 CC Background

The uncertainty on the charged-current background in the neutral current spectrum is evaluated with two separate methods. The first method is described in detail in [77] and

takes advantage of the particle identification (PID) methods available for distinguishing between charged-current and neutral-current events. Neutral-current selected events are input into a PID and the output value is histogrammed for both data and Monte Carlo. True charged-current and true neutral-current components are histogrammed separately for Monte Carlo. The Monte Carlo is then fit to the data by scaling the charged-current and neutral-current components to minimize the χ^2 between the data and Monte Carlo for each energy bin. For a given energy bin, the total number of Monte Carlo events consists of the charge-current components, c_i, and the neutral-current component, n_i, and the data value, d_i, such that

$$X_i n_i + Y_i c_i = d_i \tag{6.2}$$

and a fit is found for scale factors X_i and Y_i in order to minimize the χ^2. Using this method with two different PIDs gives an uncertainty on the order of 20% [78].

The second method takes advantage of data taken with different beam configurations. The total number of events, N^{LE}, in the low energy beam configuration consists of a charged-current component, N_{cc}^{LE}, and a neutral current component, N_{nc}^{LE},

$$N^{LE} = N_{cc}^{LE} + N_{nc}^{LE}. \tag{6.3}$$

For an alternate beam configuration (i.e. medium energy, high energy, or horn-off), the total number of events, N^{alt}, can be written as

$$N^{alt} = r_{cc} N_{cc}^{LE} + r_{nc} N_{nc}^{LE} \tag{6.4}$$

where $r_{cc} = N_{cc}^{alt}/N_{cc}^{LE}$ and $r_{nc} = N_{nc}^{alt}/N_{nc}^{LE}$ are defined as ratios of the true charged-current or neutral-current events between the two beam configurations. These ratios are

calculated from Monte Carlo. Equations 6.3 and 6.4 can be solved to obtain

$$N_{cc}^{LE} = (N^{alt} - r_{nc}N^{LE})/(r_{cc} - r_{nc})$$

$$N_{nc}^{LE} = (N^{alt} - r_{cc}N^{LE})/(r_{nc} - r_{cc}) \tag{6.5}$$

A weighted average is obtained from three beam pairings, LE/Horn-off, LE/ME, and LE/HE [78]. The measurement is cut off at 8GeV due to the fact that the charged current and neutral current ratios look the same above 8 GeV. This method gives a 15% uncertainty of the charged current background in the neutral current spectrum which is used in this analysis.

6.1.3 Relative Hadronic Energy

The near-far relative energy scale uncertainty on the overall shower energy arises when the same shower occurring in the near and far detectors is given a different reconstructed energy. Because the MINOS detectors are calibrated to give the same response, the uncertainty comes from residual differences after the calibration procedure. The uncertainty is the sum in quadrature of the systematic uncertainties on each stage of the calibration chain and has been calculated to be 2.1% [79].

6.1.4 Absolute Hadronic Energy

An uncertainty on the absolute shower energy arises when a shower of given energy, E, receives a different average reconstructed energy in data and Monte Carlo. This uncertainty has two parts. The first is the uncertainty on the overall detector response to single hadrons. This uncertainty was calculated to be 5.7% using the MINOS calibration detector [79]. The second part of the uncertainty arises from hadron shower modeling in Monte

Carlo. Due to intranuclear rescattering, where low energy pions in the final state interact with nucleons before being detected, some of the energy transferred to the hadronic system is lost. The uncertainties of this effect are large and energy dependent. A study of the hadronic modeling and an estimate of the uncertainty was conducted in [80]. The study used samples of Monte Carlo events and altered the parameters controlling intranuclear rescattering within their uncertainty to quantify the effect on the reconstructed energy. Parameters included pion branching ratios, cross sections for the pion absorption, formation times, and changes to the hadronization models used in the generation of hadronic showers. This resulted in a true energy dependent systematic uncertainty. Combining this with the 5.7% calibration uncertainty gives an overall absolute hadronic energy systematic of [79]

$$\frac{\sigma_E}{E} = \begin{cases} 5.7\% \oplus 8.2\%, & \text{if } \mathrm{E}_{True}^{shower} \leq 0.5 \text{ GeV} \\ 5.7\% \oplus (2.7\% + 3.7\% \times e^{-0.25\mathrm{E}_{True}^{shower}}), & \text{if } 0.5 < \mathrm{E}_{True}^{shower} \leq 10 \text{ GeV} \\ 5.7\% \oplus 3.0\%, & \text{if } \mathrm{E}_{True}^{shower} > 10 \text{ GeV} \end{cases} \tag{6.6}$$

where $\oplus$ means adding in quadrature.

6.1.5 Near Detector Cleaning

The addition of higher intensity data in runs 5, 6, and 10 resulted in a large pile-up of low energy showers within a spill in the near detector. Low-energy showers are a background to the neutral current selection and lead to reconstruction failures of a large number of poorly reconstructed events. Two pre-selection cuts which are meant to reduce the number of poorly reconstructed events [81]. A cut is placed on the fraction of the pulse height in the slice that belongs to the event and the largest number of consecutive

planes hit in the event. Poor modeling of the low energy showers and the two cleaning variables lead to near detector data and Monte Carlo discrepancies that result in an energy dependent systematic uncertainty on the far detector prediction.

The systematic has been evaluated as a combination of the effect of the uncertainty on the poorly reconstructed events and on the effect of the cleaning cut position. For the uncertainty of the poorly reconstructed events, a scaling factor is used that minimizes the combined χ^2 from the fit between data and Monte Carlo for the two cleaning variables. After scaling the component of poorly reconstructed events in the Monte Carlo, the nominal position of each cut in the Monte Carlo is moved so that it matches the fraction of events rejected by the nominal cut position in data. The uncertainty is then calculated to be the ratio of the near detector energy spectrum with the modified cuts and the energy spectrum with the nominal cuts, for each energy bin. The overall systematic uncertainty is the average of the two results. In order to make binning less relevant, a continuous empirical model, $a/(1 + E/b)^2$, has been implemented in the analysis [82] with $a = 8.2\%$ and $b = 3.0$ GeV gives an overall near detector cleaning systematic as a scaling of events by

$$8.2\%/(1 + \mathrm{E}_{Reco}/3 \text{ GeV}).$$

6.1.6 Far Detector Cleaning

The uncertainty on the event selection in the far detector is broken up into two systematics, one relating to cuts intended to remove noise and one for the cuts intended to remove cosmic ray muons. A study on the far detector cleaning was conducted in [71]. Different neutral-current spectra are generated by shifting a cut position up and down by a value based on the RMS of the distribution of Monte Carlo events in each cut variable. The systematic uncertainty is taken as the ratio of the reconstructed energy spectrum with

the shifted cut and with the nominal cut. The far detector noise cleaning systematic is determined to be [71]

$$4.9\% \text{ if } \mathrm{E}_{Reco}^{shower} \leq 0.5 \text{ GeV},$$

$$1.0\% \text{ if } 0.5 < \mathrm{E}_{Reco}^{shower} \leq 1.0 \text{ GeV},$$

$$0.6\% \text{ if } 1.0 < \mathrm{E}_{Reco}^{shower} \leq 2.0 \text{ GeV},$$

$$0.4\% \text{ if } 2.0 < \mathrm{E}_{Reco}^{shower} \leq 3.0 \text{ GeV},$$

$$0.5\% \times e^{\mathrm{E}_{Reco}^{shower}/7.1} \oplus 1.6\% \times e^{-\mathrm{E}_{Reco}^{shower}/1.1} \text{if } \mathrm{E}_{Reco}^{shower} > 3 \text{ GeV}.$$

While the far detector cosmic cleaning systematic is calculated to be [71]

$$1.1\% \text{ if } \mathrm{E}_{Reco}^{shower} \leq 0.5 \text{ GeV},$$

$$2.7\% \text{ if } 0.5 < \mathrm{E}_{Reco}^{shower} \leq 1.0 \text{ GeV},$$

$$2.3\% \text{ if } 1.0 < \mathrm{E}_{Reco}^{shower} \leq 2.0 \text{ GeV},$$

$$2.1\% \text{ if } 2.0 < \mathrm{E}_{Reco}^{shower} \leq 3.0 \text{ GeV},$$

$$7.4\% \times e^{\mathrm{E}_{Reco}^{shower}/0.98} \oplus 2.1\% \times e^{-\mathrm{E}_{Reco}^{shower}/20.8} \oplus 1.2\% \times e^{-\mathrm{E}_{Reco}^{shower}/5.5} \text{if } \mathrm{E}_{Reco}^{shower} > 3 \text{ GeV}.$$

6.2 Uncertainties on CC selected events

6.2.1 CC Normalization

The normalization systematic for CC-selected events is computed almost identically to the NC-selected events as described in section 6.1.1. The one exception being in the method used to calculate the near/far selection bias. For CC-selected events a study was

conducted that involved hand-scanning a number of events in all four combinations to search for events that failed reconstruction and events that were moved in or out of the fiducial volume. This method calculated a 1.3% uncertainty for the near/far selection bias. When all components of the normalization systematic are added in quadrature, a value of 1.6% overall systematic is computed for CC-selected events [77].

6.2.2 NC Background

The neutral current background in the charged current spectrum occurs due to mis-modeling of hadronic showers and neutral current cross sections in the Monte Carlo. For a direct comparison between data and Monte Carlo, muon tracks are removed from reconstructed charged current events, leaving only the hadronic shower, in both data and Monte Carlo. These muon-removed charge current events are then put through the reconstruction to study the rate of accidentally reconstructing a charged current event from data and Monte Carlo. This study was documented in [83] and an uncertainty of 20% on the number of neutral current events in the charge current selected spectrum was inferred.

6.2.3 Absolute Hadronic Energy

The energy dependent form of the shower modeling uncertainty is added in quadrature with the 5.7% calibration and CalDet uncertainties, which results in a total uncertainty on the shower energy. This energy dependent form is then parameterized according to [84]

$$\frac{\sigma_E}{E} = 6.6 + 3.5e^{\frac{\mathrm{E_{shw}}}{1.44\mathrm{GeV}}}. \tag{6.7}$$

The error is taken to be fully correlated bin-to-bin.

6.2.4 Absolute Track Energy

An uncertainty of 2% is applied to track energies which are measured by range and a 3% uncertainty is applied to track energies measured by curvature [68]. The error for range measurements is calculated from the uncertainty in the detector simulation, detector density and geometry, and from uncertainties from particle propagation. The curvature measurement error incorporates differences in the range and curvature measurements from individual stopping muon tracks [74].

CHAPTER 7

Results

This analysis was conducted in two phases. First, the results of a comparison to the standard three flavor oscillation model is presented. Second, the data are fit to the 3+1 model at a fixed $\Delta m^2_{34} = 0.5\,\mathrm{eV}^2$.

Figure 1.3 displays the oscillation probability as a function of L/E for three values of Δm^2_{34}. At small Δm^2_{34} ($0.05\,\mathrm{eV}^2$), oscillations occur in the far detector at high energies but not in the near detector at any neutrino energy available at NuMI. The largest effect in the far detector is visible where beam flux uncertainties are larger. At large Δm^2_{34} ($5.0\,\mathrm{eV}^2$), there are significant oscillations in the near detector and a constant deficit in the far detector. This constant deficit occurs because the rapid oscillations are smeared by the energy resolution of the detector such that the average of the oscillation probability is observed. The far detector prediction is based on the far-over-near ratio which depends on the flux model at the two detectors. Due to this dependance, the flux model and uncertainties need to be accurate. Uncertainties is the flux model need to be properly included in the fit and the correlations between energy bins must be taken into account. Otherwise, discrepancies in the flux model could be fit as oscillations, a detail that was

not fully explored in this thesis. At medium Δm^2_{34} ($0.5\,\mathrm{eV}^2$), there are no oscillations at the near detector and the oscillations in the far detector are rapid. The effect smears out to create an overall deficit, which effectively results in a far detector counting experiment. Therefore, for this analysis, all four flavor fits were conducted at a fixed $\Delta m^2_{34} = 0.5\,\mathrm{eV}^2$.

7.1 Three flavor comparison

The analysis was conducted using the methods described in the previous chapters. The far detector data was compared to Monte Carlo generated with the standard three-flavor oscillation probability. The three flavor comparison is run twice, once with θ_{23} constrained to the upper octant and once with θ_{23} is constrained to the lower octant.

The number of expected neutral current events including uncertainties is shown in Table 7.1. From the far detector data, 1221 events were selected as neutral current candidates. The observed number of events agrees with the prediction within the estimated uncertainties. No deficit in the neutral current spectrum is observed, therefore, the data is consistent with three-flavor oscillations. Figures 7.1 and 7.3 show the far detector neutral current spectrum when θ_{23} is constrained to either the upper or lower octant. The observed neutral current spectrum agrees well with either prediction.

θ_{23}	Number of Expected Events	Observed
$\theta_{23} < 45°$	$1182.87 \pm 34.39(\mathrm{stat}) \pm 36.12(\mathrm{syst})$	1221
$\theta_{23} > 45°$	$1168.48 \pm 34.18(\mathrm{stat}) \pm 36.12(\mathrm{syst})$	

TABLE 7.1: The number of expected neutral current events in the far detector.

θ_{23}	Number of Expected Events	Observed
$\theta_{23} < 45°$	$2604.91 \pm 51.04(\mathrm{stat}) \pm 51.93(\mathrm{syst})$	2712
$\theta_{23} > 45°$	$2623.3 \pm 51.22(\mathrm{stat}) \pm 52.12(\mathrm{syst})$	

TABLE 7.2: The number of expected charged current events in the far detector.

The expected number of charged current events including uncertainties is shown in Table 7.2. A total of 2712 charged current events were observed in the data, consistent with the uncertainties on the prediction. Figures 7.2 and 7.4 show the far detector charged current spectrum in the two octants of θ_{23}. The observed charged current spectrum agrees well with either prediction.

R Statistic

To quantify the agreement between data and the three flavor prediction, the number of neutral current events observed in the far detector data is compared to the number of events expected from standard three flavor oscillations. The comparison is done via the R statistic,

$$R \equiv \frac{N_{data} - B_{CC}}{S_{NC}} \tag{7.1}$$

where, within a given energy range, N_{data} is the observed event count, B_{CC} is the extrapolated charged current background from all flavors, and S_{NC} is the extrapolated number of neutral current interactions. If $R = 1$, no neutral current deficit is observed. The R statistic is calculated in three energy ranges, $0\,\text{GeV} < E_{reco} < 200\,\text{GeV}$, $3\,\text{GeV} < E_{reco} < 200\,\text{GeV}$, and $E_{reco} < 3\,\text{GeV}$. The R values with θ_{23} constrained to the lower(upper) octant are shown in Table 7.3(7.4). In all cases, the R values are consistent with 1 to within uncertainties, quantifying the agreement with the three flavor oscillation model.

E_{reco} GeV	$R\pm$ (stat) $\pm$ (syst)
0 – 200	1.07 $\pm$ 0.045 $\pm$ 0.060
3 – 200	1.03 $\pm$ 0.068 $\pm$ 0.065
0 – 3	1.11 $\pm$ 0.059 $\pm$ 0.080

TABLE 7.3: R statistic with $\theta_{23} < 45°$.

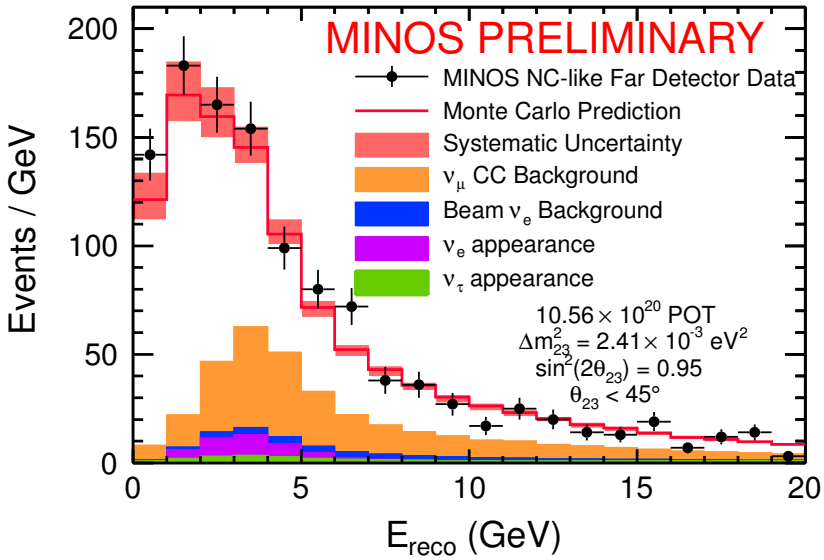

FIG. 7.1: Neutral current energy spectum in the far detector for 10.56×10^{20} POTs. Monte Carlo prediction is based on three flavor oscillations with $\theta_{23} < 45°$. Monte Carlo is plotted with its systematic uncertainty. Data is plotted with its statistical uncertainty.

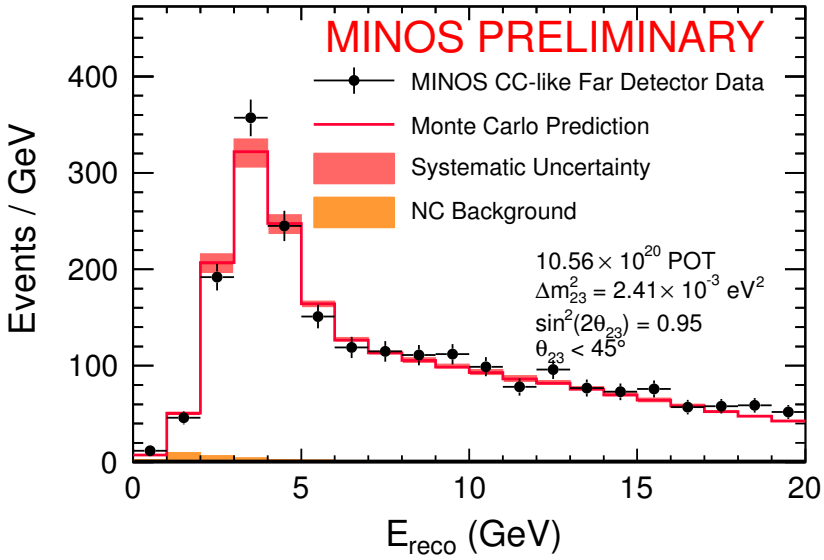

FIG. 7.2: Charged current energy spectum in the far detector for 10.56×10^{20} POTs. Monte Carlo prediction is based on three flavor oscillations with $\theta_{23} < 45°$. Monte Carlo is plotted with its systematic uncertainty. Data is plotted with its statistical uncertainty.

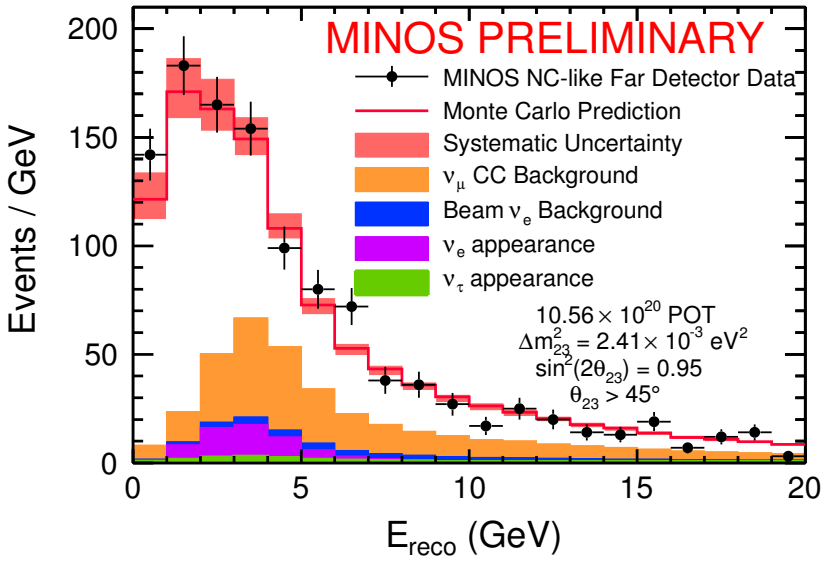

FIG. 7.3: Neutral current energy spectum in the far detector for 10.56×10^{20} POTs. Monte Carlo prediction is based on three flavor oscillations with $\theta_{23} > 45°$. Monte Carlo is plotted with its systematic uncertainty. Data is plotted with its statistical uncertainty.

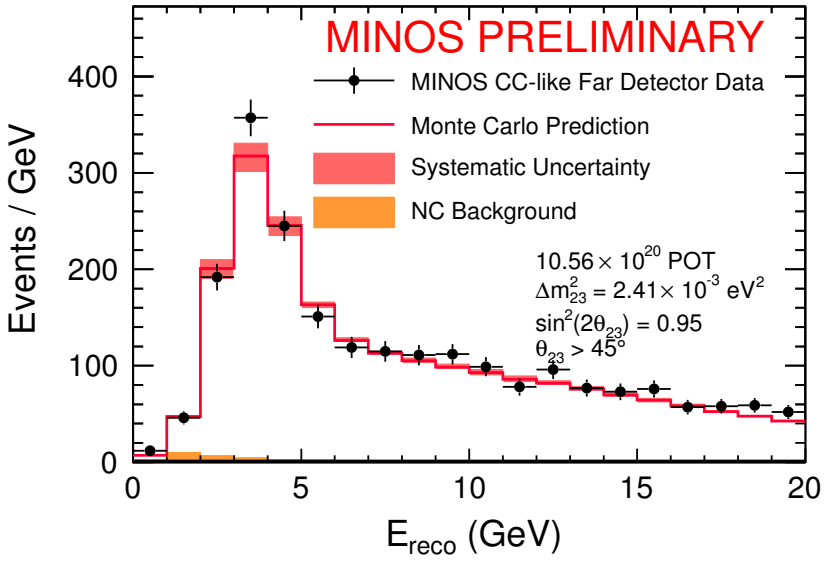

FIG. 7.4: Charged current spectum in the far detector for 10.56×10^{20} POTs. Monte Carlo prediction is based on three flavor oscillations with $\theta_{23} > 45°$. Monte Carlo is plotted with systematic uncertainty. Data is plotted with its statistical uncertainty.

E_{reco} GeV	$R\pm$ (stat) $\pm$ (syst)
0 – 200	1.05 $\pm$ 0.045 $\pm$ 0.061
3 – 200	1.01 $\pm$ 0.068 $\pm$ 0.069
0 – 3	1.09 $\pm$ 0.059 $\pm$ 0.080

TABLE 7.4: R statistic with $\theta_{23} > 45°$.

7.2 Four flavor comparison

While the data is consistent with three flavor oscillations, fitting the data to the 3+1 model allows us to place constraints on the parameters of that model. As stated previously, we will only consider the case where Δm^2_{34} is fixed at $\Delta m^2_{34} = 0.5\,\mathrm{eV}^2$. The best fit values of the four flavor fit are summarized in Table 7.5. Figure 7.5 shows the 90% C.L. for each pair of oscillation parameters. Included in each contour is the overall best fit point. The upper octant for θ_{23} is slightly preferred. Figure 7.6 shows the projections of $\Delta\chi^2$ as a function of the different oscillation parameters. The 90% C.L. limits on the three angles are as follows: $\theta_{24} < 4.8°$, $\theta_{34} < 23.9°$, and $37.0° < \theta_{23} < 54.5°$. This further constrains the allowed region of θ_{24} and θ_{34} from the previous MINOS sterile neutrino analysis which reported limits of $\theta_{24} < 7°$ and $\theta_{34} < 26°$ [1].

The global best fit at $\Delta m^2_{34} = 0.5\,\mathrm{eV}^2$ yields the values $\theta_{24} = 3.012 \times 10^{-6}$ and $\theta_{34} = 4.99 \times 10^{-4}$. These are approximately zero and confirm that the three flavor model is the best fit to the data.

Combined with Bugey

As a comparison to the LSND and MiniBooNE experiments, this result was combined with the constraints on θ_{14} from the Bugey experiment [85]. The Bugey experiment measured the energy spectra of electron antineutrinos from the Bugey nuclear reactor with a ^{6}Li-loaded liquid scintillator detector at a short baseline. The LSND and MiniBooNE experiments were based on a two flavor fit which involved one sterile mass splitting, Δm^2

(effectively Δm^2_{34}) and one sterile angle $\theta_{\mu e}$. When using the 3+1 model, $\theta_{\mu e}$ can be expressed in terms of θ_{14} and θ_{24} in the following manner [86]:

$$\sin^2 2\theta_{\mu e} = \sin^2 2\theta_{14} \sin^2 \theta_{24} \tag{7.2}$$

To combine the two results, for every Δm^2 and $\theta_{\mu e}$, the smallest χ^2 is found by iterating over all combinations of θ_{14} and θ_{24} consistent with $\sin^2 2\theta_{\mu e}$ and summing the χ^2 from MINOS and Bugey. Figure 7.7 shows the MINOS result for $\Delta m^2_{34} = 0.5\,\mathrm{eV}^2$ compared to LSND, MiniBoone, and Karmen, and combined with Bugey. For this one value of Δm^2_{34}, the allowed regions of the LSND and MiniBooNE experiments are excluded at the 90% C.L.

	Best fit values
Δm^2_{23}	2.338×10^{-3}
θ_{23}	0.8143
θ_{24}	3.012×10^{-6}
θ_{34}	0.000499
Norm. CC	1.01083
Shw. Scale	-0.56991
Trk. Scale	-0.267869
NC background	0.990316
Norm. NC	0.99916
Abs. Shw. NC	0.602654
Rel. Shw. NC	-0.559182
CC background	-0.395133
FD cleaning	0.135281
ND cleaning	-0.606918
FD cosmics	0.210409
χ^2/d.o.f.	1.1852

TABLE 7.5: Global best fit values for all free parameters. Δm^2_{34} fixed at $0.5\,\mathrm{eV}^2$. The degrees of freedom (d.o.f) correspond to the number of energy bins used in the χ^2 and is equal to 233.

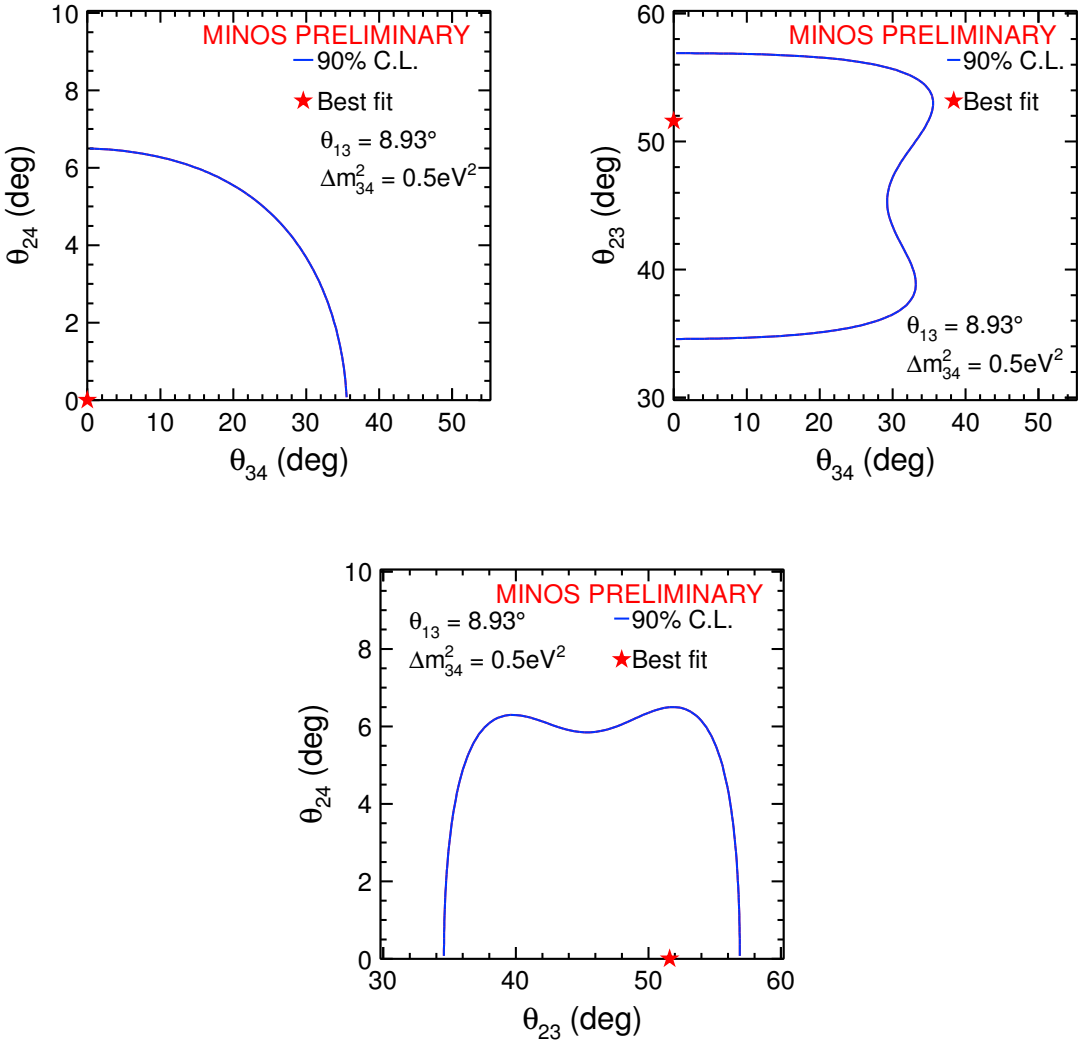

FIG. 7.5: Contours representing the 90% C.L. for these pair of parameters with a four flavor oscillation fit.

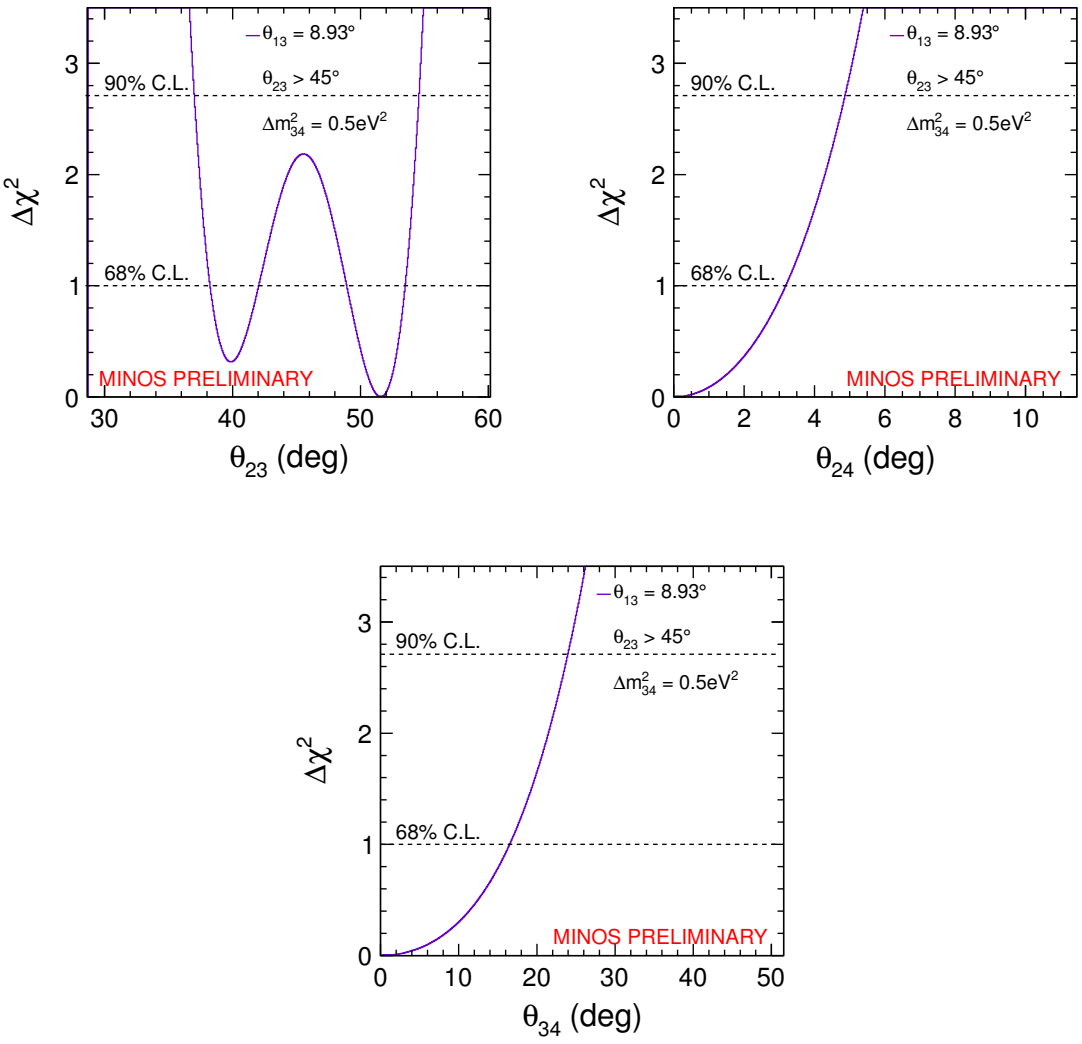

FIG. 7.6: Projections of $\Delta\chi^2$ as a function of the different oscillation parameters. The values of $\Delta\chi^2$ at the 68% and 90% C.L. are also shown.

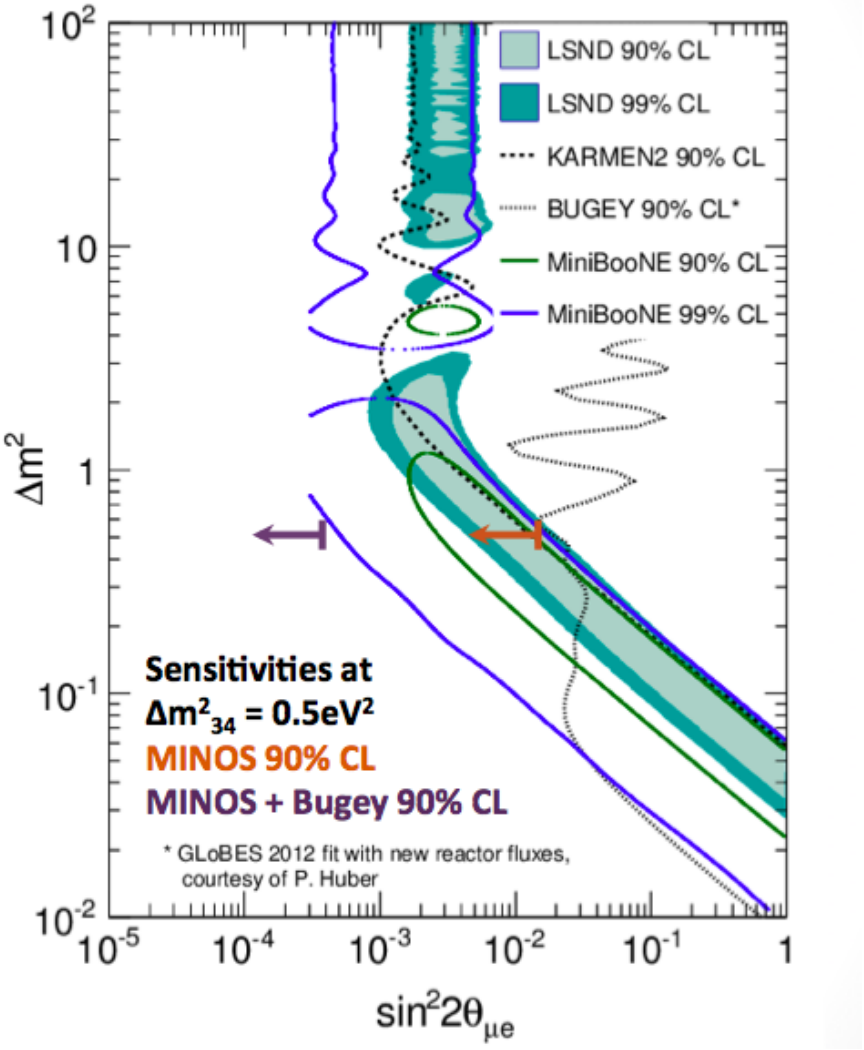

FIG. 7.7: LSND, MiniBooNE appearance signal compared to Karmen and Bugey. The Bugey limit is recomputed by Patrick Huber taking into account the new reactor flux calculations by Mention et al. [31]. The region to the right of the orange error is excluded by MINOS at 90% C.L. for Δm^2_{34}. When our result is combined with Bugey, the region to the right of the purple arrow is excluded at 90%C.L.

CHAPTER 8

Conclusion

The sterile neutrino analysis presented here included an additional 3.5×10^{20} POT forward horn current data [1]. An exact 3+1 neutrino oscillation model was implemented, allowing for oscillations occurring at the near detector. This is necessary because in the sterile mass range preferred by the LSND experiment ($\sim 1.0\,\mathrm{eV}^2$), oscillations into the sterile flavor occur at the near detector baseline. In order to better follow the oscillation curve, the binning was made finer and performed as a function of L/E rather than E. The exact 3+1 oscillation model has a direct dependance on the octant of θ_{23}, requiring the analysis to be performed separately for each octant.

The observed data was consistent with the three flavor oscillation model. No evidence for oscillations into sterile neutrinos was observed. Incorporating the 3+1 model at Δm^2_{34} $= 0.5\,\mathrm{eV}^2$ and fitting the sterile mass angles, θ_{24} and θ_{34}, we found a global best fit of approximately zero, which reduces the 3+1 model to a three flavor oscillation. Combining the results with Bugey excludes the allowed regions of LSND and MiniBooNE at Δm^2_{34} $= 0.5\,\mathrm{eV}^2$ at a 90% C.L.

8.1 Extending to a full range of Δm^2_{34}

While this result provides useful constraints on the intermediate sterile mass splitting range, extending the analysis to a broader range of Δm^2_{34} would extend the physics impact. Naively freeing Δm^2_{34} in the fit resulted in a best fit at $\Delta m^2_{34} = 56\,\mathrm{eV}^2$, suggesting the presence of sterile neutrinos, Figure 8.1. This result, however, is statistically insignificant because $\Delta\chi^2 = 4.6$, where

$$\Delta\chi^2 = \mid \chi^2_{\text{best fit}} - \chi^2_{\text{global}} \mid . \tag{8.1}$$

According to Table 5.2, this best fit value is within 90% C.L. of the three flavor oscillation model. Also, the phenomenology of oscillations at this high value of Δm^2_{34} suggests that a

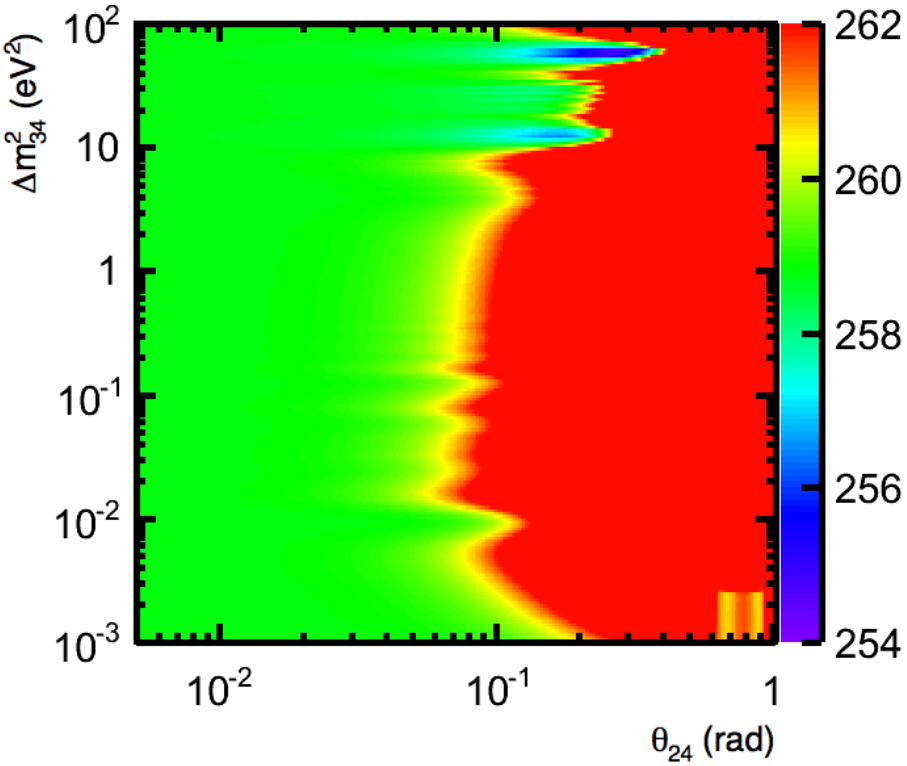

FIG. 8.1: The χ^2 surface of Δm^2_{34} vs. θ_{24}. The best fit point is found at $\Delta m^2_{34} = 56\,\mathrm{eV}^2$.

systematic effect is responsible. At $\Delta m^2_{34} = 0.5\,\mathrm{eV}^2$, the oscillations at the near detector

are rapid and smeared by the energy resolution such that in the peak of the flux there would exist a constant deficit. In the high energy tail, a shape could perhaps be observed, but this is the region where flux uncertainties are the largest (Figure 8.2). As stated previously, above $\Delta m^2_{34} = 0.5\,\mathrm{eV}^2$, the oscillations in the far detector are sufficiently rapid to reduce the observation to a counting experiment (Figure 8.3). For this result to be convincing, it would be necessary to observe a shape discrepancy in a region where the flux is well understood. If Δm^2_{34} is small, a shape discrepancy would be observed in the far detector with no change in the near detector. At larger Δm^2_{34}, a discrepancy would be observed in the near detector with a constant deficit in the far detector.

For this analysis to succeed at all values of Δm^2_{34} it is necessary to properly account for the bin to bin correlation systematics in the neutrino flux. Since the completion of this analysis, the MINOS collaboration continued to improve the methods described here in an attempt to fully understand the results. The 2014 sterile neutrino analysis was conducted with the following changes:

1. Instead of using the near detector data to predict a far detector spectrum, the F/N ratios of the charge current and neutral current events were evaluated.

2. Systematic uncertainties due to hadron production, acceptance, cross-sections, energy scales, and beam optics were re-evaluated and combined with statistical uncertainties to form a covariance matrix, which was applied to the F/N ratio.

3. A Feldman-Cousins correction was applied to the χ^2 surface.

With these changes the analysis was able to extend the fit over a broader range of Δm^2_{34}. Their combined result [86] with the Bugey [85] experiment has placed stringent constrains on the allowed regions for LSND and MiniBooNE results.

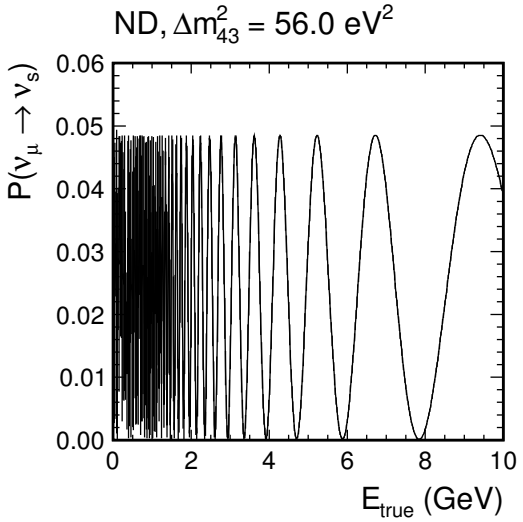

FIG. 8.2: Near detector $\nu_\mu \rightarrow \nu_s$ oscillation probability curve at $\Delta m^2_{34} = 56\,\mathrm{eV}^2$, $\theta_{24} = 8^\circ$ and $\theta_{34} = 37^\circ$.

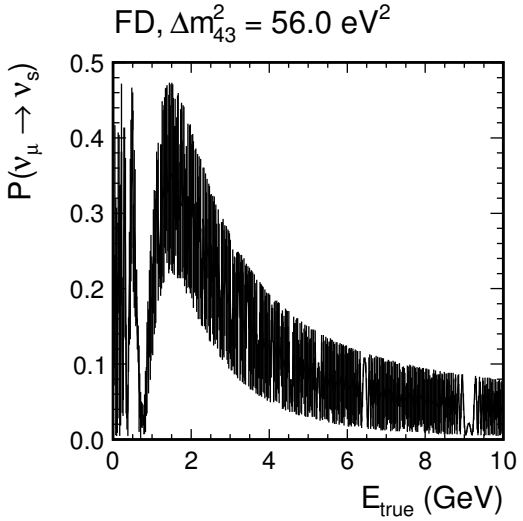

FIG. 8.3: Far detector $\nu_\mu \rightarrow \nu_s$ oscillation probability curve at $\Delta m^2_{34} = 56\,\mathrm{eV}^2$, $\theta_{24} = 8^\circ$ and $\theta_{34} = 37^\circ$.

BIBLIOGRAPHY

[1] P. Adamson et al. Active to sterile neutrino mixing limits from neutral-current interactions in minos. *Phys. Rev. Lett.*, 107:011802, June 2011.

[2] J. Chadwick. Distribution in intensity in the magnetic spectrum of the -rays of radium. *Ver. Dtsch. Physik. Ges.*, 16:383–391, 1914.

[3] C. D. Ellis and W. A. Wooster. The average energy of disintegration of radium E. *Proc. of the Royal Society of London: A*, 117(776):109–123, 1927.

[4] Wolfgang Pauli. Letter to the physical society of tubingen, 1930.

[5] J. Chadwick. Possible existence of a neutron. *Nature*, 129:312, 1932.

[6] E. Fermi. An attempt of a theory of beta radiation. *Z. Phys.*, 88:161–177, 1934.

[7] H. Bethe and R. Peierls. The 'neutrino'. *Nature*, 133:532, 1934.

[8] B. Pontecorvo. The neutrino and the recoil of nuclei in the beta disintegrations. *Rep. Prog. Phys.*, 11:32, 1947.

[9] C. L. Cowan Jr., F. Reines, et al. Detection of the free neutrino: a confirmation. *Science*, 159:694, 1956.

[10] R. Davis and D. Harmer. Attempt to observe the ^{37}Cl $(\bar{\nu}, e^-)$ ^{37}Ar reaction induced by reactor antineutrinos. *Bull. Am. Phys. Soc.*, 4:217, 1959.

[11] G. Danby et al. Observation of high-energy neutrino reactions and the existence of two kinds of neutrinos. *Phys. Rev. Lett.*, 9(1):36–44, 1962.

[12] B. T. Cleveland, T. Daily, R. Davis, et al. Measurement of the solar electron neutrino flux with the Homestake chlorine detector. *The Astrophysical Journal*, 496(1):505, 1998.

[13] M. L. Perl et al. Evidence for Anomalous Lepton Production in e^+ - e^- Annihilation. *Phys. Rev. Lett.*, 35:1489, 1975.

[14] DONUT Collaboration: K. Kodoma et al. Observation of the Tau Neutrino Interactions. *Phys. Rev. Lett.*, B504:218, 2001.

[15] M. Grunevald et al. Precision electroweak measurements of the Z resonance. *Phys. Rept.*, 427(5-6):257–454, 2006.

[16] Y. Fukuda et al. Evidence for oscillation of atmospheric neutrinos. *Phys. Rev. Lett.*, 81(8):1562–1567, 1998.

[17] M. H. Ahn et al. Indications of Neutrino Oscillation in a 250km Long-Baseline Experiment. *Phys. Rev. Lett.*, 90(041801), 2003.

[18] D.G. Michael et al. Observation of muon neutrino disappearance with the MINOS detectors and the NuMI neutrino beam. *Phys. Rev. Lett.*, 97(191801), 2006.

[19] Q. R. Ahmad et al. Direct evidence for neutrino flavor transformation from neutral-current interactions in the Sudbury Neutrino Obsevatory. *Phys. Rev. Lett.*, 89(011301), 2002.

[20] K. Eguchi et al. First results from KamLAND: Evidence for reactor antineutrino disappearance. *Phys. Rev. Lett.*, 90(021802), 2003.

[21] D. M. Webber et al. An improved measurement of electron antineutrino disappearance at Daya Bay. *Nucl. Phys. Proc. Suppl.*, 233:96–101, 2012.

[22] D. Griffiths. *Introduction to Elementary Particles*. WILEY-VCH Verlag GmbH and Co. kGaA, Weinheim, 2008.

[23] B. Pontecorvo. Inverse beta processes and nonconservation of lepton charge. *Sov. Phys.*, JETP 7:172, 1958.

[24] Nakagawa M. Sakata S. Maki, Z. Remarks on the unified model of elementary particles. *Prog. Theor. Phys.*, 28(870), 1962.

[25] D. Perkins. *Introduction to High Energy Physics*. Cambridge University Press, 2000.

[26] B. Kayser. Neutrino Mass, Mixing, and Flavor Change. *arXiv:hep-ph/0211134v1*, 2002.

[27] C. Athanassopoulos et al. Evidence for $\bar{\nu_\mu} \rightarrow \bar{\nu_e}$ Oscillations from the LSND experiment at LMAPF. *Phys. Rev. Lett.*, 77(3082), 1996.

[28] C. Athanassopoulos et al. The Liquid Scintillator Neutrino Detector and LAMPF neutrino source. *Nucl. Instrum. Meth.*, A388:149–172, 1997.

[29] M. Maltoni and T. Schwetz. Sterile neutrino oscillations after first MiniBooNE result. *Phys. Rev. D.*, 76(093005), 2007.

[30] A. A. Aguilar-Arevalo et al. A search for electron neutrino appearance at the $\Delta m^2 \sim 1eV^2$ scale. *Phys. Rev. Lett.*, 98(231801), 2007.

[31] Lhuillier D. Fallot M. Letourneau A. Cormon S. Mueller, T. et al. Improved Predictions of Reactor Antineutrino Spectra. *Phys. Rev. D.*, 83:054615, 2011.

[32] Fechner M. Lasserre T. Mueller T. Lhuillier D. Mention, G. et al. The Reactor Antineutrino Anomaly. *Phys. Rev. D.*, 83:073006, 2011.

[33] P. Anselmann et al. First results from the Cr-51 neutrino source experiment with the GALLEX detector. *Phys. Rev. Lett.*, B342:440–450, 1995.

[34] W. Hampel et al. Final results from the Cr-51 neutrino source experiments in GALLEX. *Phys. Rev. Lett.*, B420:114–126, 1998.

[35] Gavrin V. Girin S. Gorbachec V. Ibragimova T. V. Abdurashitov, D. et al. The Russian-American gallium experiment (SAGE) Cr neutrino source measurement. *Phys. Rev. Lett.*, 77:4708–4711, 1996.

[36] D. Abdurashitov et al. Measurements of the response of the Russian-American gallium experiment to neutrinos from a Cr-51 source. *Phys. Rev.*, C59:2246–2263, 1999.

[37] J. Hylen et al. NuMI Facility Technical Design Report. *Fermilab-TM-2018*, 1997.

[38] P. Adamson et al. A Study of Muon Neutrino Disappearance Using the Fermilab Main Injector Neutrino Beam. *Phys. Rev.*, D77, 2008.

[39] J. Coelho. Time and intensity correlations. MINOS-doc-9309, 2012.

[40] L. Loiacono. *Measurement of the Muon Neutrino Inclusive Charged Current Cross Section on Iron using the MINOS Detector*. PhD thesis, University of Texas at Austin, 2010.

[41] D.G. Michael et al. The magnetized steel and scintillator calorimeters of the MINOS experiment. *Nuclear Instruments and Methods in Physics Research A*, 596:190–228, 2008.

[42] N. Tagg et al. Performance of Hamamatsu 64-anode photomultipliers for use with wavelength shifting optical fibres. *Nucl. Instrum. Meth.*, A539:668–678, 2005.

[43] T. Cundiff et al. The MINOS Near Detector Front End Electronics. *IEEE Trans. Nuc. Sci.*, 53(3), 2006.

[44] J. Oliver et al. Design and Performance of the Readout System of the MINOS Far Detector. *IEEE Trans. Nuc. Sci.*, 51(5):2193–2195, 2004.

[45] A. Belias et al. The MINOS Data Acquisition System. *IEEE Trans. Nuc. Sci.*, 51(3), 2004.

[46] MINOS Collaboration. Calibration position paper for pre-shutdown data. MINOS-doc-3941, 2008.

[47] J.J. Hartnell. *Measurements of the calorimetry energy scale in MINOS.* PhD thesis, University of Oxford, 2005.

[48] P. Adamson et al. The MINOS calibration Detector. *Nuclear Instruments and Methods in Physics Research A*, 556:119–133, 2006.

[49] R. Brun et al. Geant detector description and simulation tool. Technical report, 1994.

[50] P.L. Vahle. *Electromagnetic interactions in the MINOS detectors.* PhD thesis, University of Texas at Austin, 2004.

[51] C. Zeitnitz and T.A. Gabriel. The geant-calor interface and benchmark calculations of zeus test calorimeters. *Nuclear Instruments and Methods in Physics Research A*, 349:106–111, 1994.

[52] M. Kordosky. *Hadronic interactions in the MINOS detectors.* PhD thesis, University of Texas at Austin, 2004.

[53] Corwin L. Sharma R. DeJong J. Phan-Budd, S. and M. Mathis. Blessed Plots of the Calibration Group. MINOS-doc-9089.

[54] P. Ballester. Hough transform for robust regression and automated detection. *Astron. Astrophys.*, 286:1011, 1994.

[55] Mokhov N.V. Groom, D.E. and S.I. Striganov. Muon stopping power and range tables 10mev - 100tev. *Atom. Data. Nucl. Data Tabl.*, 78:183–356, 2001.

[56] R.E. Kalman. A new approach to linear filtering and prediction problems. *Transactions of the ASME - Journal of Basic Engineering*, Series D(82):35–45, 1960.

[57] M. Campanella, A. Ferrari, P.R. Sala, and S. Vanini. First calorimeter simulation with the FLUGG prototype. *ATL-SOFT-99-004*, 1999.

[58] M. Campanella, A. Ferrari, P.R. Sala, and S. Vanini. Reusing code from FLUKA and GEANT4 geometry. *ALT-SOFT-98-039*, 1998.

[59] S. Agostinelli et al. G4-a simulation toolkit. *Nuclear Instruments and Methods in Physics Research A*, 506(3):250–303, 2003.

[60] F. Ballarini, G. Battistoni, F. Cerutti, A. Empl, A. Fasso, et al. Nuclear models in FLUKA: Present capabilities, open problems, and future improvements. *AIP Conf. Proc.*, 769:1197–1202, 2005.

[61] H. Gallagher. The NEUGEN neutrino event generator. *Nucl. Phys. B*, 112(1-3):188–194, 2002.

[62] T. Yang et al. A hadronization model for few-GeV neutrino interactions. *Eur. Phys. J. C*, 63:1–10, 2009.

[63] T. Sjostrand, S. Mrenna, and P. Skands. PYTHIA 6.4 physics and manual. *Journal of High Energy Physics*, 05(026), 2006.

[64] Z. Koba, B. Nielsen, and P. Olesen. Scaling of multiplicity distributions in high energy hadron collisions. *Nucl. Phys. B*, 40:317–334, 1972.

[65] R. Merenyi et al. Determination of pion intranuclear rescattering rates in $\nu_\mu - Ne$ versus $\nu_\mu - D$ interactions for the atmospheric ν flux. *Phys. Rev. D.*, 45(3):743–751, 1992.

[66] K. A. Olive and others (Particle Data Group). *Chin. Phys. C*, 38(010001), 2014.

[67] R. Toner and A.P Schreckenberger. An Updated Search for Electron Neutrino and Antineutrino Appearance in MINOS. Neutrino 2012 and Fermilab User's Meeting 2012.

[68] C. Backhouse et al. Neutral Current Analysis of 7.1×10^{20} POT of MINOS Data - Executive Summary. MINOS-doc-7191, 2010.

[69] G. Tinti. The ND Preselection for the NC analysis. MINOS-doc-7127, 2010.

[70] R. P. Litchfield. *Neutrino induced events in the MINOS detectors.* PhD thesis, University of Oxford, 2008.

[71] J. de Jong. Position Paper for the Runs I-II-III FD NC Cleaning. MINOS-doc-7165, 2010.

[72] P. Adamson et al. Search for sterile neutrino mixing in the MINOS long baseline experiment. *Phys. Rev.*, D81, 2010.

[73] A. Radovic. *Measuring the Disappearance of Muon Neutrinos with the MINOS Detector.* PhD thesis, University College Longon, 2013.

[74] R. Ospanov. *A Measurement of Muon Neutrino Disappearance with the MINOS Detectors and NuMI Beam*. PhD thesis, University of Texas at Austin, 2008.

[75] J. Ratchford. *Identifying Muons for Neutrino Oscillation and Cross Section Experiments*. PhD thesis, University of Texas at Austin, 2007.

[76] Adamson P. Holin, A. NUMI beam brag plots. MINOS-doc-9258, May 2012.

[77] P. Rodrigues. Notes on the Normalization Systematic for the NC and CC Analyses. MINOS-doc-6636, 2010.

[78] Hsu L. Rodrigues, P. Charged current background in the neutral current sample. MINOS-doc-3878, 2007.

[79] The MINOS Calibration Group. 2009 Position Paper on Calibration of Runs. MINOS-doc-6717, 2010.

[80] Gallagher H. Dytman S. Kordosky, M. Shower Energy Scale Uncertainty For the Run I+II CC Analysis. MINOS-doc-4287, 2008.

[81] J. O'Connor. Near Detector Neutral Current Cleaning Systematic. MINOS-doc-9819, 2013.

[82] J. Coelho. ND Cleaning Systematic. MINOS-doc-9664, 2013.

[83] J. Ratchford. A Data Driven Estimate to the NC background. MINOS-doc-7115, 2010.

[84] J. Evans. Absolute (calorimetric) shower energy uncertainty. MINOS-doc-7173, 2010.

[85] Favier J. Metref A. Pessard H. Achkar B. Declais, Y. et al. Search for neutrino oscillations at 15-meters, 40-meters, and 95-meters from a neuclear power reactor at bugey. *Nucl. Phys.*, B434:503–534, 1995.

[86] J. Huang. *Sterile Neutrino Searches in MINOS and MINOS+*. PhD thesis, University of Texas at Austin, 2015.

VITA

Alena V. Devan

Alena V. Devan [redacted]. In August 2005, she began her undergraduate education at George Mason University, majoring in physics. She graduated in 2008 and began her graduate career at the College of William and Mary. In 2009, she began working with Dr. Patricia Vahle within the experimental high energy group. She received a Master of Science in 2010. [redacted]. She is currently working for Dominion Enterprises in Norfolk, Virginia as a Data Engineer. Her thesis is devoted to the sterile neutrino search with the MINOS experiment at Fermilab.